

Atomistic molecular dynamics approach for channeling of charged particles in oriented crystals

Dissertation

zur Erlangung des Doktorgrades
der Naturwissenschaften

vorgelegt beim Fachbereich Physik
der Johann Wolfgang Goethe-Universität
in Frankfurt am Main

von

Gennady B. Sushko
aus Moskau, Russland

Frankfurt am Main
2015

(D30)

vom Fachbereich Physik der
Johann Wolfgang Goethe–Universität, Frankfurt am Main, als
Dissertation angenommen.

Dekan: Prof. Dr. Rene Reifarth

Gutachter: Prof. Dr. Andrey V. Solov'yov, Prof. Dr. Stefan Schramm, Prof. Dr. Marcus Bleicher

Datum der Disputation: 05.10.2015

for Notes

Kurzfassung

Der Gitterführungseffekt ist der Prozess der Ausbreitung von geladenen Teilchen entlang der Ebenen oder Achsen von kristallinen Materialien. Seit den 1960er Jahren ist dieser Effekt weitgehend theoretisch und experimentell untersucht worden. Dieser Effekt wurde für die Manipulation von Hochenergiestrahlen, die Hochpräzisionsstruktur- und -fehleranalyse von kristallinen Medien und die Herstellung von hochenergetischer Strahlung angewendet. Zur Abstimmung der Parameter der Gitterführung und Gitterführungsstrahlung wurde dieser Prozess für den Fall von künstlich nanostrukturierten Materialien, wie gebogenen Kristallen, Nanoröhren und Fullerit, angenommen. In den letzten Jahren wurde das Konzept des kristallinen Undulators formuliert und getestet, das besondere Eigenschaften der Strahlung aufgrund der Gitterführung von Projektilen in regelmäßig gebogenen Kristallen vorhersagt.

In dieser Arbeit werden die Prozesse der Gitterführung von Sub- und Multi-GeV-Elektronen und -Positronen durch den atomistischen Molekulardynamik-Ansatz untersucht. Die Ergebnisse dieser Studien wurden in einer Reihe von Artikeln während meiner Promotion in Frankfurt vorgestellt. Dieser Ansatz ermöglicht die Simulation komplexer Fälle von Gitterführung in geraden, gebogenen und periodisch gebogenen Kristallen aus reinen kristallinen Materialien und von gemischten Materialien wie Si-Ge-Kristallen, in mehrschichtigen und nanostrukturierten kristallinen Systemen. Die Arbeit beschreibt die Methode der Simulationen, stellt Ergebnisse von Simulationen für verschiedene Fälle vor und vergleicht die Ergebnisse von Simulationen mit aktuellen experimentellen Daten. Die Ergebnisse werden mit Schätzungen der dechanneling-Länge verglichen, dem Anteil der gittergeführten Projektile, der Winkelverteilung der ausgehenden Projektile und des Strahlungsspektrums.

Zusammenfassung

Der Gitterführungseffekt ist der Prozess der Ausbreitung von geladenen Teilchen entlang der Ebenen oder die Achsen von kristallinen Materialien [1]. Seit den 1960er Jahren ist dieser Effekt weitgehend theoretisch [1, 2] und experimentell [3, 4] untersucht worden. Dieser Effekt wurde für verschiedene Energien von Projektilen vom MeV- bis TeV-Bereich für verschiedene Arten von leichten Projektilen wie Elektronen [5] und Positronen, und für schwere Projektile wie Pionen [4], Protonen [6], Atome [7] und Ionen [3] untersucht. Dieser Effekt wurde sowohl für planare [8] und axiale [5, 9] Fälle für verschiedene Materialien, wie Silizium, Germanium, Wolfram [7], Kohlenstoff, Gold [10] und anderen untersucht.

Die Gitterführung wurde für die Manipulation von Hochenergiestrahlen [11], die Hochpräzisionsstruktur- und -fehleranalyse von kristallinen Medien [12, 13] und die Herstellung von hochenergetischer Strahlung [9] angewendet.

Aufgrund der Wechselwirkung mit den Atomkernen des Mediums wird der Gitterführungspartikel beschleunigt und erzeugt Strahlung. Dieser Vorgang wird Bremsstrahlung genannt [14]. Der Prozess der Gitterführungsstrahlung wurde in Arbeiten von E. Uggerhøj [9] und U. Uggerhøj [15], J. Watson [10], M. Kumakhov [14] und andere untersucht. Diese Strahlung ist durch eine sehr hohe Energie der Photonen und hohe monochromatisch gekennzeichnet.

Zur Abstimmung der Parameter der Gitterführung und Gitterführungsstrahlung wurde dieser Prozess für den Fall von künstlich nanostrukturierten Materialien, wie gebogenen Kristallen, Nanoröhren [16, 17] und Fullerit [18], angenommen.

In den letzten Jahren wurde das Konzept der kristallinen Undulators formuliert [19, 20, 21], das besondere Eigenschaften der Strahlung aufgrund der Gitterführung von Projektilen in regelmäßig gebogenen Kristallen vorhersagt. Die Wechselwirkung von hochenergetischen Elektron- und Positronstrahlen mit solchen kristallinen Strukturen ist der Gegenstand von aktuellen experimentellen [22, 23, 24, 25, 26, 27] und theoretischen [28, 29, 30, 31] Studien. Eine gute Übersicht dieser Arbeiten wird im

Buch [32] von Korol, Solov'yov und Greiner gegeben. Es ist möglich zwei Arten von kristallinen Undulatoren zu unterscheiden: Undulatoren mit großer Amplitude und langer Periode [19, 20, 32], in denen die Periode der Biegung größer ist als die Periode der Gitterführungsschwingungen und kurzperiodischen Undulatoren mit kleiner Amplitude [33, 34, 27, 35, 15] im entgegengesetzten Fall. Im Fall von kurzperiodischen Undulatoren wird die Photonenenergie der Undulatorstrahlung vorhergesagt, höher zu sein als die Energie der Strahlung durch die Gitterführung.

Die Simulation von Gitterführung kann mit verschiedenen Ansätzen durchgeführt werden: analytischer Ansatz im der quantenmechanischen Formalismus [36], Kontinuum-Potential-Näherung [37, 38], Monte-Carlo-Ansatz [39, 40] und direkte Modellierung der Wechselwirkung von Atomen mit Partikeln [41, 42, 43]. Die Verwendung der geeigneten Methode hängt von der Energie und dem Typ der Projektile, der Länge des Kristalls und der Menge der Strahlungsenergie ab. Der quantenmechanische Formalismus ist für Energien unterhalb von 100 MeV nötig. Bei höheren Energien stehen die klassischen relativistischen Bewegungsgleichungen zur Verfügung.

In dieser Arbeit werden die Prozesse der Gitterführung von Sub- und Multi-GeV-Elektronen und -Positronen durch den atomistischen Molekulardynamik-Ansatz untersucht. Die Ergebnisse dieser Studien wurden in einer Reihe von Artikeln während meiner Promotion in Frankfurt vorgestellt [44, 45, 46, 47, 48].

Innerhalb des atomistischen Molekulardynamik-Ansatzes, wird die Wechselwirkung eines Projektils mit einem Medium durch ein klassisches Wechselwirkungspotential in der Form von Molière [49] oder Pacios [50] Wechselwirkungspotential simuliert. Für den ausgewählten Energiebereich können die Quanteneffekte der des Gitterführungsprozesses vernachlässigt werden, und das System der klassischen relativistischen Bewegungsgleichungen verwendet werden.

Dieser Ansatz ermöglicht die Simulation komplexer Fälle von Gitterführung in geraden, gebogenen und periodisch gebogenen Kristallen aus reinen kristallinen Materialien und von gemischten Materialien wie Si-Ge-Kristallen. Dieser Ansatz ermöglicht es Naturbeschreibung dechanneling- (das Ende des Regimes des Gitterführung) und rechanneling-Effekte (Neustart des Regimes des Gitterführung) Effekte, die Bewegung in jeder Gitterrichtung und in amorphen Medien innerhalb eines Modells zu beschreiben. Es ermöglicht das Studium der Gitterführung in mehrschichtigen und nanostrukturierten kristallinen Systemen.

Die Arbeit beschreibt die Methode der Simulationen, stellt Ergebnisse von Simulationen für verschiedene Fälle und vergleicht die Ergebnisse von Simulationen

mit aktuellen experimentellen Daten. Die Ergebnisse werden mit Schätzungen dechanneling-Länge verglichen, dem Anteil der gittergeführten Projektile, der Winkelverteilung der ausgehenden Projektile und des Strahlungsspektrums. Der Vergleich der Simulationsergebnisse zeigt eine gute Übereinstimmung mit den experimentellen Daten.

Die Strahlungsspektrumverteilung wird im Rahmen der quasi-klassischen Methode, die die Quantenkorrekturen aufgrund des Strahlungsrückstoß-Effekts berücksichtigt, untersucht. Es konnte gezeigt werden [34], dass die Korrekturen zu starken Veränderungen der Strahlungsspektren von Multi-GeV-Projektilen führen.

Der atomistische Ansatz zur Simulation der Gitterführung, der in dieser Arbeit beschrieben wird, wurde umgesetzt in der Form eines Moduls [44] des MBN Explorer-Software-Pakets [51, 52]. MesoBioNano Explorer (MBN Explorer) ist ein Softwarepaket für die Multiskalensimulation komplexer molekularer Strukturen und deren Dynamik. Es hat viele einzigartige Features, eine breite Palette von Anwendungen in Physik, Chemie, Biologie, Materialwissenschaften und in verwandten Branchen. Es ist geeignet für klassische Molekulardynamik (MD), Monte Carlo (MC) und relativistische Simulationen einer großen Palette von molekularen Systemen unterschiedlicher Art, wie Nano- und biologische Systeme, nanostrukturierte Materialien, Komposit- / Hybridmaterialien, Gase, Flüssigkeiten, Feststoffe und Grenzflächen, atomarer Größe bis zu mesoskopischen Abmessungen.

Eine der Anwendungen von Elektronen- und Positronen-Gitterführung ist die Schaffung einer Lichtquellen. Eine Reihe von Arbeiten [29, 22, 32, 53, 33] beschreiben den kristallinen Undulator (CU) als ein Werkzeug zur Erzeugung von Strahlung mit sehr hoher Photonenenergie [56]. Eine Menge Arbeit in diesem Bereich wird auch experimentell durchgeführt [28, 54, 27]. Die weitere anspruchsvolle Aufgabe in diesem Forschungsbereich wird die Schaffung eines kristallinen Undulator-Laser (CUL) [55] sein. Der CUL sollte der Glanz der Strahlung zu verbessern. Der Glanz wird als die Anzahl der Photonen pro Zeiteinheit und Einheitsfläche und Einheitsraumwinkel und Bandbreite definiert und wird in der Regel in den Einheiten [photons/s/mm²/mrad/0.1%BW] angegeben [56].

Die Struktur dieser Arbeit ist folgende:

Im Kapitel 2 wird eine allgemeine Beschreibung der Theorie der Gitterführung gegeben. Es enthält auch die Beschreibung der Verfahren zur Berechnung des Strahlungsemissionsspektrums, die Beschreibung der analytischen Methode zur Berechnung der Strahlungsspektrums in amorphen Medien, den Überblick über die Her-

stellungsverfahren gebogener Kristalle und einen Überblick über die Computersimulationssoftware für das Studium des Gitterführungsprozesses.

Das Kapitel 3 beinhaltet die Beschreibung des vorgeschlagenen Simulationsalgorithmus, der in einem Artikel veröffentlicht [44] ist. Innerhalb dieses Verfahrens wird die Ausbreitung des Geschosses in dem Medium durch Lösung der relativistischen Bewegungsgleichungen des Geschosses modelliert, die die Interaktion mit Feststoffatomen des Mediums berücksichtigen. Dieses Kapitel enthält die Beschreibung der numerischen Verfahren zur Integration der Bewegungsgleichungen und die Methodik zur dynamischen Generierung der Umgebung des Geschosses Basis von eines Satzes vordefinierter Regeln. Das Kapitel enthält die Beschreibung der Molire- und Pacios-Wechselwirkungspotentiale für die Interaktion des Geschosses mit Atomen des Mediums, die Beschreibung des Stillinger-Weber-Vielteilchenpotentials [57] für die klassischen Moleküldynamiksimulationen der Struktur von Si-, Ge- und $\text{Si}_x\text{Ge}_{1-x}$ -Kristallen. Das Kapitel enthält auch die numerischen Eigenschaften des Gitterführungsprozesses dieser Arbeit und den Mechanismus der Mittelwertbildung und der Schätzung von statistischen Fehlern.

Das Kapitel 4 enthält die Ergebnisse der Simulation der Ausbreitung Sub-GeV und Multi-GeV-Projektilen in amorphem Medium und bei planarer und axialer Gitterführung. Für den Fall des amorphen Mediums werden die Ergebnisse der Berechnung des Strahlungsspektrums mit der analytischen Bethe-Heitler-Näherung [58, 59, 60] verglichen. Die Ergebnisse für planare Gitterführung wurden in Publikationen veröffentlicht [46, 44] und mit experimentellen Ergebnissen [8] sowohl in Bezug auf Länge und dechanneling Strahlungsspektrum verglichen.

Das Kapitel 5 enthält Ergebnisse der Simulation der Gitterführung von Elektronen und Positronen in gebogenen und periodisch gebogenen Kristallen. Für den Fall der gleichförmig gebogen Kristalle wurden die Ergebnisse der Simulationen als Artikel [47] veröffentlicht, und werden mit den letzten experimentellen Arbeiten [61, 27] über die Ablenkung der Strahlen von 3.35 GeV- und 6.3 GeV-Elektronen bei der Verwendung eines gleichmäßig gebogen Si-Kristalls verglichen. Dieser Versuch wurde als Fallstudie zur Abstimmung der Parameter des Modells und Auswahl geeigneter Wechselwirkungspotentiale gemacht. Für diesen Fall wird der Einfluß der Modellparameter auf die Ergebnisse der Simulation untersucht sowohl für den Fall des periodisch gebogenen Kristalls sowohl großer Amplitude mit langer Periode (LALP) als auch für Undulatoren kleiner Amplitude mit kurzer Periode (SASP). Für den LALP-Undulator wurden die Ergebnisse als Artikel [46] veröffentlicht. Für den SASP-

Undulator wurden die Simulationen für die Parameter des Lichtstrahls und Kristalls ähnlich zu laufenden Experimenten an der SLAC Versuchsanlage durchgeführt.

Das Kapitel 6 beschreibt die Verwendung des atomistischen Molekulardynamikansatzes zur Simulation von Gitterführung bei $\text{Si}_x\text{Ge}_{1-x}$ -Übergittern. Im ersten Abschnitt dieses Kapitels wird Simulation der Struktur der $\text{Si}_x\text{Ge}_{1-x}$ -Kristalle mit dem klassischen Molekulardynamik Ansatz und Stillinger-Weber-Vielteilchenpotential [57] durchgeführt. Diese Simulationen erlauben es die Abhängigkeit der Parameter der Struktur $\text{Si}_x\text{Ge}_{1-x}$ -Gitters von der Konzentration der Ge-Atome zu studieren. Die Ergebnisse dieser Simulationen sind in folgenden Abschnitten verwendet worden, um den Prozess der Gitterführung von Elektronen und Positronen in geraden $\text{Si}_x\text{Ge}_{1-x}$ -Übergittern zu simulieren. Es wird gezeigt, dass innerhalb des angewendeten Ansatzes die numerischen Parameter der Gitterführung in zusammengesetzten Kristallen sich allmählich mit Zunahme der Konzentration. Diese Abhängigkeit wurde für dechanneling-Länge, Akzeptanz und Strahlungsspektrum untersucht.

Das Kapitel 7 enthält die Zusammenfassung der Arbeit, zieht Schlussfolgerungen aus den Ergebnissen dieser Arbeit und gibt einen Ausblick auf Richtungen der Weiterentwicklung der angewendeten Methoden.

Contents

| | |
|---|-----------|
| Kurzfassung | v |
| Zusammenfassung | vi |
| 1 Introduction | 3 |
| 2 Relativistic mechanics and channeling processes | 9 |
| 2.1 Relativistic equations of motion | 9 |
| 2.1.1 Classical relativistic equations of motion | 12 |
| 2.1.2 Radiation damping force | 12 |
| 2.2 Calculation of radiation spectrum | 15 |
| 2.3 Bethe-Heitler approximation | 19 |
| 2.4 Crystal structure and crystallographic directions | 23 |
| 2.5 Continuous potential model | 24 |
| 2.6 Channeling in bent crystals | 27 |
| 2.7 Bent crystals production methods | 28 |
| 2.8 Overview of existing simulation methods | 31 |
| 3 Theoretical and computational methods | 35 |
| 3.1 Runge-Kutta integrator for relativistic equations of motion | 35 |
| 3.2 Dynamic generation of crystal structure | 37 |
| 3.3 Interaction of the projectile with the medium | 39 |
| 3.3.1 Molière potential | 39 |
| 3.3.2 Pacios potential | 41 |
| 3.4 Stillinger-Weber potential for classical MD | 42 |
| 3.5 Analysis of channeling fractions and calculation of dechanneling length | 43 |
| 3.5.1 Calculation of statistical error for channeling fraction | 43 |

| | | |
|----------|--|------------|
| 4 | Computational studies of channeling processes within the atomistic approach | 45 |
| 4.1 | Amorphous medium case study | 45 |
| 4.2 | Planar channeling | 47 |
| 4.2.1 | Results for 855 MeV electrons and positrons | 47 |
| 4.2.2 | Results for 6.7 GeV electrons and positrons | 54 |
| 4.3 | Axial channeling | 60 |
| 5 | Channeling in bent and periodically bent crystals | 65 |
| 5.1 | Channeling in bent crystals | 66 |
| 5.1.1 | Comparison with experimental results | 69 |
| 5.1.2 | Radiation spectrum | 72 |
| 5.1.3 | Comparison of results for Molière and Pacios potential | 74 |
| 5.1.4 | Influence of incident angle and temperature on channeling | 77 |
| 5.2 | Channeling in periodically bent crystals | 80 |
| 5.2.1 | Results for sub-GeV electrons and positrons | 80 |
| 5.2.2 | Results for 10 GeV electrons and positrons | 83 |
| 5.3 | Comparison of axial and planar channeling | 84 |
| 5.4 | Rechanneling in periodically bent crystals | 87 |
| 5.5 | Small-amplitude short-period undulator case study | 89 |
| 5.5.1 | Crystalline undulator stack | 93 |
| 6 | Channeling in binary crystalline structures | 97 |
| 6.1 | Modeling a Si-Ge crystal structure | 98 |
| 6.2 | Channeling in Si-Ge composite crystals | 101 |
| 6.3 | Channeling radiation in composite crystals | 103 |
| 7 | Summary and conclusions | 107 |
| 8 | Acknowledgments | 109 |

Chapter 1

Introduction

The channeling is the process of propagation of charged particles along the planes or axis of the crystalline materials [1]. Starting from 1960-s this effect was studied extensively both theoretically [1, 2] and experimentally [3, 4]. This effect was studied for different energies of projectiles starting from MeV up to TeV range, for different types of light projectiles such as electrons [5] and positrons, and for heavy projectiles such as pions [4], protons [6], atoms [7] and ions [3]. This effect was studied for both planar [8] and axial [5, 9] cases for various materials such as silicon, germanium, tungsten [7], carbon, gold [10] and others.

The channeling effect was applied to manipulation of high energy beams [11], the high-precision structural and defect analysis of crystalline medium [12, 13] and to the production of high-energy radiation [9].

Due to the interaction with nuclei of the atoms of the medium the channeling particle experiences accelerated motion and produces radiation. This process is called braking radiation or bremsstrahlung [14]. The process of channeling radiation was studied in works by E. Uggerhøj [9] and U. Uggerhøj [15], J. Watson [10], M. Kumakhov [14] and others. This radiation is characterized by very high energy of photons and high level of monochromaticity.

In order to tune the parameters of channeling and channeling radiation this process was adopted for the case of artificial nanostructured materials such as bent crystals, nanotubes [16, 17] and fullerites [18].

In recent years the concept of crystalline undulator was formulated [19, 20, 21], which predicts special properties of radiation due to channeling of projectiles in periodically bent crystals. The interaction of high energy beams of electrons and

positrons with such crystalline structures is the subject of active experimental [22, 23, 24, 25, 26, 27] and theoretical [28, 29, 30, 31] study. A good review of these works is given in book [32] by Korol, Solov'yov and Greiner. Two types of crystalline undulators can be distinguished: large-amplitude long-period undulators [19, 20, 32], in which the period of bending is larger, then period of channeling oscillations, and the small-amplitude short-period undulators [33, 34, 27, 35, 15] in the opposite case. In the case of short-period undulators the photon energy of undulator radiation is predicted to be higher, then the energy of channeling radiation.

Channeling simulation can be done using a few different approaches: analytic approach using quantum mechanical formalism [36], continuous potential approximation [37, 38], Monte-Carlo approach [39, 40] and direct modeling of interaction of atoms with particle [41, 42, 43]. The use of appropriate method depends on the energy and type of the projectiles, the length of the crystal and amount of radiated energy. The quantum mechanical formalism is necessary for energies below 100 MeV. For higher energies the classical relativistic equations of motion are applicable.

In this work the processes of channeling of sub- and multi-GeV electrons and positrons are studied by means of atomistic molecular dynamics approach. The results of these studies have been published in a series of articles written during my PhD work in Frankfurt [44, 45, 46, 47, 48], another two papers were submitted and are in the process of publication [62, 63].

Within the atomistic molecular dynamics approach the interaction of a projectile with a medium is simulated as an interaction with a set of neighboring atoms with a classical force field in form of Molière [49] or Pacios [50] interaction potential. For the selected energy range the quantum effects of channeling process can be neglected, and the system of classical relativistic equations of motion can be used.

This approach allows simulation of complex cases of channeling in straight, bent and periodically bent crystals consisting of pure crystalline materials and of mixed materials like Si-Ge crystals. This approach allows natural description of dechanneling and rechanneling effects, the motion in any crystalline direction and in amorphous medium within one model. It allows study of channeling in multi-layer and nanostructured crystalline systems.

The work describes the method of simulations, provides results of simulations for different cases and comparison of results of simulations with recent experimental data. The results are compared in terms of dechanneling length estimates, fractions of channeling projectiles, the angular distribution of outgoing projectiles and the

radiation spectrum. The comparison of simulation results shows a good agreement with experimental data.

The radiation spectrum distributions are studied within the framework of the quasi-classical method which accounts for the quantum corrections due to the radiative recoil effect. It was demonstrated [34] that the corrections lead to strong modifications of the radiation spectra of multi-GeV projectiles.

The atomistic approach to simulation of channeling described in this work was implemented in the form of a module [44] of the MBN Explorer software package [51, 52]. MesoBioNano Explorer (MBN Explorer) is a software package for the advanced multiscale simulations of complex molecular structure and dynamics. It has many unique features, a wide range of applications in Physics, Chemistry, Biology, Material Science, and in related Industries. It is suitable for classical molecular dynamics (MD), Monte Carlo (MC) and relativistic dynamics simulations of a large range of molecular systems of different kind, such as nano- and biological systems, nanostructured materials, composite/hybrid materials, gases, liquids, solids and various interfaces, with sizes ranging from atomic to mesoscopic dimensions.

One of the applications of electrons and positrons channeling is a creation of light sources. A series of works [29, 22, 32, 53, 33] describe the crystalline undulator (CU) as a tool for creation of radiation with very high photon energy [65], the latest and the most complete overview of field is published in the recent book [53]. A lot of work in this field is also done experimentally [28, 54, 27]. The further challenging task in this research area will be the creation of a crystalline undulator laser (CUL) [55]. In Figure 1.1 an overview of existing and proposed light sources is given. In this figure the results of experimental work [64] are referred and compared to the theoretical predictions of CUL radiation parameters. In Figure 1.1 different light sources are compared in terms of characteristic photon energy and peak brilliance. The brilliance is defined as the number of photons per unit of time, per unit of surface, per unit of solid angle, per unit of bandwidth and is usually given in the units of [photons/s/mm²/mrad/0.1%BW] [56].

The structure of this thesis is following:

In Chapter 2 the general description of theory of channeling is given. It contains also the description of the methods of calculation of radiation emission spectrum, the description of the analytic method of calculation of radiation spectrum in amorphous medium the overview of the bent crystal production techniques and an overview of the computer simulation software for study of the channeling process.

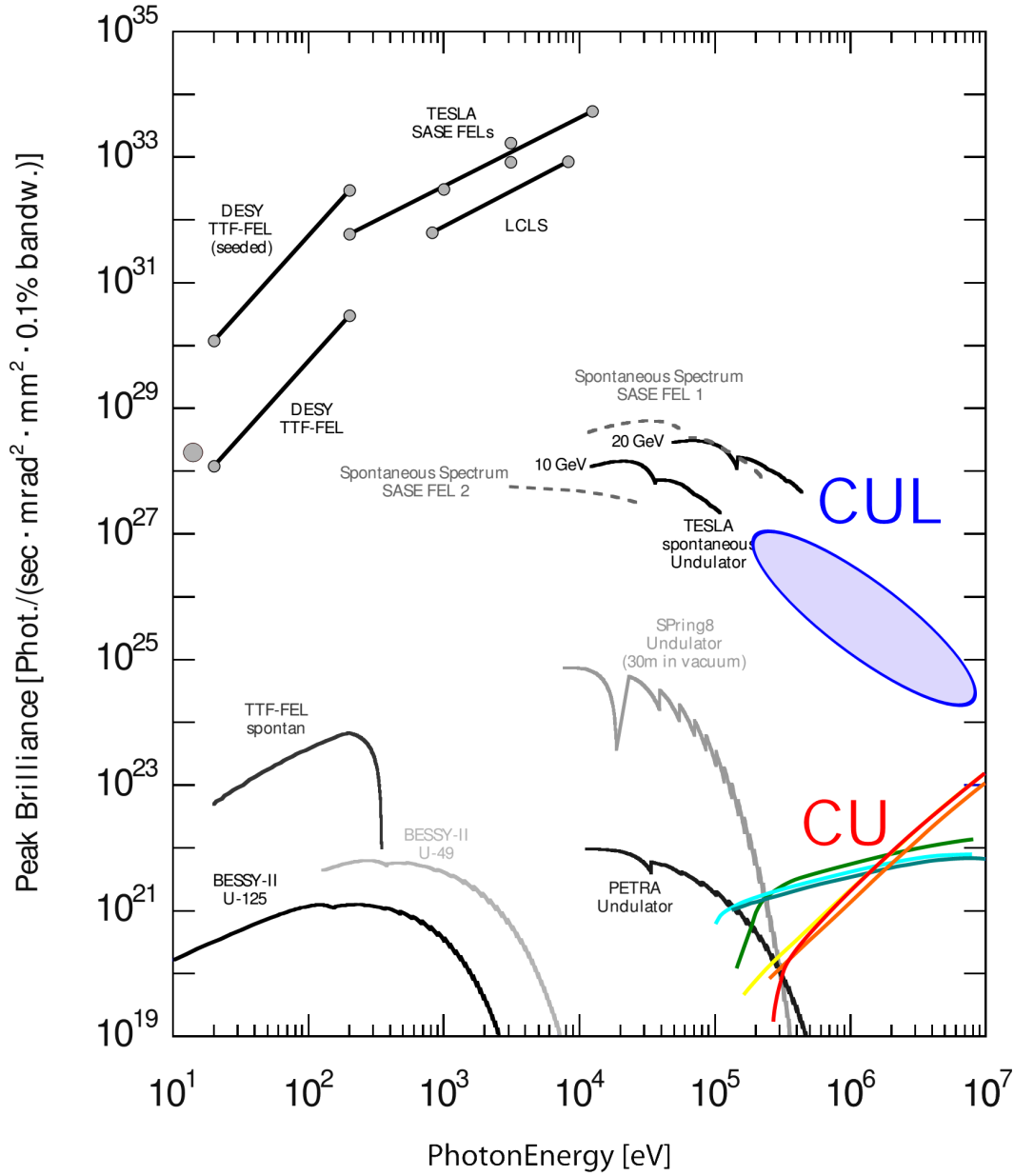


Figure 1.1: The comparison of existing light sources [64] with the proposed crystalline undulator [29] and crystalline undulator laser [55]. The CUR curves were calculated [65] for the KEKB positron beam and for SLAC beam [66]. The CUL area marks the estimation of the CUL parameters done with the parameters of the electron beam from the FLASH FEL [64]. The figure adapted from paper [32].

Chapter 3 contains the description of the proposed simulation algorithm and is based on published paper [44]. Within this method the propagation of the projectile in the medium is modeled by solution of the relativistic equations of motion of the

projectile, interacting with fixed atoms of the medium. This chapter contains the description of the numerical method for integration of equations of motion and the methodology of dynamic generation of the projectile environment based on set of predefined rules. The chapter contains the description of the Molière and Pacios interaction potentials of interaction of the projectile with atoms of the medium, it contains the description of the Stillinger-Weber [57] manybody potential for classical molecular dynamics simulations of structure of Si, Ge and $\text{Si}_x\text{Ge}_{1-x}$ crystals. The chapter also contains the numerical characteristics of channeling process used in this work and the mechanism of averaging and estimation of statistical errors.

Chapter 4 contains the results of the simulation propagation of sub-GeV and multi-GeV projectiles in case of amorphous medium, and planar and axial channeling. For the case of amorphous medium the results of calculation of radiation spectrum are compared with analytic Bethe-Heitler approximation [58, 59, 60]. The results for planar channeling case were published in papers [46, 44] and are compared with experimental results [8] in terms of both dechanneling length and radiation spectrum. The results for axial case were previously described in the paper [62] which is in the process of publication.

Chapter 5 contains results of the simulation of channeling of electrons and positrons in bent and periodically bent crystal. For the case of uniformly bent crystals the results of simulations were published in paper [47] and are compared with recent experimental works [61, 27] on deflection of beams of 3.35 GeV and 6.3 GeV electrons with the use of uniformly bent Si crystal. This experiment was taken as a case study for tuning the parameters of the model, and selection of appropriate interaction potential. For this case the influence of the model parameters on the results of simulation was studied. For the case of periodically bent crystal both large-amplitude long-period (LALP) and small-amplitude short-period (SASP) undulators are studied. For LALP undulator the results were published in paper [46]. For SASP undulator the simulations were performed for the parameters of beam and crystal similar to ongoing experiments at SLAC experimental facility. These results were previously described in the paper [63] which is in the process of publication.

Chapter 6 describes the use of the atomistic molecular dynamics approach for simulation of channeling in case of $\text{Si}_x\text{Ge}_{1-x}$ superlattices. In the first section of this chapter the simulation of the structure of $\text{Si}_x\text{Ge}_{1-x}$ crystals is performed using classical molecular dynamics approach and Stillinger-Weber [57] manybody potential. These simulations allowed to study the dependence of the parameters of structure

of $\text{Si}_x\text{Ge}_{1-x}$ superlattices on concentration of Ge atoms. The results of these simulations are used in next sections to simulate the process of channeling of electrons and positrons in straight $\text{Si}_x\text{Ge}_{1-x}$ superlattice. It is shown that within applied approach the numerical parameters of channeling in composite crystals change gradually with increase of concentration. Such dependence was studied for dechanneling length, acceptance and radiation spectrum.

Chapter 7 contains the summary of the thesis, concludes the results of this work and gives an outlook of directions of further development of applied methods.

Chapter 2

Relativistic mechanics and channeling processes

In this chapter the description of theoretical methods of this work is given. The description of the process of propagation of relativistic projectiles requires appropriate selection of equations of motion depending on energy of the projectile. This question is addressed in the Section 2.1. The second major question is the radiation emission due to the motion of projectiles, its calculation and characterization for different cases. These problems are the subject of Sections 2.2-2.3. The description of crystalline structures in the context of the problems of channeling is given in the Sections 2.4 and 2.5. In the Sections 2.6 and 2.7 an overview of problems of channeling in bent crystals and production of bent crystals is given. The Section 2.8 contains an overview of existing simulation methods and codes for modeling of channeling and related processes.

2.1 Relativistic equations of motion

The study of the motion of relativistic projectile in crystal requires proper selection of the formalism. The most detailed and precise description of the channeling, channeling radiation and related processes is based on the quantum mechanical approach.

Within this methodology the channeling process of fermions should be described by the Dirac equation, which for the particle interacting with the field of the crystal U can be written in the following form [67]:

$$(\varepsilon - U - m\beta c + i\hbar c\alpha\nabla)\phi(r) = 0 \quad (2.1)$$

where ε is the energy of the projectile, m is the rest mass of the projectile, c is the speed of light, \hbar is the reduced Planck constant, α is the Dirac matrix and $\phi(r)$ is the bispinor.

This equation can be transformed to the second order equation by applying operator $(\varepsilon - U + m\beta c - i\hbar c\alpha\nabla)$:

$$\left(-\hbar^2\Delta_r - p^2 + \frac{2\varepsilon U}{c^2} - \frac{U^2}{c^2} - \frac{i\hbar}{c}\alpha\nabla U\right)\phi(r) = 0 \quad (2.2)$$

where $p^2 = (\varepsilon^2 - m^2c^4)/c^2$ is the square of the momentum of the projectile. Due to the screening of charges of nuclei the potential energy U is much smaller than the electron or positron rest energy mc^2 , therefore the term U^2/c^2 can be neglected. It was shown in the paper [68] that the effect of spin is negligible in the case of channeling at energies of several GeV therefore term $\frac{i\hbar}{c}\alpha\nabla U$ can be also neglected. Dividing this equation by $2m\gamma$ the equation can be written in the following form:

$$\left(-\frac{\hbar^2}{2m\gamma}\Delta_r + U\right)\phi(r) = \varepsilon'\phi(r) \quad (2.3)$$

where $\varepsilon' = \varepsilon/\gamma$. This equation corresponds to the Schrödinger equation for the particle with mass $m\gamma$. For energies above 100 MeV the factor γ exceeds 200 and the relativistic mass of the projectile becomes comparable with the mass of atoms. In this case the motion of the projectile can be described purely classically using relativistic equations of motion.

In order to determine the lower limit of energy for which the quantum effects are significant consider the channeling of positrons in Si(110) plane. Within continuous potential approximation (see section 2.5) this motion can be considered as a motion in one-dimensional periodic potential. For positrons staying in one channel this potential can be written in a simplified parabolic form $U(\rho) = 4U_0\rho^2/d^2$, where U_0 is the depth of the potential (for Si(110) this value can be estimated as 22.9 eV), ρ is the displacement from the midplane of the channel and d is the interplanar distance (for Si(110) 1.92 Å). The energy levels for this case can be written in the following form:

$$\varepsilon_{\perp n} = \Delta\varepsilon_{\perp n}(n + 0.5) = \hbar\sqrt{\frac{8U_0}{d^2m\gamma}}(n + 0.5), \quad n = 0, 1, 2, \dots \quad (2.4)$$

This approximation is applicable for the transverse motion with the energy below the depth of the potential well $\varepsilon_{\perp n} < U_0$. Therefore, the number of energy levels is limited $N_\varepsilon = U_0/\Delta\varepsilon_{\perp n}$. For electrons the shape of the potential energy surface can be described using Pöschl-Teller potential and the $\Delta\varepsilon_{\perp n}$ in this case can be written as $\hbar\sqrt{\frac{2U_0}{b^2m\gamma}}$ where $b = 4U_0/3\sqrt{3}U'_{max}$ is the parameter of the potential.

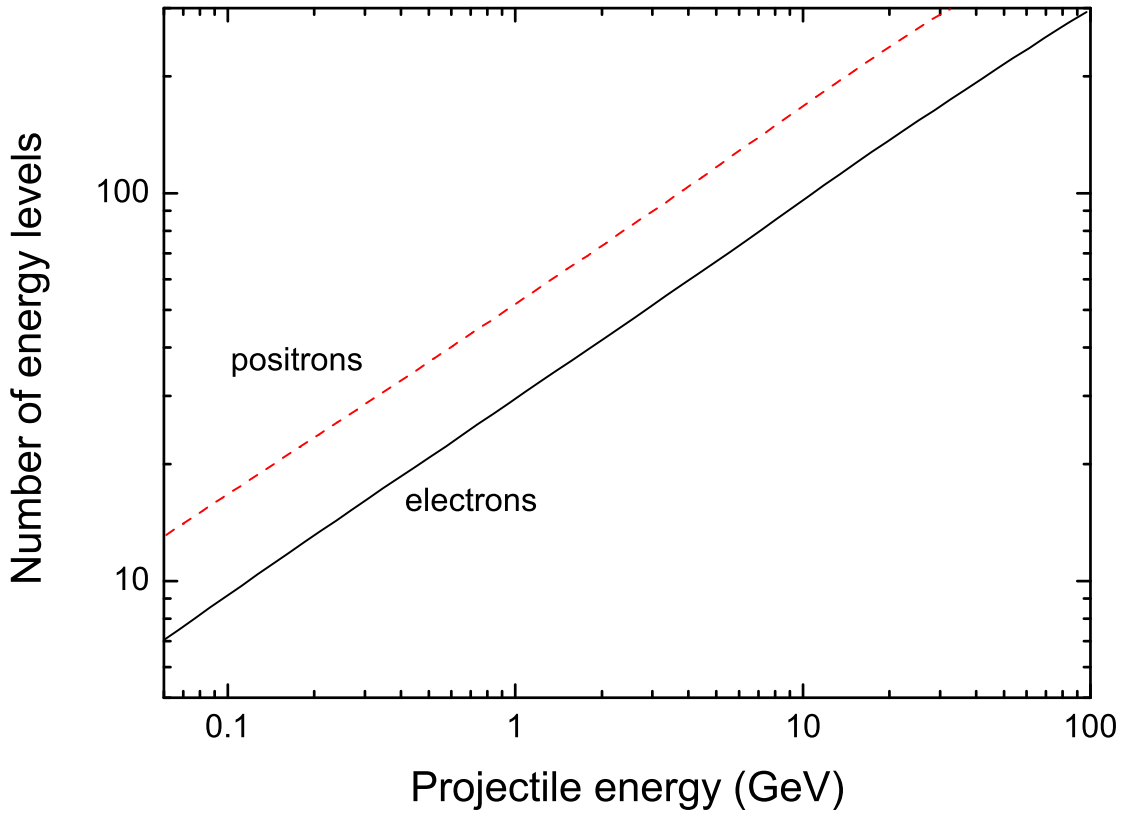


Figure 2.1: Dependence of number of energy levels of electrons and positrons in Si(110) on energy of the projectile in the continuous potential approximation [32]. The Pöschl-Teller potential was used for electrons, the parabolic potential was used for positrons.

In Figure 2.1 the dependence of number of energy levels of electrons and positrons in Si(110) on energy of the projectile is given. In the energy range $\varepsilon > 0.2$ GeV the number of energy levels $N_\varepsilon > 10 \gg 1$, which indicates that the classical description of the transverse motion of projectile can be applied.

Due to the difference in the profile of the interplanar potentials for electrons

and positrons, the range of applicability of the classical description of the transverse motion in the case of electrons is narrower than for the positron channeling [32, 69].

2.1.1 Classical relativistic equations of motion

Let us consider propagation of charged relativistic projectiles in the medium within the framework of classical relativistic mechanics [70] and describe the motion of the projectile in the laboratory reference frame. In this reference frame atoms of the medium are fixed, and the projectile is moving with the speed \mathbf{v} close to the speed of light c .

The motion of an ultra-relativistic projectile of the charge q and mass m in an external electrostatic field $\mathbf{E}(\mathbf{r})$ is subject to the relativistic equations of motion which can be written in the canonical form

$$\begin{cases} \dot{\mathbf{p}} = q\mathbf{E} \\ \dot{\mathbf{r}} = \mathbf{v} \end{cases} . \quad (2.5)$$

Dots over \mathbf{p} and \mathbf{r} in Eq. (2.5) denote differentiation with respect to time. The momentum \mathbf{p} written in terms of velocity reads $\mathbf{p} = m\gamma\mathbf{v}$ where γ stands for the Lorentz factor $\gamma = (1 - v^2/c^2)^{-1/2} = \varepsilon/mc^2$ with ε being the projectile energy.

The differential equations (2.5) are to be integrated for $t \geq 0$ using the initial values of the coordinates (x_0, y_0, z_0) and the velocity components (v_{x0}, v_{y0}, v_{z0}) of the particle.

2.1.2 Radiation damping force

The simulation of propagation of relativistic projectiles with very high energies requires accounting for the radiation damping effect [70]. In order to do this one should consider additional force acting on a projectile due to the radiation, which was created by the projectile itself:

$$\dot{\mathbf{p}} = q\mathbf{E} + \mathbf{f} \quad (2.6)$$

The form of this force was studied by Larmor [71], Heaviside [72], Abraham [73] and Dirac and was summarized in the paper by Rohrlich [74] in the following form:

$$\mathbf{f} = \frac{2}{3}q^2\gamma^2 (\ddot{\mathbf{v}} + 3\gamma^2\mathbf{v} \cdot \dot{\mathbf{v}}\dot{\mathbf{v}} + \gamma^2 (\mathbf{v} \cdot \ddot{\mathbf{v}} + 3\gamma^2(\mathbf{v} \cdot \dot{\mathbf{v}})) \mathbf{v}) \quad (2.7)$$

In this form the equation is called Lorentz-Abraham-Dirac (LAD) equation.

Another form of these equations is given in the classical book of Landau and Lifshitz [70]. In this case equations of motion should be extended with additional term:

$$\begin{cases} \dot{\mathbf{p}} = q\mathbf{E} + \mathbf{f} \\ \dot{\varepsilon} = q\mathbf{E}\mathbf{v} + \mathbf{f}\mathbf{v} \\ \dot{\mathbf{r}} = \mathbf{v} \end{cases} \quad (2.8)$$

where

$$\mathbf{f} = \frac{2q^3}{3mc^3} \left[\gamma(\mathbf{v}\nabla)\mathbf{E} + \frac{q}{mc^2}(\mathbf{v}\mathbf{E})\mathbf{E} - \frac{q}{mc^2}\gamma^2 \left(\mathbf{E}^2 - \frac{(\mathbf{v}\mathbf{E})^2}{c^2} \right) \mathbf{v} \right] \quad (2.9)$$

is the radiative damping force due to the presence of the electric field \mathbf{E} . The ∇ sign denotes the gradient operator. It can be seen, that this force is proportional to the square of the projectile energy, and is acting in the opposite direction to its velocity. Such force results to deceleration of a projectile.

In order to determine characteristic energy limits consider the case, where the force due to radiation damping is much higher than the force due to external field described in section 76 of book [70]. In this case following differential equation for energy can be written:

$$-d\varepsilon/dt = k(t)\varepsilon^2 \quad (2.10)$$

where $k(t)$ is the time-dependent coefficient. The solution of this differential equation gives:

$$\frac{1}{\varepsilon(\tau)} = \frac{1}{\varepsilon_0} + \int_{-\infty}^{\tau} k(t)dt \quad (2.11)$$

where ε_0 is the initial energy of the projectile. For the case of infinitely large initial energy $\varepsilon_0 \rightarrow \infty$, the value of the energy of the projectile saturates to a constant finite value, defined by the equation [75]:

$$\frac{1}{\varepsilon_{crit}} = \int_{-\infty}^{\infty} k(t) dt \quad (2.12)$$

or, substituting the expression for $k(x)$:

$$\frac{1}{\varepsilon_{crit}} = \frac{2}{3m^2c^4} \left(\frac{q^2}{mc^2} \right)^2 \int_{-\infty}^{\infty} (E_x^2 + E_y^2) dx \quad (2.13)$$

As a case study consider an electron channeling in Si(110) plane, in the 1 mm crystal. In this case $mc^2 = 0.5$ MeV, $qE_x \approx 6.37$ GeV/cm, $E_y = 0$, which give an estimation of critical energy of $\varepsilon_{crit} = 17.4$ TeV.

The total loss of energy due to radiation damping force can be written in the following form:

$$\delta\varepsilon = \frac{\varepsilon_0^2}{\varepsilon_0 + \varepsilon_{crit}} \quad (2.14)$$

Using this estimate, we find that for the considered direction and crystal thickness the energy loss becomes significant in the energy range above 100 GeV, and is negligible for the selected energy range of 1..10 GeV. The value of the ε_{crit} is inversely proportional to the length of the trajectory. For channeling projectiles the limiting factor in this case is the dechanneling length of the projectile. For positrons of the same energy the dechanneling length is more than one order of magnitude larger, which results in lower critical energy and higher effect of radiation damping for large crystals.

In the paper [76] it is shown, that already for 10 GeV electrons in very thick diamond crystals (1mm and above) in axial case the effect of radiation damping might lead to important correction of projectile energy and its proper description is required for correct simulations. It is also noted in papers [76, 77], that the introduction of radiation damping force in form of Eq. 2.7 may lead to non-physical solutions of differential equations and requires proper selection of integration scheme.

In this work the radiation damping force is omitted as the simulated projectiles are in the energy range below or equal to 10 GeV. The introduction of the damping force is the direction of further development of this work.

2.2 Calculation of radiation spectrum

Accelerated motion of charged projectiles in crystal channels produces radiation which can be characterized by radiation spectrum [69, 70, 78]. This spectrum describes distribution of energy between photons with different wave length.

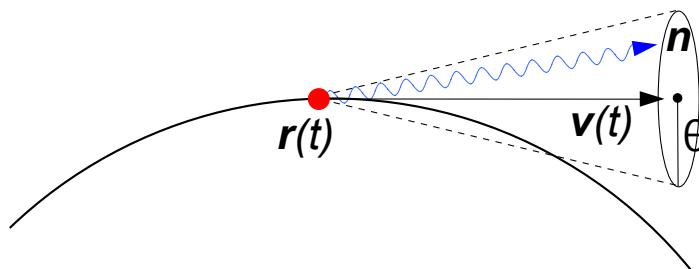


Figure 2.2: Due to the accelerated motion of a projectile the photons are emitted within the small cone around the direction of motion.

Using the relativistic equation of motion described in Section 2.1 one can calculate the trajectories of ultrarelativistic projectiles propagating through crystals. These trajectories can be used for the calculation of spectral distribution of emitted radiation. The detailed description of this process is given in the paper [44]. For N_0 simulated trajectories the spectral distribution of photons emitted within the cone $\theta < \theta_{max}$ with respect to the incident beam can be calculated as follows:

$$\frac{dE(\theta < \theta_{max})}{\hbar d\omega} = \frac{1}{N_0} \sum_{j=1}^{N_0} \int_0^{2\pi} d\phi \int_0^{\theta_{max}} \theta d\theta \frac{d^3 E_j}{\hbar d\omega d\Omega} \quad (2.15)$$

Here, $d^3 E_j / \hbar d\omega d\Omega$ stands for the spectral-angular distribution photons emitted by a particle which moves along the j th trajectory. The sum is carried out over all simulated trajectories in both channeling and non-channeling regimes.

To calculate $d^3 E_j / \hbar d\omega d\Omega$ one can use a general quasi-classical method developed by Baier and Katkov [79]. The quasi-classical approach explicitly takes into account the quantum corrections due to the radiative recoil. The method is applicable in the whole range of the emitted photon energies, except for the extreme high-energy tail of the spectrum ($1 - \hbar\omega/\varepsilon \ll 1$).

Within the framework of quasi-classical approach the spectral distribution of energy radiated in given direction \mathbf{n} by an ultra-relativistic particle is given by the following expression (see Ref. [78] for the details):

$$\frac{d^3 E_j}{\hbar d\omega d\Omega} = \frac{\alpha q^2 \omega^2}{4\pi^2} S \quad (2.16)$$

where

$$S = \int_{-\infty}^{\infty} dt_1 \int_{-\infty}^{\infty} dt_2 e^{i\omega'(\psi(t_1) - \psi(t_2))} \frac{1}{2} \left((1 + (1 + u)^2) \left(\frac{\mathbf{v}(t_1)\mathbf{v}(t_2)}{c^2} - 1 \right) + \frac{u^2}{\gamma^2} \right) \quad (2.17)$$

where $u = \frac{\hbar\omega}{\varepsilon - \hbar\omega}$, $\psi(t) = t - \frac{\mathbf{n} \cdot \mathbf{r}(t)}{c}$, $\omega' = \omega(1 + u)$. The values of ω' and u describe the effect of radiation recoil. In the classical limit $u \rightarrow 0$, $\omega' = \omega$.

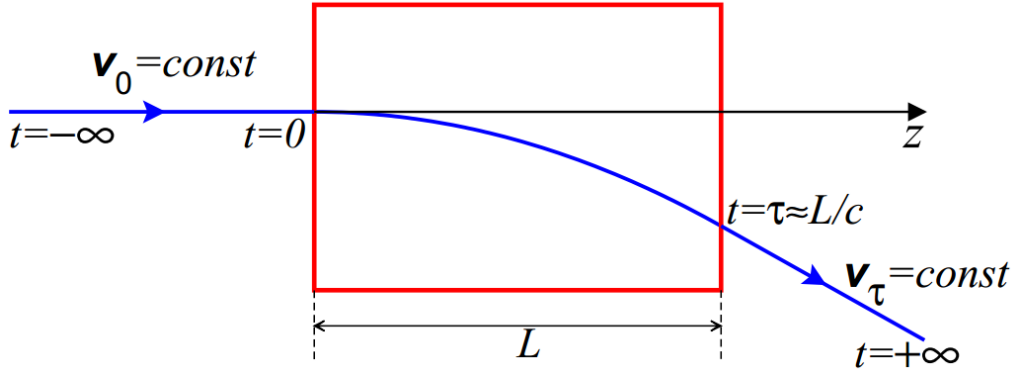


Figure 2.3: A trajectory of ultra-relativistic particle ($v \approx c$) which experiences the action of an external field within scattering medium of thickness L . Before entering the medium, i.e. within time interval $t < 0$, and after leaving it at $t = \tau \approx L/c$ the particle moves with constant velocities along the straight lines. Inside the medium the motion is affected by forces acting on the particle. Figure adapted from paper [44].

In Figure 2.3 a trajectory of the ultra-relativistic particle passing the crystal is illustrated. The radiation of a projectile should be calculated by taking into account motion of a projectile with constant velocity for both positive and negative infinity limits. The particle moves along a straight line $v(t) = v(0)$ for $t < 0$, and along another straight line $v(t) = v(\tau)$ for $t > \tau$, where τ corresponds to the time, when projectile leaves crystal.

In order to simplify equations the z-axis can be aligned with the initial velocity of the projectile. Due to the small values of emission angle $\theta \ll 1$ the components of vector \mathbf{n} can be written in the following form:

$$\mathbf{n} = \begin{bmatrix} \sin(\theta) \cos(\phi) \\ \sin(\theta) \sin(\phi) \\ \cos(\theta) \end{bmatrix} \approx \begin{bmatrix} \theta \cos(\phi) \\ \theta \sin(\phi) \\ 1 - \theta^2/2 \end{bmatrix}$$

Assuming $v_x \ll v_z \approx c$, $v_y \ll v_z \approx c$, and $v_x^2 + v_y^2 + v_z^2 = \text{const}$ one obtains the following relations:

$$\frac{v_z^2}{c^2} = 1 - \frac{1}{\gamma^2} - \frac{v_x^2}{c^2} - \frac{v_y^2}{c^2} \implies \frac{v_z}{c} = 1 - \frac{1}{2\gamma^2} - \frac{v_x^2}{2c^2} - \frac{v_y^2}{2c^2} \quad (2.18)$$

which gives the following transformation:

$$\begin{aligned} \frac{\mathbf{v}_1 \mathbf{v}_2}{c^2} - 1 &\approx -\frac{1}{\gamma^2} + \frac{v_x(t_1)v_x(t_2)}{c^2} + \frac{v_y(t_1)v_y(t_2)}{c^2} - \\ &\quad \frac{v_x^2(t_1) + v_x^2(t_2)}{2c^2} - \frac{v_y^2(t_1) + v_y^2(t_2)}{2c^2} \\ &= -\frac{1}{\gamma^2} - \frac{(v_x(t_1) - v_x(t_2))^2 + (v_y(t_1) - v_y(t_2))^2}{2c^2} \end{aligned} \quad (2.19)$$

Substituting this relation in equation (2.17) the following transformation can be written:

$$\begin{aligned} \int_{-\infty}^{\infty} dt_1 \int_{-\infty}^{\infty} dt_2 e^{i\omega'(\psi(t_1) - \psi(t_2))} \left(\frac{\mathbf{v}(t_1) \cdot \mathbf{v}(t_2)}{c^2} - 1 \right) &\approx \\ -\frac{1}{\gamma^2} |S_0|^2 + |S_{1x}|^2 + |S_{1y}|^2 - \text{Re} S_0 (S_{2x}^* + S_{2y}^*) \end{aligned} \quad (2.20)$$

where

$$S_0 = \int_{-\infty}^{\infty} dt e^{i\omega' \psi(t)}, \quad S_{1x,y} = \int_{-\infty}^{\infty} dt \frac{v_{x,y}}{c} e^{i\omega' \psi(t)}, \quad S_{2x,y} = \int_{-\infty}^{\infty} dt \frac{v_{x,y}^2}{c} e^{i\omega' \psi(t)} \quad (2.21)$$

and

$$S = \frac{1+u}{\gamma^2} (\gamma^2(1+\delta) (|S_{1x}|^2 + |S_{1y}|^2 - \text{Re} S_0 (S_{2x}^* + S_{2y}^*)) - |S_0|^2) \quad (2.22)$$

where

$$\delta = \frac{u^2}{2(1+u)} \quad (2.23)$$

Consider relation for $\psi(t)$:

$$\frac{d\psi(t)}{dt} = 1 - \frac{\mathbf{n} \cdot \mathbf{v}}{c} = 1 - \frac{n_z v_z}{c} - \frac{n_x v_x + n_y v_y}{c} \quad (2.24)$$

Using equation (2.18) and relation for \mathbf{n} :

$$\begin{aligned} \frac{d\psi(t)}{dt} &\approx 1 - \left(1 - \frac{\theta^2}{2}\right) \left(1 - \frac{1}{2\gamma^2} - \frac{v_x^2 + v_y^2}{2c^2}\right) - \theta \frac{\cos \phi v_x + \sin \phi v_y}{c} \approx \\ &\approx \frac{1}{2} \left(\frac{1}{\gamma^2} + \theta^2\right) + \frac{v_x^2(t)}{2c^2} + \frac{v_y^2(t)}{2c^2} - \theta \cos \phi \frac{v_x(t)}{c} - \theta \sin \phi \frac{v_y(t)}{c} \end{aligned}$$

Therefore

$$S_{2x} + S_{2y} = 2\theta (\cos \phi S_{1x} + \sin \phi S_{1y}) - \left(\frac{1}{\gamma^2} + \theta^2\right) S_0 \quad (2.25)$$

Using this relation the equation (2.22) can be rewritten in the following form:

$$\begin{aligned} S &= (1+u)(1+\delta) \left(\frac{\delta}{\gamma^2(1+\delta)} |S_0|^2 + \sin^2 \phi |S_{1x}|^2 + \cos^2 \phi |S_{1y}|^2 - \right. \\ &\quad \left. - 2 \cos \phi \sin \phi S_{1x} S_{1y} + |\theta S_0 - \cos \phi S_{1x} - \sin \phi S_{1y}|^2 \right) = \\ &= (1+u)(1+\delta) \cdot \left(\frac{\delta}{\gamma^2(1+\delta)} |S_0|^2 + |\sin \phi S_{1x} - \cos \phi S_{1y}|^2 + \right. \\ &\quad \left. + |\theta S_0 - \cos \phi S_{1x} - \sin \phi S_{1y}|^2 \right) \quad (2.26) \end{aligned}$$

Using this relation in the equation (2.16) one obtains following equation for spectra-angular distribution of emitted radiation:

$$\begin{aligned} \frac{d^3 E_j}{\hbar d\omega d\Omega} &= \frac{\alpha q^2 \omega^2}{4\pi^2} (1+u)(1+\delta) \cdot \left(\frac{\delta |S_0|^2}{\gamma^2(1+\delta)} + |\sin \phi S_{1x} - \cos \phi S_{1y}|^2 + \right. \\ &\quad \left. + |\theta S_0 - \cos \phi S_{1x} - \sin \phi S_{1y}|^2 \right) \quad (2.27) \end{aligned}$$

where α is the fine-structure constant, q is the charge of the projectile in a.u., θ

and ϕ are the spherical angles of the normalized direction \mathbf{n} of photon emission, γ is the relativistic Lorentz factor of the projectile, $\hbar\omega$ is the photon energy.

In order to take into account uniform motion of a projectile for $t < 0$ and $t > \tau$ one should use following equations for $\psi(t)$:

$$\psi(t) = \begin{cases} t \left(1 - \frac{\mathbf{n} \cdot \mathbf{v}(0)}{c}\right) - \frac{\mathbf{n} \cdot \mathbf{r}(0)}{c}, & t < 0 \\ t - \frac{\mathbf{n} \cdot \mathbf{r}(t)}{c}, & 0 \leq t \leq \tau \\ t \left(1 - \frac{\mathbf{n} \cdot \mathbf{v}(\tau)}{c}\right) - \frac{\mathbf{n} \cdot (\mathbf{r}(\tau) - \mathbf{v}(\tau)\tau)}{c}, & t > \tau \end{cases} \quad (2.28)$$

Substituting this relation to equation (2.21) the following modified equations for S_0 and $S_{1x,y}$ can be obtained:

$$\begin{aligned} S_0 &= \int_{-\infty}^0 dt e^{i\omega'\psi(t)} + \int_0^\tau dt e^{i\omega'\psi(t)} + \int_\tau^\infty dt e^{i\omega'\psi(t)} = \\ &= \int_0^\tau dt e^{i\omega' \left(t - \frac{\mathbf{n} \cdot \mathbf{r}(t)}{c}\right)} - \frac{i}{\omega'} \left(\frac{e^{i\omega'\psi(0)}}{D_0} - \frac{e^{i\omega'\psi(\tau)}}{D_\tau} \right) \end{aligned}$$

and

$$S_{1x,y} = \int_0^\tau dt \frac{v_{x,y}(t)}{c} e^{i\omega' \left(t - \frac{\mathbf{n} \cdot \mathbf{r}(t)}{c}\right)} - \frac{i}{\omega'} \left(\frac{v_{x,y}(0)}{c} \frac{e^{i\omega'\psi(0)}}{D_0} - \frac{v_{x,y}(\tau)}{c} \frac{e^{i\omega'\psi(\tau)}}{D_\tau} \right) \quad (2.29)$$

where

$$D(0) = 1 - \frac{\mathbf{n} \cdot \mathbf{v}(0)}{c}, \quad D(\tau) = 1 - \frac{\mathbf{n} \cdot \mathbf{v}(\tau)}{c} \quad (2.30)$$

2.3 Bethe-Heitler approximation

During the process of scattering of a charged projectile on a static field of a heavier target atom the accelerated motion of charge produces photon emission. This process is called bremsstrahlung. For ultra-relativistic projectiles, the analytic Bethe-Heitler (BH) approximation [58] (with various corrections due to Bethe *et al.* [59, 60] and Tsai *et al.* [80]) is the simplest and the most widely used description of this process. A good overview of this approximation was given in the appendix B of the paper [44].

In this section the relevant formulae for the case of ultra-relativistic electrons and positrons scattering from a neutral atom treated within the Molière approximation [49] are presented.

Following Eq. (3.80) in Ref. [80], one can write the following formula for the cross section differential with respect to the photon energy $\hbar\omega$ and to the emission angle $\Omega = (\theta, \phi)$ (but integrated over the angles of the scattered electron):

$$\frac{d^2\sigma}{d(\hbar\omega)d\Omega} = \frac{2\alpha^3 E^2}{\pi\hbar\omega m^4} \left(\left(\frac{2x-2}{(1+l)^2} + \frac{12l(1-x)}{(1+l)^4} \right) (Z^2 + Z) + \left(\frac{2-2x+x^2}{(1+l)^2} - \frac{4l(1-x)}{(1+l)^4} \right) (X - 2Z^2 f((\alpha Z)^2)) \right) \quad (2.31)$$

$$f((\alpha Z)^2) = (\alpha Z)^2 \sum_{n=1}^{\infty} [n^2 (n^2 + (\alpha Z)^2)]^{-1} \quad (2.32)$$

$$X = \int_{t_{min}}^{m^2(1+l)^2} (Z^2 + Z) \frac{t - t_{min}}{t^2} dt \quad (2.33)$$

$$t_{min} = \left(\frac{m^2(1+l)}{2\hbar\omega x(1-x)} \right)^2 \quad (2.34)$$

Here $\alpha \approx 1/137$ is the fine structure constant, Z is the atom number, $l = \theta_k^2 E^2 / m^2$, $x = \hbar\omega / \varepsilon$. The function f is the correction worked out by Bethe and Maximon [59, 60]. After simplification it can be written in the following form:

$$\frac{d^2\sigma}{d(\hbar\omega)d\Omega} = \frac{4\alpha r_0^2}{\pi} \frac{\gamma^2}{\hbar\omega} \left\{ \left(2 - 2x + x^2 - \frac{4(1-x)}{1+\xi} + \frac{4(1-x)}{(1+\xi)^2} \right) \frac{\mathcal{F} - 1 + \ln(1+\xi)}{(1+\xi)^2} - Z(Z+1) \left(1 - \frac{6}{1+\xi} + \frac{6}{(1+\xi)^2} \right) \frac{1-x}{(1+\xi)^2} \right\}. \quad (2.35)$$

Where $r_0 = e^2/mc^2 \approx 2.818 \times 10^{-13}$ cm is the classical electron radius and $\xi = (\gamma\theta)^2$. The factor \mathcal{F} is defined by Eqs. (3.5), (3.44) and (3.45) from Ref. [80]. In the ultra-relativistic limit (more exactly, for $\gamma \gtrsim 10^3$) it can be written as follows:

$$\mathcal{F} = Z^2 \left(\ln \frac{184}{Z^{1/3}} - 1 - f((\alpha Z)^2) \right) + Z \left(\ln \frac{1194}{Z^{2/3}} - 1 \right), \quad (2.36)$$

In the limit $(\alpha Z)^2 \ll 1$ the term $f((\alpha Z)^2)$ can be ignored. For example, for a Si atom ($Z = 14$) $f((\alpha Z)^2) \approx 0.0126 \ll 1$. For other widely used crystals materials this is also correct for C ($Z = 6$, $f \approx 0.002 \ll 1$), that is a less precise approximation for Ge ($Z = 32$, $f \approx 0.056 \ll 1$) and is not true for W ($Z = 74$, $f \approx 0.25$).

The term proportional to Z^2 on the right-hand sides of (2.35) and (2.36) stands for the contribution of the elastic bremsstrahlung process in which the target atom does not change its state during the collision. The terms $\propto Z$ are due to the inelastic bremsstrahlung channels, when the atom becomes excited or ionized.

To calculate the cross section of bremsstrahlung radiated into the cone with the opening angle θ_0 one integrates Eq. (2.35) over the emission angles $\theta = [0, \theta_0]$ and $\phi = [0, 2\pi]$. The result can be written as:

$$\left. \frac{d\sigma}{d(\hbar\omega)} \right|_{\theta \leq \theta_0} = \frac{d\sigma}{d(\hbar\omega)} + \frac{4\alpha r_0^2}{\hbar\omega} \left\{ Z(Z+1) \left(1 - \frac{4}{D_0} + \frac{26}{9D_0^2} \right) \frac{1-x}{D_0} - \left(2 - 2x + x^2 - \frac{2(1-x)}{D_0} + \frac{4(1-x)}{3D_0^2} \right) \frac{\mathcal{F} + \ln D_0}{D_0} \right\}, \quad (2.37)$$

with $D_0 = 1 + (\gamma\theta_0)^2$. In the limit of large emission angles when $\theta_0 \gg 1/\gamma$ the second term on the right-hand side goes to zero. Therefore, the first term stands for the cross section differential in the photon energy but integrated over the whole range of the emission angles. Its explicit expression is as follows (cf. Eq. (3.83) in Ref. [80]):

$$\frac{d\sigma}{d\hbar\omega} = \int_0^{2\pi} d\phi \int_0^\infty \frac{\theta d\theta d^2\sigma}{d\hbar\omega d\Omega} \approx \frac{4\alpha r_0^2}{3\hbar\omega} \left((4 - 4x + 3x^2) \mathcal{F} + Z(Z+1) \frac{1-x}{3} \right) \quad (2.38)$$

To calculate the cross section of the elastic bremsstrahlung one substitutes $Z(Z+1) \rightarrow Z^2$ on the right-hand sides of Eqs. (2.35), (2.37) and (2.38) as well as ignores the last term in Eq. (2.36). The latter approximation leads to the following reduction:

$$\mathcal{F} \rightarrow \mathcal{F}_{\text{el}} = Z^2 \left[\ln \frac{184}{Z^{1/3}} - 1 - f((\alpha Z)^2) \right]. \quad (2.39)$$

Then, the single differential cross section of elastic bremsstrahlung emitted within

the cone $0 \leq \theta \leq \theta_0$ is given by:

$$\left. \frac{d\sigma_{\text{el}}}{d(\hbar\omega)} \right|_{\theta \leq \theta_0} = \frac{d\sigma_{\text{el}}}{d(\hbar\omega)} + 4\alpha r_0^2 \frac{Z^2}{\hbar\omega} \left\{ \frac{1-x}{D_0} \left(1 - \frac{4}{D_0} + \frac{26}{9D_0^2} \right) - \left(2 - 2x + x^2 - \frac{2(1-x)}{D_0} + \frac{4(1-x)}{3D_0^2} \right) \frac{\mathcal{F}_{\text{el}} + \ln D_0}{Z^2 D_0} \right\} \quad (2.40)$$

where

$$\frac{d\sigma_{\text{el}}}{d(\hbar\omega)} = \frac{4\alpha r_0^2}{3} \frac{Z^2}{\hbar\omega} \left[(4 - 4x + 3x^2) \frac{\mathcal{F}_{\text{el}}}{Z^2} + \frac{1-x}{3} \right] \quad (2.41)$$

is the Bethe-Heitler spectrum of elastic bremsstrahlung.

Within the framework of less accurate approximation, used frequently for quantitative estimates (see, e.g., [81, 8]), one ignores the non-logarithmic terms in (2.39):

$$\mathcal{F}_{\text{el}} \approx \ln \frac{184}{Z^{1/3}}. \quad (2.42)$$

To calculate spectral-angular distribution of the radiated energy $d^2E/d(\hbar\omega)d\Omega$ in an amorphous target of the thickness L much less than the radiation length [82] one multiplies Eq. (2.35) by the photon energy $\hbar\omega$, by the volume density n of the target atoms and by L :

$$\frac{d^2E}{d(\hbar\omega)d\Omega} = nL \hbar\omega \frac{d^2\sigma}{d(\hbar\omega)d\Omega}. \quad (2.43)$$

Spectral distribution $dE/d(\hbar\omega) \Big|_{\theta \leq \theta_0}$ of the energy radiated within the cone $\theta \leq \theta_0$ is obtained from (2.43) by substituting the double differential cross section either with $d\sigma/d(\hbar\omega) \Big|_{\theta \leq \theta_0}$ (for the total emitted energy) or with $d\sigma_{\text{el}}/d(\hbar\omega) \Big|_{\theta \leq \theta_0}$ (if accounting for elastic bremsstrahlung only).

For illustrative purposes the spectral distributions $dE_{\text{el}}/d(\hbar\omega) \Big|_{\theta \leq \theta_0}$ of elastic bremsstrahlung formed during the passage of a $\varepsilon = 855$ MeV electron through a 50 μm thick amorphous silicon ($n = 5 \times 10^{22} \text{ cm}^{-3}$) is presented in Figure 2.4. The curves were calculated for different values of the emission cone angle as indicated. The value $\theta_0 = 0.21$ mrad corresponds to the limit of small emission angles $(\gamma\theta_0)^2 \ll 1$ where $\gamma^{-1} \approx 6 \times 10^{-3}$ for the indicated incident energy. For each photon energy the magnitude of $dE_{\text{el}}/d(\hbar\omega) \Big|_{\theta \leq \theta_0}$ steadily increases with θ_0 reaching its upper limit at $\theta_0 = \pi$ which corresponds to the cross section integrated over the whole

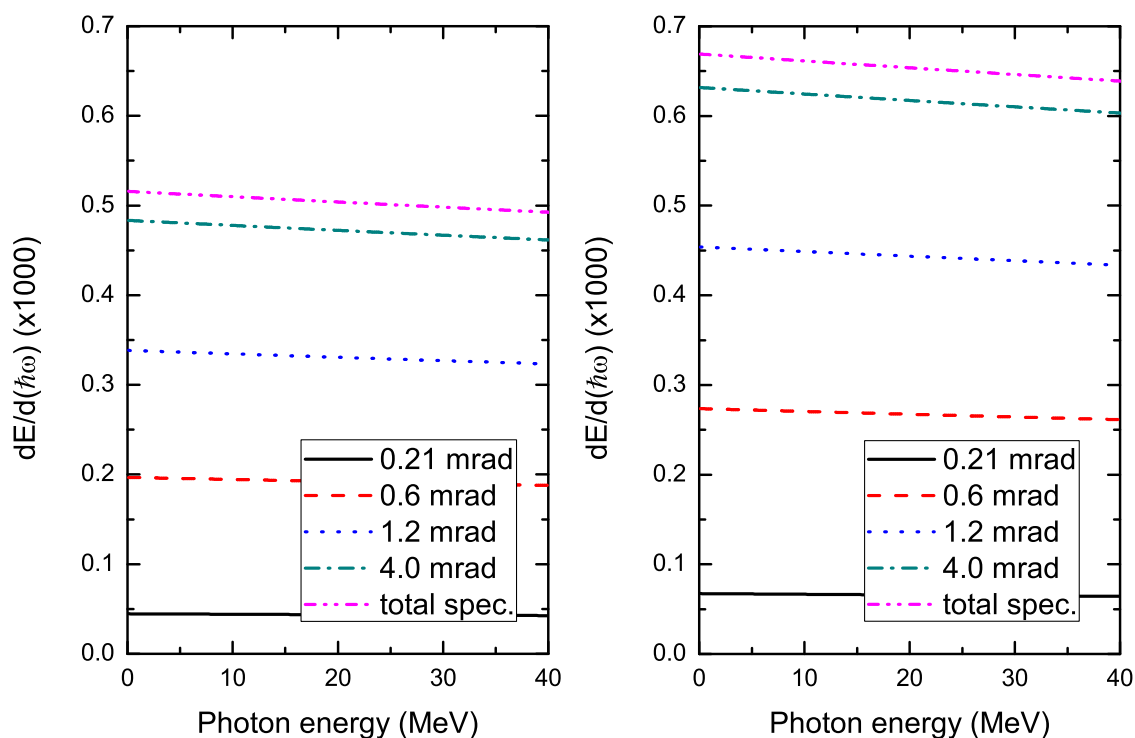


Figure 2.4: Bethe-Heitler spectra of the energy $dE_{\text{el}}/d(\hbar\omega)$ radiated via the elastic channel by a $\varepsilon = 855$ MeV electron in amorphous silicon of the thickness $50 \mu\text{m}$. Left panel corresponds \mathcal{F}_{el} given by Eq. (2.39), right panel corresponds to Eq. (2.42). Different curves correspond to different values of the emission cone angle θ_0 as indicated. The curve "total spec." stands for the spectral distribution integrated over the whole range of emission angles.

range of emission angle, see Eq. (2.41).

The comparison of the radiation spectrum for ultrarelativistic electrons and positrons given by Bethe-Heitler approximation with the results of numerical calculation is given in Section 4.1. It is shown that the results of direct calculation of radiation spectrum for projectile in simulated amorphous medium are in a good agreement with both forms of this approximation.

2.4 Crystal structure and crystallographic directions

In mineralogy and crystallography, a crystal structure is a unique arrangement of atoms, ions or molecules in a crystalline medium. It describes a highly ordered

structure, occurring due to the intrinsic nature of its constituents to form symmetric patterns. These patterns depend on a type of atoms and their interactions.

The structure of a crystal can be described by a unit cell and three translation vectors, which define the pattern formation. The unit cell is represented in terms of its lattice parameters, which are the lengths of the cell edges (a , b and c) and the angles between them (alpha, beta and gamma), while the positions of the atoms inside the unit cell are described by the set of atomic positions (x_i , y_i , z_i) measured in terms of fractional coordinates, relative to the unit cell lengths [83]. In Figure 2.5 unit cells for simple cubic, body-centered cubic (BCC) and Face-centered cubic (FCC) crystalline structures are illustrated. These crystalline structures are of a main interest of this work as corresponding materials are usually applied for channeling experiments.

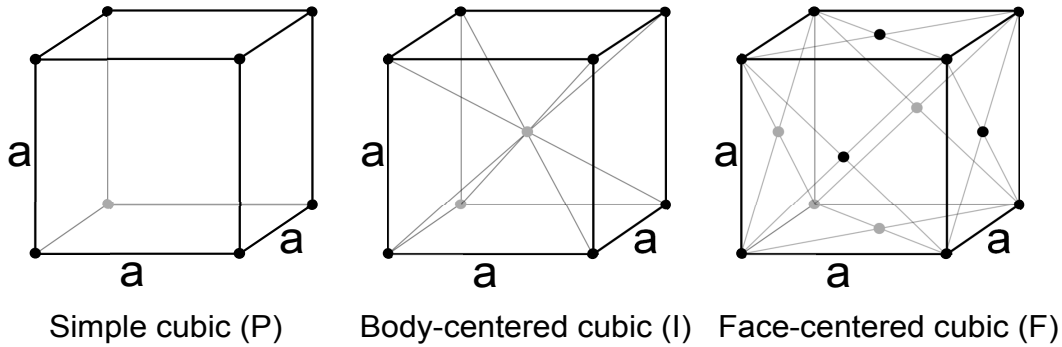


Figure 2.5: Unit cells for simple cubic, body-centered cubic (BCC) and Face-centered cubic (FCC) crystalline structures.

To characterize directions in a crystalline medium the Miller indices are used. These indices consist of three values l, m, n . The direction $\langle l, m, n \rangle$ corresponds to a vector $\mathbf{r} = l\mathbf{a} + m\mathbf{b} + n\mathbf{c}$, the set of planes (l, m, n) is defined as orthogonal to this direction. The notation \bar{l} corresponds to a negative value of l . In Figure 2.6 examples of planes with different indices are shown.

2.5 Continuous potential model

One of the widely used theoretical methods of description of channeling is the continuous potential method. Within this approach the interaction of a projectile with crystalline planes are described as an interaction with a periodic one-dimensional potential. The form of this potential is different for positive and negative projec-

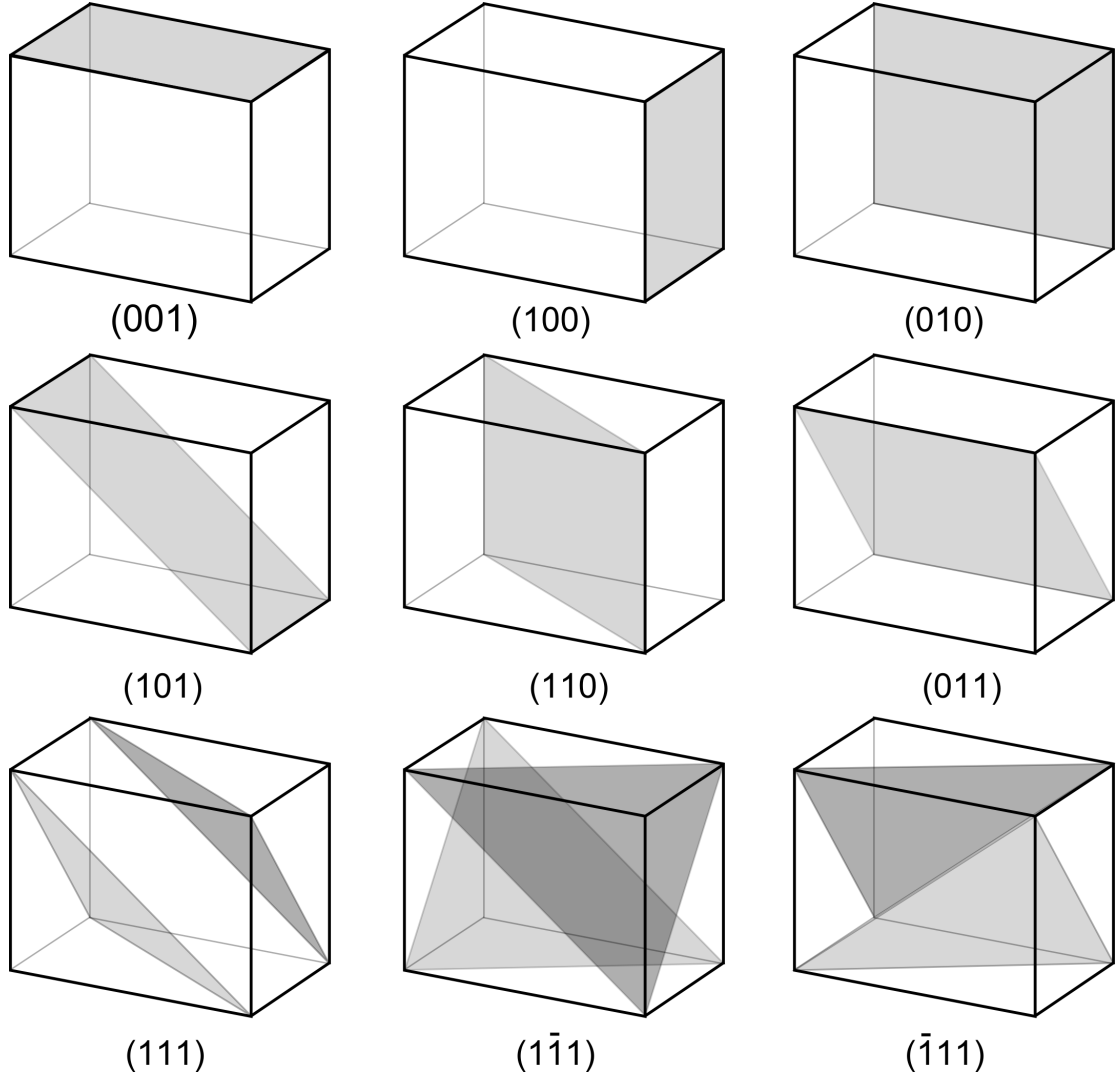


Figure 2.6: Planes with different Miller indices in cubic crystals

tiles. In Figure 2.7 the form of this potential within Molière approximation and its approximation are presented. For positive projectiles the parabolic form of the potential can be applied. For negative projectiles the Pöschl-Teller potential [84] can be used. This potential can be written in the following form:

$$U_{PT}(\rho) = a_{PT} \tanh^2(\rho/b_{PT}) \quad (2.44)$$

The parameters a_{PT} and b_{PT} are determined by the depth of the potential energy well (U_0) and the maximal gradient of the potential energy (U'_{max}). These parameters are either known from experiment or calculated using other methods. Following

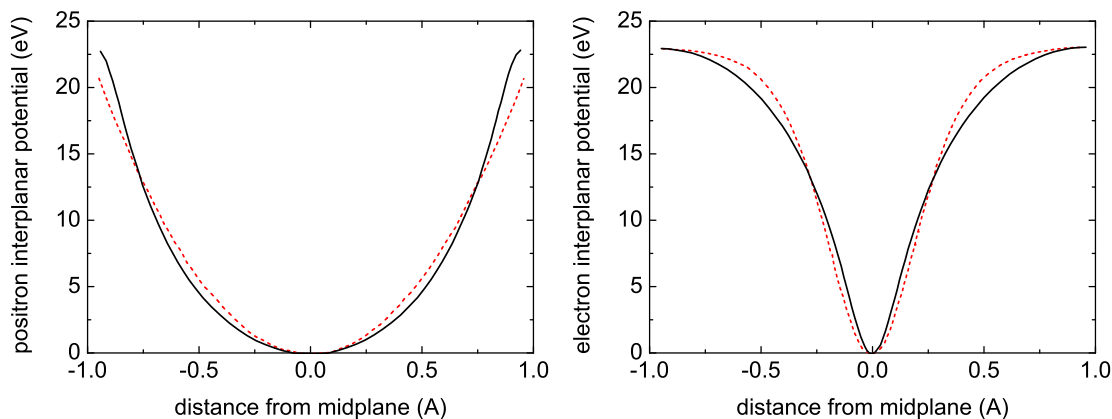


Figure 2.7: The interplanar potential in Si(110) for positrons (left) and electrons (right). In both panel solid line stands for the potential calculated within the Molière approximation at crystal temperature 150 K. The dashed red curve on the left panel represents the harmonic approximation, on the right panel - the Pöschl-Teller approximation. Adapted from book [32]

equations can be written for the parameters of the potential:

$$\begin{cases} a_{PT} = 3^{3/2} b_{PT} U'_{max} / 4 \\ \frac{d}{2b_{PT}} = k \tanh^2 \left(\frac{d}{2b_{PT}} \right) \\ k = 3^{3/2} d U'_{max} / 8 U_0 \end{cases} \quad (2.45)$$

Parameters of the Pöschl-Teller potential for carbon, silicon, germanium and tungsten in (110) and (111) planes are provided in Table 2.1.

| | Channel | d (Å) | U'_{max} (GeV/cm) | U_0 (eV) | a_{PT} (eV) | b_{PT}/d |
|----|---------|------------|------------------------|---------------|------------------|------------|
| C | (100) | 0.89 | 4.57 | 9.9 | 10.1 | 0.190 |
| | (110) | 1.26 | 7.17 | 19.7 | 19.9 | 0.170 |
| Si | (100) | 1.36 | 4.25 | 12.6 | 12.7 | 0.170 |
| | (110) | 1.92 | 6.37 | 22.9 | 23.0 | 0.145 |
| Ge | (100) | 1.41 | 8.04 | 23.6 | 23.8 | 0.161 |
| | (110) | 2.00 | 14.2 | 41.2 | 41.2 | 0.112 |
| W | (100) | 1.58 | 34.7 | 86.8 | 86.9 | 0.122 |
| | (110) | 2.24 | 49.5 | 138.6 | 138.6 | 0.096 |

Table 2.1: Parameters of Pöschl-Teller potential for C, Si, Ge and W. Table adapted from book [32].

2.6 Channeling in bent crystals

The channeling process can occur in bent crystals provided several conditions are met. In order for a projectile to be captured into a channeling mode the local direction of a bent plane or axis should be within a Lindhard angle parallel to a direction of a beam. Another important factor of channeling in bent crystals is the presence of a centrifugal force. The motion of a projectile on a trajectory with finite curvature radius R leads to the centrifugal force $F_c = \varepsilon/R$.

For the projectile to stay in a channeling mode the following condition should be met [32]:

$$C = \frac{\varepsilon}{RU'_{max}} \ll 1 \quad (2.46)$$

where U'_{max} is the maximum module of gradient of the potential energy surface. In the case of periodically bent crystals the bending profile can be described in the following form:

$$y = a \cos\left(\frac{2\pi z}{\lambda}\right) \quad (2.47)$$

where a is the amplitude of bending, λ is the period of bending and y and z refer to coordinates. In this case the curvature radius of bending is changing from the minimum value $\lambda^2/(4\pi^2a)$ up to infinity (straight segments). The segments with lowest curvature radius lead to the maximum of dechanneling and therefore this minimal radius should be used for calculation of C in this case.

The channeling in bent crystals was studied both experimentally and theoretically. For uniformly bent crystals experimentally this effect was studied for protons [85], pions [86] and electrons [27, 87]. Theoretical studies were performed also for protons [88, 89], electrons and positrons [90, 47, 45, 46].

The results of the simulation of the channeling in bent crystals are presented in this thesis in the Chapter 5, the results for periodically bent crystals are given in the Section 5.2. The influence of the periodic bending on rechanneling is studied in the Section 5.4.

2.7 Bent crystals production methods

The experimental study of interaction of beams with bent and periodically bent crystalline medium require efficient, precise and affordable methodology of producing specific bending of initial crystals. Three main approaches are practiced nowadays: mechanical bending, epitaxial formation of constantly bent crystals with variable concentration of doped atoms and acoustic dynamical bending of the medium.

High energy beams require micro radian level of bending of crystals. Such high precision of mechanical bending can be achieved using advanced technologies like quasi-mosaic crystals, relying on mechanical anisotropy of crystalline silicon [91, 92, 87]. In Figure 2.9 the use of quasi-mosaic crystals for accurate bending of a crystal is illustrated. In the paper [93] the detailed description of the process of manufacturing of bent oriented Si crystals for channeling experiments is given.

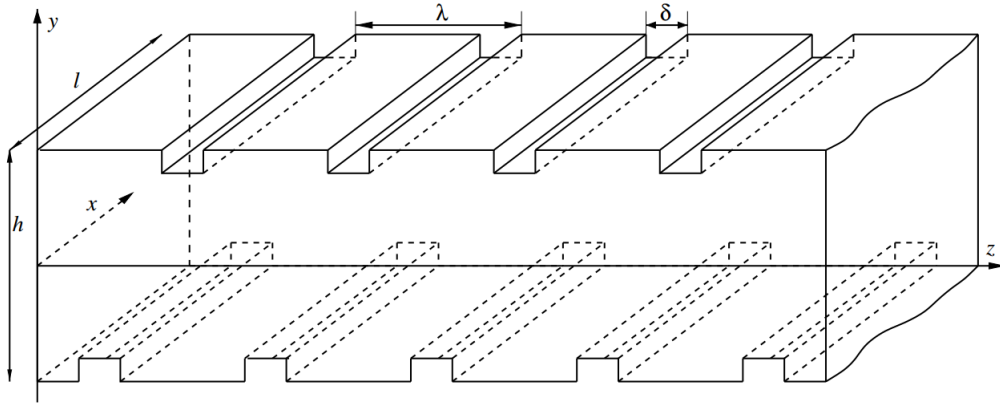


Figure 2.8: Schematic representation of a crystal with periodic surface deformations (the sets of regularly spaced grooves parallel to the x direction): λ stands for the period of deformations and δ denote the width of a groove. The set on the lower surface is shifted by $\lambda/2$ (along the z -axis) with respect to that on the upper surface. The surface stress gives rise to the periodic bending of crystallographic planes in the bulk of crystal. Figure adapted from paper [94].

The second variant of mechanical bending of crystals is to use periodic surface deformations described in papers [94, 95]. The deformation of the surface of the medium leads to slight bending of the internal volume of crystalline medium due to surface tension effect. This approach was applied in several experimental studies [96, 97, 98] and can be implemented by use of superficial grooves [23, 21], laser ablation [95] or film deposition [99]. In Figure 2.8 the schematic representation of a

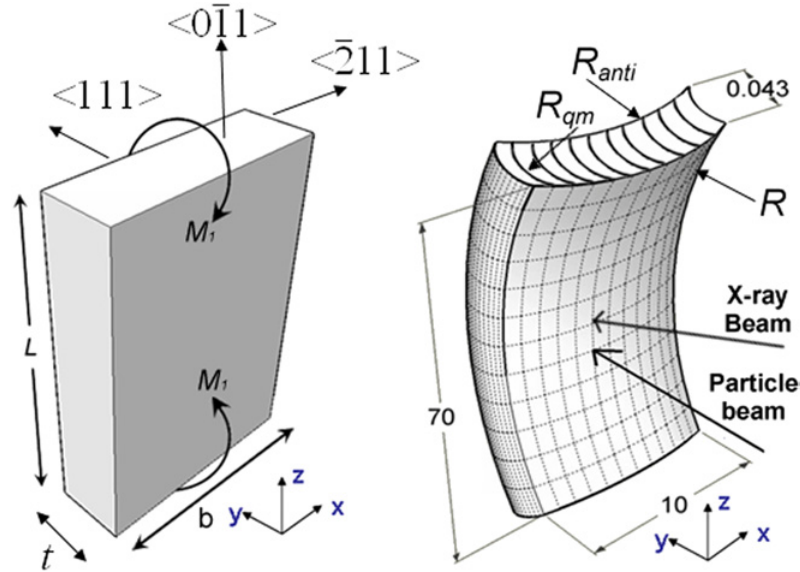


Figure 2.9: High precision method of mechanical bending of crystal described in paper by V. Guidi, A. Mazzolari, D. De Salvador and A. Carnera [92]. (a) Sketch of the unbent silicon plate with height L and thickness t with the $\langle 111 \rangle$ crystallographic axis along the y axis. As a couple of forces with momentum M_1 is exerted at its edges crystal bends as in b. (b) External forces generate a primary curvature with radius R , which results in a secondary curvature with radius R_{qm} due to anisotropy-induced deformation. Unwanted anticlasic deformation with radius R_{anti} also appears as a result of primary bending. Figure adapted from paper [92].

crystal with periodic surface deformations is presented.

Another approach to creation of bending of a crystalline medium was described in the paper by U. Mikkelsen and E. Uggerhøj [100]. In this method individual sections of the superlattice are deformed by growing $\text{Ge}_x\text{Si}_{1-x}$ superlattices on a Si substrate, where x is varied along the crystal length to generate the desired shape of the crystal.

Si and Ge crystals share same diamond crystalline lattice type, and have similar but different lattice parameter. The technology of construction of such superlattices is based on precise growth control of concentration of atoms on each layer of atoms. Using well-known methods of crystal growing (like molecular beam epitaxy or chemical vapor deposition, see the references in paper [101]), it is possible to add single crystal layers onto a substrate. The gradient of the concentration of Ge leads to the variable lattice parameter of resulting superlattice. In the papers [100, 25] the examples of application of such crystals to the experiments on crystalline undulator

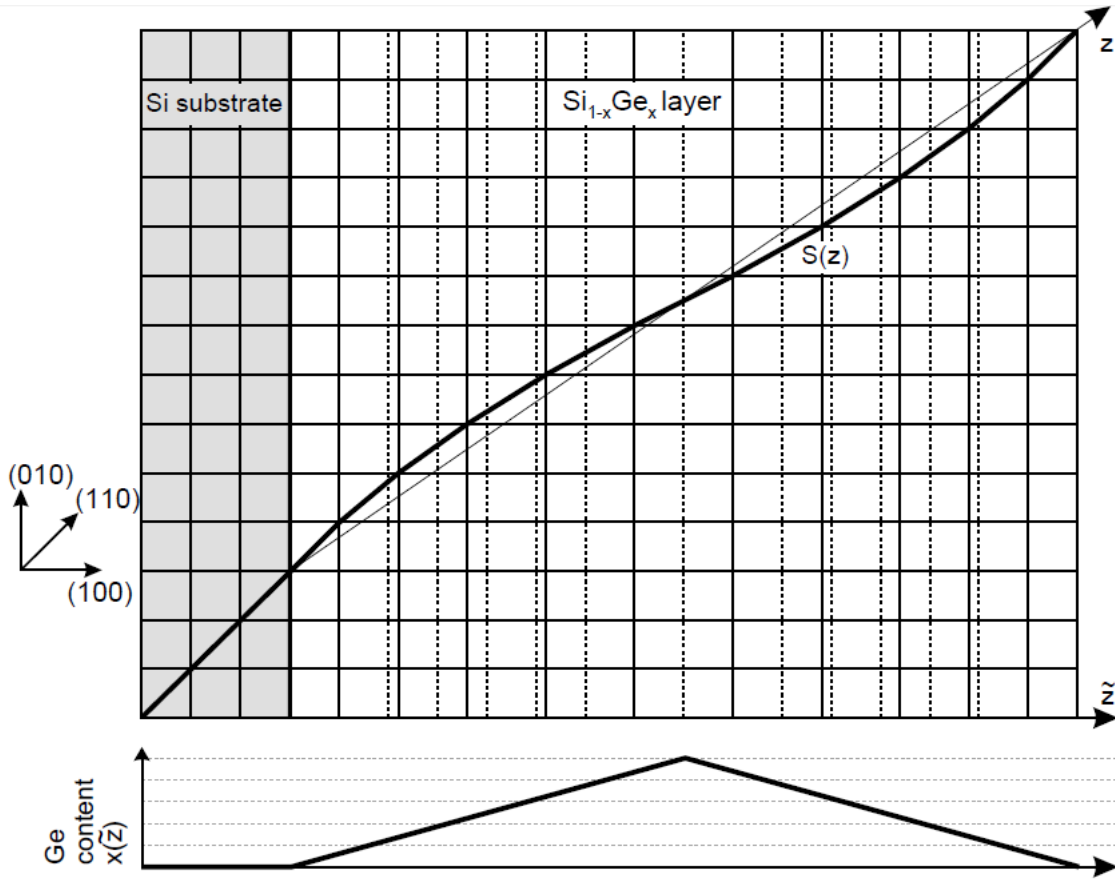


Figure 2.10: Scheme of $\text{Ge}_x\text{Si}_{1-x}$ crystalline superlattice bending due to variation of concentration of Ge atoms. Figure adapted from paper [102].

are provided.

In the paper [102] the dependence of concentration of Ge atoms in a $\text{Ge}_x\text{Si}_{1-x}$ superlattice for sine bending profile of bending is given. The schematic view of this function is provided in Figure 2.10. A set of constraints on a concentration profile is described in the paper [102]. The influence of concentration on dechanneling length and radiation spectrum is studied in this work further in the Section 6.2.

The third approach to bending of crystalline medium is to create acoustic waves in the material [103] e.g. using piezo crystals and electromagnetic fields. This approach allows dynamical change of parameters of the crystal to tune parameters of the particles propagation.

2.8 Overview of existing simulation methods

The simulation of channeling and related phenomena was implemented using different theoretical approaches in several software packages. Depending on a type of a projectile, its energy and the complexity of crystalline medium different methods can be applied. The simplest model is to use an average potential of interaction of a projectile with crystalline planes. This approach allows calculating amplitudes and frequencies of channeling oscillations depending on projectile energy and the depth of the potential well.

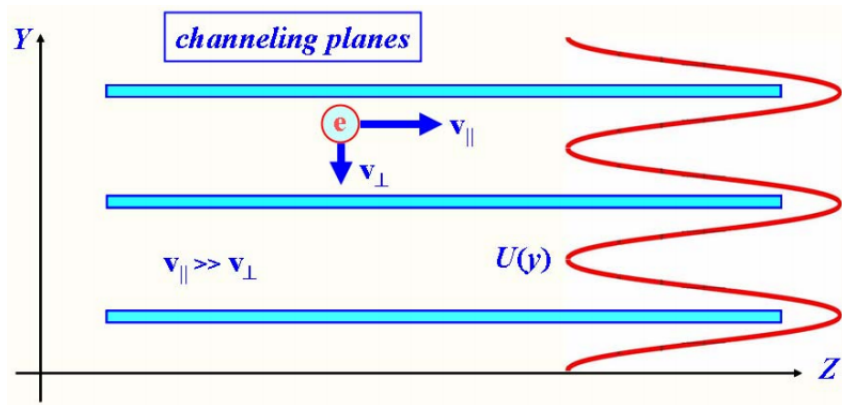


Figure 2.11: Motion model of planar channeled relativistic charged particle in a crystal, picture adapted from paper [104].

Basic Channeling with Mathematica The computer code "Basic Channeling with Mathematica" described in the paper [104] uses the method of continuous potential for analytic solution of channeling related problems. It provides following functions:

1. calculation of planar periodic potential function for chosen set of crystallographic planes of desired crystal (only Si, LiF and Ge are available);
2. computation of classical trajectories of channeled charged particles in defined periodic potential function;
3. computation of eigenvectors (i.e. wave functions) and eigenvalues (i.e. energy levels) of channeled electrons (positrons) transverse motion in defined periodic potential function;

4. calculation of transverse energy levels initial populations;
5. calculation of transitions matrix elements of channeled electrons (positrons)

In Figure 2.11 the model of motion of relativistic projectile in the average potential of the crystal is illustrated. Within this model the parallel component of velocity is considered constant. The perpendicular motion of a projectile is studied as a one-dimensional quantum mechanics problem with periodic potential energy.

CRYSTAL A CRYSTAL simulation code for particle tracking in crystals was introduced in the paper [88]. Its essence consists in both adequate and fast sampling of proton trajectories in crystals which is crucial for both correct description of experiments and quantitative prediction of new effects.

The main concept of the CRYSTAL software is simulation of particle trajectories by solving of equations of motion. The CRYSTAL code includes both one and two dimensional models. A 2D model is used for calculation of particle motion in an axial potential $U(x, y)$ depending on transverse coordinates x and y and averaged along the longitudinal coordinate z . The planar potential $U(x)$ is obtained by averaging along the coordinate y . In both cases the potential is averaged over thermal vibrations. The relativistic Lorentz equation is solved numerically by the 4th order Runge-Kutta method 3/8 rule.

DYNECHARM++ A toolkit for the simulation of coherent interactions between high-energy charged projectiles with complex crystalline structures, called DYNECHARM++ has been developed and is described in the paper [40]. The code has been written in C++ language taking advantage of this object-oriented programming method. The code is capable to evaluating the electrical characteristics of complex atomic structures and to simulate and track the particle trajectory within them. Calculation method of electrical characteristics based on their expansion in Fourier series has been adopted. Two different approaches to simulate the interaction have been adopted, relying on the full integration of particle trajectories under the continuum potential approximation and on the definition of cross-sections of coherent processes. Finally, the code has proved to reproduce experimental results and to simulate interaction of charged particles with complex structures.

The DYNECHARM++ code is based on the full solution of the equation of motion in the continuum potential and allows the computation of electric characteristics

of the crystal through the ECHARM (Electrical CHARacteristics of Monocrystals) calculation method described in the paper [105]. Therefore, the density as a function of transverse energy for complex atomic structures and for many planes and axes can be computed.

The study of radiation spectra was implemented in this software package recently [106] and this module is called RADCHARM++. In the RADCHARM++ routine, the model for the computation of electromagnetic radiation generation is based on the direct integration of the quasiclassical formula of Baier and Katkov [78].

GEANT4 Based on a continuum potential approximation model, an extension of the Geant4 toolkit [107, 108] has been developed and was described in the paper [90]. GEANT4 (for GEometry ANd Tracking) is a platform for "the simulation of the passage of particles through matter," using Monte Carlo methods. It is the successor of the GEANT series of software toolkits developed by CERN, and the first to use object oriented programming (in C++). Its development, maintenance and user support are taken care by the international Geant4 Collaboration. Application areas include high energy physics and nuclear experiments, medical, accelerator and space physics studies. The software is used by a number of research projects around the world.

The model allows the manipulation of particle trajectories by means of straight and bent crystals and the scaling of the cross sections of hadronic and electromagnetic processes for channeled particles.

Binary collisions model Another approach to channeling description was implemented in the Monte-Carlo code described in the paper by Kostyuk, Korol, Solovyov and Greiner [109]. Due to the high speed of the projectile, its interaction time with a crystal atom is very short. The atomic electrons have no time to move during the interaction. As a result, the projectile 'sees' a 'snapshot' of the atom: the atomic electrons are seen as point-like charges at fixed positions around the nucleus.

The propagation of a projectile in this case is described as a sequence of binary collision with these charges. The use of binary collision model of interaction of a projectile with fixed charges allows very fast calculation of a trajectory but leads to an overestimation of a dechanneling rate. While the nucleus of an atom can be considered as a fixed in space due to a high mass, the use of fixed electron positions leads to an unrealistic description of a binary collision. The collisions in this case

lead to higher deflection angle of a projectile and therefore faster dechanneling. In more details this problem was described in the appendix to the paper [44].

Atomistic molecular dynamics approach The atomistic molecular dynamics approach for simulation of propagation of relativistic projectiles was implemented using MBN Explorer software. It implements the simulation of the motion of the projectile by solution of three-dimensional classical relativistic equations of motion. The interaction of the projectile with the medium is simulated as an interaction with several neighbor atoms of crystalline lattice using screened Coulomb's potential (in Molière [49] or Pacios [50] variants). The details of this approach are discussed in Chapter 3.

The use of atomistic approach allows to study propagation of projectiles in amorphous medium, planar and axial channels by changing medium orientation and application of addition modifiers (for amorphous case, see Section 3.2). Such universality can't be achieved using average potential models due to use of different energy potential surfaces.

The better description as compared with [109] is achieved due to accounting for the interaction with several neighbor atoms instead of one, and also due to exploiting the atomic potential concept instead of accounting for the binary collisions with the randomly distributed point-like frozen single electrons.

Chapter 3

Theoretical and computational methods

In this chapter a description of the theoretical methods used in this work is provided. In order to simulate propagation of the relativistic projectiles the relativistic equations of motion (2.5) are to be integrated using high precision integration algorithm. In this work the fourth-order Runge-Kutta integration algorithm is used which is described in the Section 3.1. In order to describe the medium the dynamic generation algorithm is used, which uses a set of rules to determine positions of atoms around any given point in space. This algorithm is described in the Section 3.2. The interaction of the projectile with atoms of the medium can be described using an interaction potential. Two forms of this interaction description are given in Section 3.3.1 and Section 3.3.2 which correspond to Molière and Pacios potentials. The detailed comparison of the results of the simulations with these two potentials is given further in the Section 5.1.3. The interaction between atoms of the medium is the subject of the Section 3.4. In this section the Stillinger-Weber manybody potential is described, which is applied in the Section 6.1 to modeling of Si-Ge crystalline structure formation. In the Section 3.5 the description of statistical properties of channeling process is provided.

3.1 Runge-Kutta integrator for relativistic equations of motion

The relativistic equations of motion (2.5) can be written in the following form of:

$$\dot{\mathcal{Y}} = f(t, \mathcal{Y}). \quad (3.1)$$

Here dot indicates the time derivative of y which is defined as

$$\mathcal{Y} = \begin{bmatrix} \mathbf{v} \\ \mathbf{r} \end{bmatrix}, \quad f(t, \mathcal{Y}) = \begin{bmatrix} \frac{1}{m\gamma} \left(\mathbf{F}(\mathbf{r}) - \frac{\mathbf{v}(\mathbf{F}(\mathbf{r}) \cdot \mathbf{v})}{c^2} \right) \\ \mathbf{v} \end{bmatrix}. \quad (3.2)$$

Differential equation (3.1) can be solved numerically. Since the equation is non-linear, to permit higher precision, MBN EXPLORER utilizes the well-known Runge-Kutta scheme for numerical integration [110]. The following protocol is used in MBN EXPLORER:

1. The Runge-Kutta method requires specification of initial conditions for each simulation step, i.e., as a time instant t , for each particle experiencing relativistic motion $\mathcal{Y}(t) = \mathcal{Y}_0$. The initial conditions are used to progress the system in time.
2. For each particle experiencing relativistic motion calculate a set of intermediate variables

$$\begin{aligned} k_1 &= f(t, \mathcal{Y})\Delta t & k_2 &= f(t + \Delta t/2, \mathcal{Y} + k_1/2)\Delta t \\ k_3 &= f(t + \frac{1}{2}\Delta t, \mathcal{Y} + \frac{1}{2}k_2)\Delta t & k_4 &= f(t + \Delta t, \mathcal{Y} + k_3)\Delta t. \end{aligned} \quad (3.3)$$

3. Expressions defined in equations (3.3) are then used to calculate velocities \mathbf{v} and positions \mathbf{r} of relativistic particles at a time instant $t + \Delta t$. This is achieved by evaluating $\mathcal{Y}(t + \Delta t)$ as follows

$$\mathcal{Y}(t + \Delta t) = \mathcal{Y}(t) + \frac{1}{6}(k_1 + 2k_2 + 2k_3 + k_4). \quad (3.4)$$

The calculated $\mathcal{Y}(t + \Delta t)$ are used to compute velocities $\mathbf{v}(t + \Delta t)$ and positions $\mathbf{r}(t + \Delta t)$, which then in turn are used to define the initial condition y_0 above for the subsequent simulation step.

To maintain the computational accuracy the energy conservation is checked at every integration step. If the relative difference of the total system's energy exceeds a

pre-defined threshold value, the simulation step is repeated with a two times smaller time step. The procedure is continued until either the desired precision is reached or the step size reaches its minimal allowed value.

3.2 Dynamic generation of crystal structure

To simulate propagation of particles through medium one has to specify its structure. It can be done using the crystal generation technique, which is available in the MBN EXPLORER.

A structure of the crystal is defined by a unit cell, three translational vectors and the numbers of translations along each vector. If any of the latter numbers is not implicitly given, the crystal spreads in the corresponding direction along the entire computational box, which has to be specified.

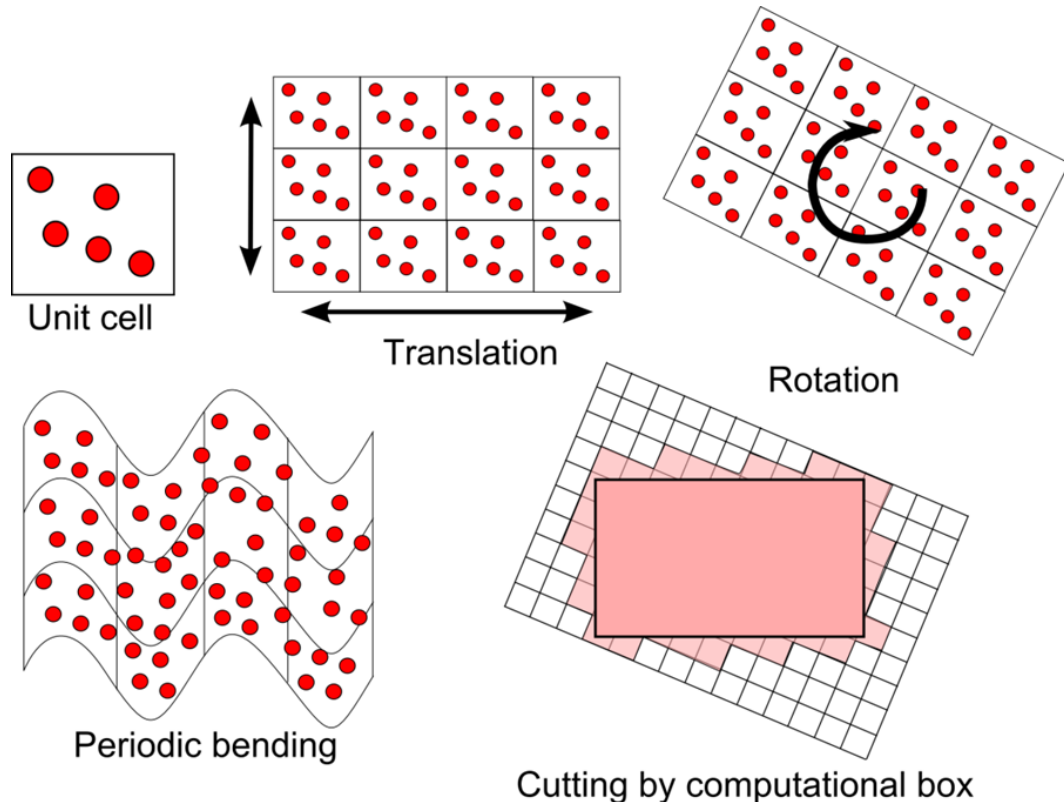


Figure 3.1: Description of a crystalline medium is done through the definition of unit cell of the crystal and a set of reversible transformations. This approach allows efficient mapping of coordinates into crystalline reference frame i.e. cutting the periodic crystalline structure by a simulation box.

The crystalline structure generated with MBN EXPLORER permits several build-in modifiers which can be used to tune the generated structure in a desired fashion:

- Translation of each atom of the original unit cell to a set of displaced atoms with a constant displacement vector \mathbf{d} .
 $\mathbf{r} \mapsto \{\mathbf{r}, \mathbf{r} + \mathbf{d}, \mathbf{r} + 2\mathbf{d}, \dots, \mathbf{r} + (n - 1)\mathbf{d}\}$, where Cartesian components of $\mathbf{d} = (d_x, d_y, d_z)$ are parameters of the modifier.

- Rotation of atoms and of the coordinate frame.
 $\mathbf{r} \mapsto (\mathbf{r} \cdot \mathbf{t}_1, \mathbf{r} \cdot \mathbf{t}_2, \mathbf{r} \cdot \mathbf{t}_3)$, where $\mathbf{t}_1 = \frac{\mathbf{t}_3 \times \mathbf{t}_2}{|\mathbf{t}_3 \times \mathbf{t}_2|}$, $\mathbf{t}_2 = \frac{\mathbf{y}'}{|\mathbf{y}'|}$, $\mathbf{t}_3 = \frac{\mathbf{z}'}{|\mathbf{z}'|}$, $\mathbf{z}' = (z'_x, z'_y, z'_z)$, $\mathbf{y}' = (y'_x, y'_y, y'_z)$ with y' and z' are parameters of the modifier.

- Exclusion of atoms located outside of two parallel planes.
 $p_1 < \mathbf{r} \cdot \mathbf{n} < p_2$, where $\mathbf{n} = (n_x, n_y, n_z)$ is the unit normal vector of a plane, p_1 and p_2 are parameters of the modifier.

- Periodic displacement of atoms using a sine-function.
 $\mathbf{r} \mapsto \mathbf{r} + \mathbf{a} \sin(\mathbf{k} \cdot \mathbf{r} + \varphi)$, where $\mathbf{a} = (a_x, a_y, a_z)$ is the amplitude, the wave-vector $\mathbf{k} = (k_x, k_y, k_z)$ defines the spatial period, and φ defines the phase shift; \mathbf{a} , \mathbf{k} and φ are parameters of the modifier.

- Random displacement of atoms using normal distribution.
 $\mathbf{r} \mapsto \mathbf{r} + (\mathcal{N}(0, \sigma), \mathcal{N}(0, \sigma), \mathcal{N}(0, \sigma))$, where σ is the parameter of the modifier defining standard deviation of distribution.

- Random substitution of atoms in initial structure with new atoms of the specific type with specified probability e.g. $\text{Si} \mapsto \text{Ge}$

These transformations are reversible and therefore allow efficient construction of consistent crystal structure at any position in space. In Figure 3.1 schematic illustration of these transformations is presented. For any region in space these reverse transformations give a set of coordinates in a reference frame of the crystal (oriented

along translational vectors), then for these coordinates a new set of atoms is created and all these transformations are applied to the coordinates of atoms.

Once the nodes are defined, the position vectors of the atomic nuclei are generated with account for random displacement Δ_j from the nodal positions due to thermal vibrations. The Cartesian components $\Delta_{j\alpha}$, $\alpha = x, y, z$, are normally distributed:

$$w(\Delta_{j\alpha}) = \frac{1}{\sqrt{2\pi u_T^2}} \exp\left(-\frac{\Delta_{j\alpha}^2}{2u_T^2}\right). \quad (3.5)$$

Here u_T is the root-mean-square amplitude of thermal vibrations. Its values for various crystals at room temperature can be found in [2].

To simulate the propagation of a particle through a crystal of finite thickness L a new type of boundary conditions, the so-called "dynamic simulation box", has been implemented in MBN EXPLORER. This algorithm, illustrated in Figure 3.2, implies the following. The use of such approach instead of periodic boundary conditions allows to avoid parasitic periodicity of the grid vibrations and also allows to specify more complex crystalline structures e.g. with multiple layers.

3.3 Interaction of the projectile with the medium

The interaction of atoms of the medium with a projectile within atomistic approach is described using interaction potentials. The force acting on a projectile is a sum of forces of interaction with single atoms of the medium. These forces are calculated as a gradient of interaction potential energy. Atoms of Si in crystalline medium interact with projectiles as screened charges. In order to describe this interaction two interaction potentials were tested: Molière potential [49] and Pacios potential [50]. Detailed description of these potentials is provided below.

3.3.1 Molière potential

The Molière potential [49] is a parametrization which describes interaction between a projectile and a neutral atom. It can be written in the following form:

$$U(r) = \frac{qZe}{r} \sum_{k=1}^3 \alpha_k e^{-\frac{\beta_k r}{aTF}} \quad (3.6)$$

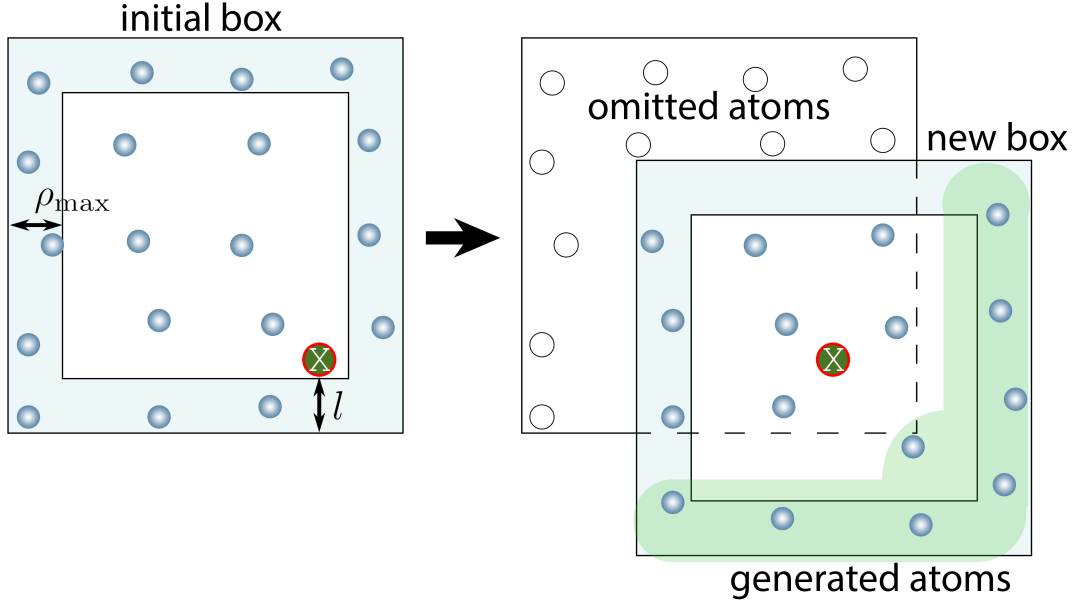


Figure 3.2: Illustration of the dynamic simulation box algorithm. When a projectile X-marked approaches the face of the initial simulation box (left panel) by a distance $l \approx \rho_{\max}$ a new simulation box of the same size is generated (right panel) with the particle placed approximately in its geometrical center. The atoms (small shadowed circles) located in the intersection of the old and the new boxes are not changed. In the rest part of the new box the atomic positions are generated anew as described in the text. Figure adapted from paper [44].

where $\alpha_k = (0.35, 0.55, 0.1)$, $\beta_k = (0.3, 1.2, 6.0)$, a_{TF} is the Thomas-Fermi radius of an atom, Ze is the charge of the atom nucleus and q is the charge of the projectile. The Thomas-Fermi radius a_{TF} is related to the Bohr radius a_0 via $a_{TF} = 0.8853Z^{1/3}a_0$.

The force acting on the projectile due to the electrostatic interaction with atom in this case is calculated according to the definition in Eq. (3.7) as

$$\mathbf{F} = -\frac{qZe}{r^3}\mathbf{r}\sum_{k=1}^3\alpha_k e^{-\frac{\beta_k r}{a_{TF}}}(\beta_k r + 1). \quad (3.7)$$

In left panel of Figure 3.3 the comparison of the potential energy of interaction of C, Si and Ge atoms with positron described by Molière potential is illustrated. For all these types of atoms the potential energy decreases exponentially and is negligible on the distance of 5-6 Å. In this work the typical value of the cutoff distance was taken as 5 Å.

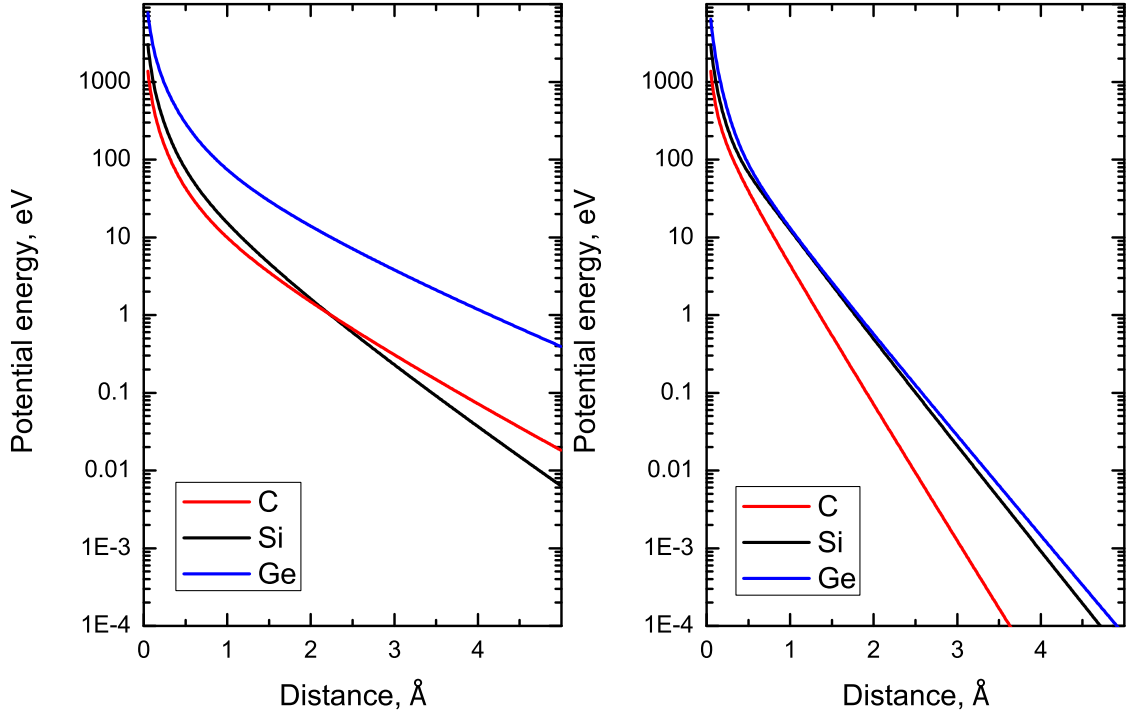


Figure 3.3: Comparison of the potential energy of interaction of C, Si and Ge atoms with positron described by Molière potential (left) and Pacios potential (right).

3.3.2 Pacios potential

The Pacios potential [50] is another type of the potential implemented in MBN EXPLORER to describe the pairwise interaction between a charge projectile and a neutral atom. It has the following form:

$$U(r) = \sum_{k=1}^4 \frac{\alpha_k}{\beta_k^3} (2 + \beta_k r) e^{-\beta_k r} \frac{4\pi}{r} \quad (3.8)$$

where Ze is the charge of the atom nucleus and q is the charge of the projectile. In Table 3.1 the values of α_k and β_k of the Pacios interaction potential from the original paper are presented for C, Si and Ge atoms.

The force acting on the projectile due to the electrostatic interaction with atom in this case is calculated according to the definition in Eq. (3.9) as

$$\mathbf{F} = - \sum_{k=1}^4 \frac{\alpha_k}{\beta_k^3} (2 + 2\beta_k r + \beta_k^2 r^2) e^{-\beta_k r} \frac{4\pi}{r^3} \mathbf{r}. \quad (3.9)$$

In right panel of Figure 3.3 the comparison of the potential energy of interaction

| Type | Param. | $i = 1$ | $i = 2$ | $i = 3$ | $i = 4$ |
|------|------------|----------|-----------|-----------|----------|
| C | α_i | 128.0489 | -2.535155 | 2.041774 | - |
| | β_i | 11.84981 | 3.508196 | 2.099930 | - |
| Si | α_i | 1713.363 | 158.9419 | -107.9461 | 1.348130 |
| | β_i | 29.95277 | 4.305803 | 3.906608 | 1.627379 |
| Ge | α_i | 20901.16 | 1399.193 | 169.1339 | 0.991756 |
| | β_i | 68.65812 | 22.95161 | 5.903443 | 1.541315 |

Table 3.1: Parameters α_i , β_i in the analytic expansion, for C, Si and Ge atoms from original paper [50].

of C, Si and Ge atoms with positron described by Pacios potential is illustrated. For all these types of atoms the potential energy decreases exponentially and is negligible on the distance of 3-4 Å. In this work the typical value of the cutoff distance was taken as 4 Å.

The Moliere and Pacios potentials are both applicable for the simulation of the channeling process. In this work both potentials were used in order to check if the choice of the potential affects the results of simulations. The direct comparison of results is done for the case of bent Si crystal in Section 5.1.3, and it shows no major difference neither in dechanneling length estimation nor in radiation spectrum.

3.4 Stillinger-Weber potential for classical MD

The simulation of the structure of Si and Ge as well as of binary Si-Ge crystals by means of molecular dynamics can be done using different potentials. The most precise classical approach for these carbon-like materials is to use bond-ordered potentials: Tersof [111, 112], Brenner [113] and Stillinger-Weber [57]. Bond-ordered potentials take into account not only pairwise interaction forces between particles, but also angles between bonds between neighboring particles. The overview of parameters of these potentials is provided in Refs. [114, 115]. The Stillinger-Weber potential can be written in the following form:

$$U = \sum_{i,j(i<j)} U_2(i,j) + \sum_{i,j,k(i<j<k)} U_3(i,j,k) \quad (3.10)$$

where

$$\begin{aligned}
 U_2(i, j) &= \epsilon_{ij} A \left(B \left(\frac{r_{ij}}{\sigma_{ij}} \right)^{-p} - \left(\frac{r_{ij}}{\sigma_{ij}} \right)^{-q} \right) \exp \left[\left(\frac{r_{ij}}{\sigma_{ij}} - a \right)^{-1} \right], \frac{r_{ij}}{\sigma_{ij}} < a \\
 U_3(i, j, k) &= \epsilon_{ijk} h \left(\frac{r_{ij}}{\sigma_{ij}}, \frac{r_{ik}}{\sigma_{ik}}, \theta_i \right) + \epsilon_{jik} h \left(\frac{r_{ji}}{\sigma_{ji}}, \frac{r_{jk}}{\sigma_{jk}}, \theta_j \right) + \epsilon_{kij} h \left(\frac{r_{ki}}{\sigma_{ki}}, \frac{r_{kj}}{\sigma_{kj}}, \theta_k \right) \\
 h \left(\frac{r_{ij}}{\sigma_{ij}}, \frac{r_{ik}}{\sigma_{ik}}, \theta_i \right) &= \lambda_{ijk} \exp \left(\gamma \left[\left(\frac{r_{ij}}{\sigma_{ij}} - a \right)^{-1} + \left(\frac{r_{ik}}{\sigma_{ik}} - a \right)^{-1} \right] \right) \left(\cos \theta_i + \frac{1}{3} \right)^2
 \end{aligned}$$

Parameters A , B , p , q , and a are positive constants, parameter ϵ determines the energy scale, σ determines length scale. For binary systems like Si-Ge: $\epsilon_{ij} = \sqrt{\epsilon_i \epsilon_j}$, $\epsilon_{ijk} = \sqrt{\epsilon_{ij} \epsilon_{jk}}$, $\sigma_{ij} = (\sigma_i + \sigma_j)/2$, $\lambda_{ij} = \sqrt{\lambda_i \lambda_j}$, $\lambda_{ijk} = \sqrt{\lambda_{ij} \lambda_{jk}}$.

3.5 Analysis of channeling fractions and calculation of dechanneling length

The direct result of the simulation of propagation of the projectile is its trajectory. The following values and fractions will be used in order to characterize the channeling effect: N_0 - total number of simulated trajectories, $N_c(z)$ - number of projectiles in a channeling mode at the depth z , $N_{c1}(z)$ - number of projectiles in a primary channeling mode, $n(z) = N_c(z)/N_0$ - fraction of particles in a channeling mode in any channel, $n_1(z) = N_{c1}(z)/N_0$ - fraction of particles in a channeling mode in primary channel, this characteristic excludes rechanneling effect.

In order to quantitatively describe channeling the following characteristics are used: acceptance \mathcal{A} - fraction of particles that start channeling right from the beginning of the crystal ($N_c(0)/N_0$), L_{p1} - mean value of the primary channeling segments, L_{p2} - mean value of all channeling segments, L_d - characteristic dechanneling length in exponential approximation: $n_1(z) = \mathcal{A} \exp(-z/L_d)$, where $n_1(z)$ is the fraction of projectiles in a primary channel.

3.5.1 Calculation of statistical error for channeling fraction

The dependence of channeling fraction on penetration distance $n(z)$ can be analyzed based on calculated trajectories of projectiles. These trajectories are in channeling mode at different positions in the crystal, therefore statistical averaging is needed in

order to determine the channeling fraction of a whole beam. Consider the following expression for channeling fraction as a random value: $n(z) = \sum_{part.} M(z)/N$, where $M(z) = 1$ if particle is in the channeling mode and $M(z) = 0$ if particle is not captured.

The variance of this value $\sigma(z)$ can be calculated using following expression:

$$\sigma(z) = \sqrt{\frac{1}{N} \sum_{part.} (M(z) - n(z))^2}. \quad (3.11)$$

The number of particles N_1 for which $M(z) = 1$ is equal to $n(z)N$, number of particles N_0 for which $M(z) = 0$ is equal to $(1 - n(z))N$.

$$\sigma(z) = \sqrt{\frac{1}{N} (n(z)N(1 - n(z))^2 + (1 - n(z))N(0 - n(z))^2)} \quad (3.12)$$

This equation can be simplified to the following form:

$$\sigma(z) = \sqrt{n(z)(1 - n(z))} \quad (3.13)$$

In order to calculate statistical error for the channeling fraction $n(z)$ one should multiply $\sigma(z)$ by the Student's coefficient [116], corresponding to the confidence probability. In this work the confidence probability $\alpha = 0.999$ was used and the coefficient value of 3.3 was taken:

$$Err(z) = 3.3\sqrt{n(z)(1 - n(z))/N} \quad (3.14)$$

The value of the statistical error is relatively small for $n(z) \rightarrow 0$ and $n(z) \rightarrow 1$ and has the maximum value for $n(z) \approx 0.5$. The decrease of the statistical error with N is rather slow and therefore the number of trajectories should be rather big for precise simulations. One can estimate that for the error below 5 % one should calculate approximately 1000 trajectories, the error below 1 % the number of trajectories should be increased to 30000. In this work the typical number of trajectories used for analysis of dechanneling length was on the order of 3000-10000 which corresponds to relative error on the level of 2-3 %.

Chapter 4

Computational studies of channeling processes within the atomistic approach

In this chapter results of a series of numerical calculations are presented. In the Section 4.1 the results of the simulation of propagation of electrons and positron through the amorphous medium are provided. The results are compared with calculations using Bethe-Heitler approximation in terms of radiation spectrum. The Section 4.2 describes results of simulation of planar channeling of 855 MeV and 6.7 GeV electrons and positrons in the Si (110) plane. The Section 4.3 describes results of simulations of channeling in axial case. These results were previously described in the paper [62] which is in the process of publication.

4.1 Amorphous medium case study

In order to verify the model described in Chapter 3 consider propagation of the relativistic projectiles through amorphous medium. As the case study the propagation of 6.7 GeV electrons and positrons through 105 μm amorphous samples was considered. The amorphous medium was generated by random placement of atoms with average density corresponding to the crystalline materials. Results of the simulations were compared to the results obtained within the analytical Bethe-Heitler approximation theory described in Section 2.3. The results are given in Figure 4.1.

In this figure the results for both electrons and positrons are provided. In the

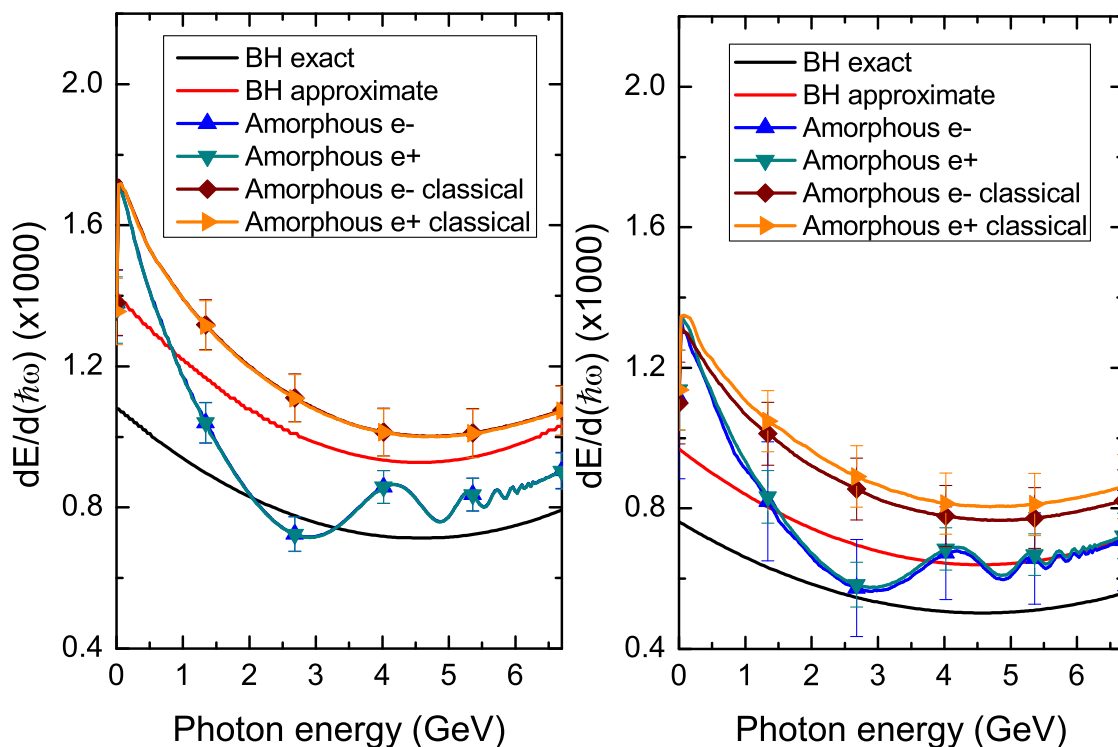


Figure 4.1: The comparison of the radiation spectrum simulations in silicon (left) and carbon (right) using the direct simulation of projectiles and analytic Bethe-Heitler theory. The spectrum was calculated for the beams of electrons and positrons propagating through $105 \mu\text{m}$ thick amorphous medium sample. The results for quasi-classical and approximate classical variants of spectrum calculation are provided.

case of amorphous medium the projectile experiences a series of random scattering events on atoms of the medium. The frequency of these processes and the change of the momentum do not depend on the sign of the charge of the projectile, therefore the emitted radiation spectrum is also the same for positive and negative projectiles.

The results of the calculation for quasi-classical and approximate classical variants of spectrum calculation are provided. The classical case corresponds to $u \rightarrow 0$ case in the Eq. (2.16). The significant difference between these cases can be seen for energies above 0.5 GeV.

For Bethe-Heitler calculations two types of approximations are provided. Exact corresponds to factor \mathcal{F} given by Eq. (2.39). Approximate corresponds to factor \mathcal{F} given by Eq. (2.42). In both cases Bethe-Heitler approximation gives an estimation based on crosssection of a single scattering process, which also gives an approximate result. The comparison of results of simulations with Bethe-Heitler approximation

shows, that in this case the "approximate" variant is in a better agreement with result of the simulations. The average difference between these approximations and results of the simulation is 20% for the "exact" variant and 10% for "approximate". Further in this work the calculation of Bethe-Heitler radiation spectrum are given in "approximate" variant.

4.2 Planar channeling

In this section the results of simulation of planar channeling of electrons and positrons within the atomistic approach are described. In the first subsection the results of simulations [46, 44] of 855 MeV electrons and positrons are given. In the second subsection the results of simulations [44] of 6.7 GeV projectiles are described and compared with the experimental measurements in terms of radiation spectrum.

4.2.1 Results for 855 MeV electrons and positrons

Consider a charged projectile propagating inside a crystalline plane. As a case study channeling of 855 MeV electrons and positrons in Si(110) and Si(111) planar channels was simulated. Si(110) planes form a set of equal channels with interplanar distance of 1.92 Å. Si(111) planar channel contains two (111) planes separated by the distance $d = 0.784$ Å. Total width of the channel is $d = 3.136$ Å. The presence of two planes of crystal atoms in a single channel leads to specific features of the channeling oscillations for both negatively and positively charged projectiles. These features are absent in the case of channeling along (100) or/and (110) planes. To discuss qualitatively the channeling oscillations of an electron and a positron we refer to Figure 4.2, which presents the Si(111) interplanar potential U calculated in the continuous approximation [1] with the use of the Molière atomic potential.

In the case of electron channeling (left panel in Figure 4.2) the interplanar potential has two wells symmetrically separated with respect to the midplane, where the potential has a local maximum U_0 . At the borders of the channel, i.e. at the distances $\pm d/2$, the potential has maxima U_{\max} which exceed U_0 . As a result, if the transverse energy ε_{\perp} of an electron satisfies the condition $\varepsilon_{\perp} < U_0$ then the channeling oscillations are restricted to one of the wells. In the case $\varepsilon_{\perp} > U_0$ the particle oscillates with larger amplitude within $[-d/2, d/2]$. The electron interplanar potential is strongly anharmonic, therefore, the period of oscillations depends

on the amplitude. On average, the large-amplitude oscillations are slower than the small-amplitude ones in the vicinity of the local minima.

The positron interplanar potential is presented on the right panel of Figure 4.2. In this case, the potential also has two wells although strongly asymmetric. Both of the wells can be approximated by parabolic dependencies. The frequency of channeling oscillations in the narrow (and shallow) well is approximately 2 times larger than that in the wide well.

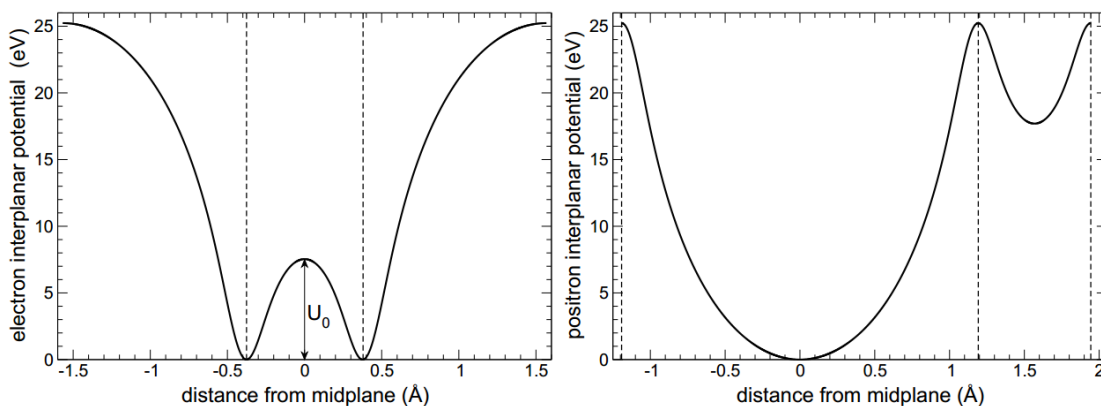


Figure 4.2: Electron (left panel) and positron (right panel) continuous Molière interplanar potential for Si(111). Vertical dashed lines mark the positions of the atomic planes. The curves correspond to the crystal temperature 300 K. Figure adapted from paper [46].

In Figure 4.3 a set of trajectories of 855 MeV positrons channeling along Si(111) direction is presented. Horizontal lines indicate the (111) planar channels (planes of atoms). The data refer to the straight crystal of the length $L = 100 \mu\text{m}$.

For positrons, noticeable are nearly harmonic oscillations. Two types of oscillations, occurring in the wide part of the channel and in the narrow as well, are clearly seen in the presented trajectories. Another feature of positron channeling through a $L = 100 \mu\text{m}$ thick crystal is a comparatively small number of the dechanneling events. This is also not surprising if one compares the crystal size with the dechanneling length $L_d \approx 700 \mu\text{m}$ for a 855 MeV positron in Si(111). The latter value can be obtained using Eq. (1.50) from [117] with the correction for a light projectile introduced in [118]. Therefore, it is not surprising that most of the incident particles traverse the crystal in the channeling mode.

Much less regular are the channeling oscillations of electrons, see Figure 4.4. The electron trajectories exhibit a broader variety of features: channeling motion, over-

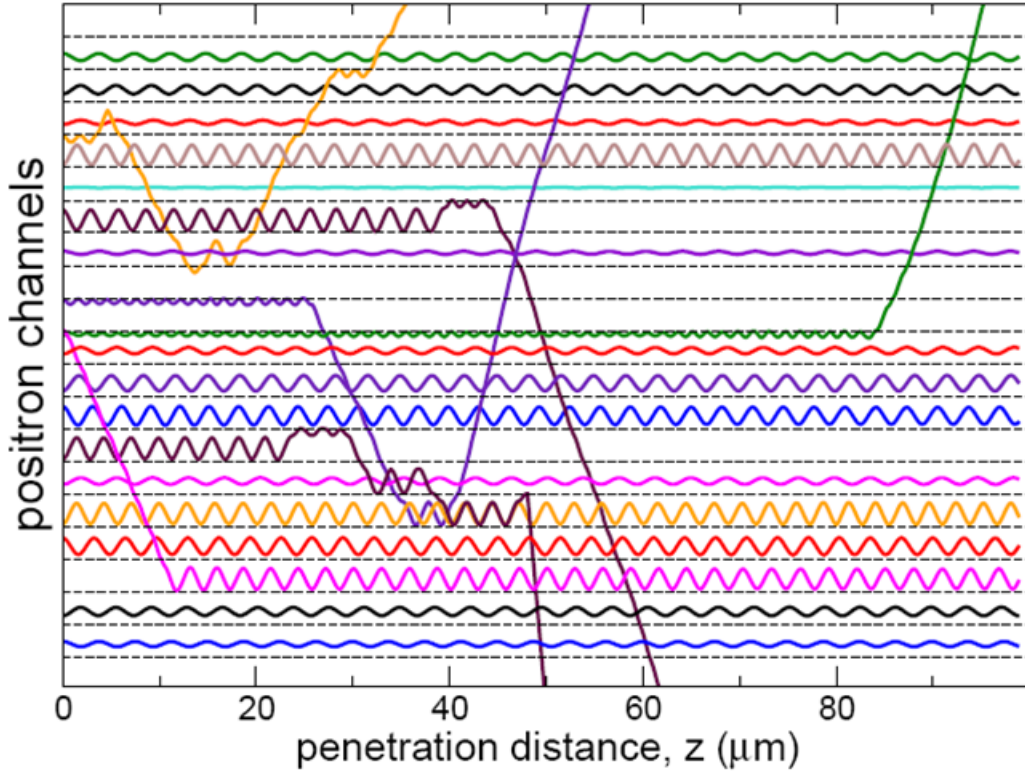


Figure 4.3: Channeling of 855 MeV positrons in a 100 μm thick silicon crystal. The plots show randomly chosen trajectories of the particles initially collimated along Si(111) crystallographic planes. Horizontal dashed lines indicate the (111) planar channels separated by the distance $d = 3.136 \text{ \AA}$. Figure adapted from paper [46].

barrier motion, rechanneling process, rare events of hard collisions etc. First, let us note that the dechanneling length of a 855 MeV electron in Si(111), estimated with the help of Eq. (10.1) from [78], is $L_d \approx 23 \mu\text{m}$. Therefore, it is not surprising that the events of channeling through the whole crystal are quite rare. On the other hand, the events of rechanneling, i.e., capture to the channeling mode of an over-barrier particle, are quite common for electrons. Even the multiple rechanneling events are not rare. This phenomenon has been already noted in the simulations of the electron channeling [44, 119] with a qualitative explanation provided [119] of the difference in the rechanneling rate for positively and negatively charged projectiles. Also it is worth noting a visible anharmonicity in the channeling oscillations of electrons which is a direct consequence of a strong deviation of the electron interplanar potential from a harmonic shape. As a result, the period of the oscillations varies with the amplitude. Similar to the positron channeling, two types of oscillations, related to

the two wells structure of the interplanar potential (see Figure 4.4), are clearly seen in the presented trajectories.

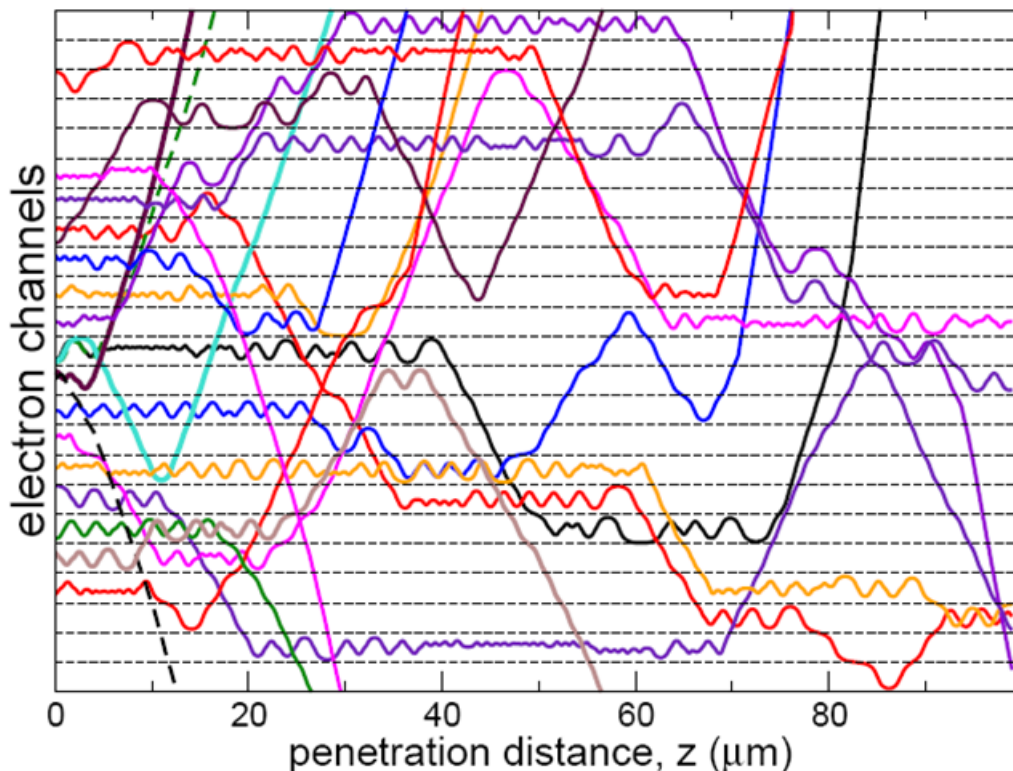


Figure 4.4: Channeling of 855 MeV electrons in a 100 μm thick silicon crystal. The plots show randomly chosen trajectories of the particles initially collimated along Si(111) crystallographic planes. Horizontal dashed lines indicate the (111) planar channels separated by the distance $d = 3.136 \text{ \AA}$. Figure adapted from paper [46].

The simulated trajectories were used to estimate the dechanneling length (in the case of the electron channeling) and to calculate spectral distribution of the emitted radiation.

To quantify the electron dechanneling process we calculated two penetration lengths introduced in Ref. [44]. The first one, notated below as L_{p1} was found as a mean value of the primary channeling segments, which started at the entrance and lasted till the dechanneling point somewhere inside the crystal. Generally speaking, this quantity is dependent on the angular distribution of the particles at the entrance. The L_{p1} values quoted below were obtained for a zero-emittance beam collimated initially along the (111) planar direction. The second penetration depth, L_{p2} , is defined as a mean value of all channeling segments, including those which appear

| Plane | \mathcal{A} (%) | L_{p1} (μm) | L_{p2} (μm) |
|-------|-------------------|----------------------------|----------------------------|
| (111) | 74 | 18.4 ± 0.8 | 15.5 ± 0.5 |
| (110) | 65 | 11.7 ± 0.6 | 10.9 ± 0.3 |

Table 4.1: The penetration lengths L_{p1} , L_{p2} and acceptance \mathcal{A} for $\varepsilon = 855$ MeV electrons in straight Si(111) and Si(110) crystals. The crystal thickness is $L = 50 \mu\text{m}$.

due to the rechanneling. In the rechanneling process an electron is captured into the channeling mode having, statistically, an arbitrary value of the incident angle ψ not greater than Lindhards critical angle. Therefore, L_{p2} mimics the penetration depth of the beam with a non-zero emittance $\approx \psi_L$.

The results for L_{p1} and L_{p2} , together with the calculated values of the channel acceptance $\mathcal{A} = N_{acc}/N_0$ (where N_0 and N_{acc} are numbers of the incident and the accepted particles, respectively), are summarized in Table 4.1.

For a straight crystal, it is instructive to compare the obtained values $L_{p1} = 18.70 \pm 0.69$ and $L_{p2} = 15.92 \pm 0.40 \mu\text{m}$ with the dechanneling lengths for the initial beam, $L_{d0} = 13.57 \pm 0.12 \mu\text{m}$, and for the rechanneled particles, $L_d = 13.69 \pm 0.07 \mu\text{m}$ obtained in Ref. [119]. The calculations performed in the cite paper were based on the peculiar model of the elastic scattering of an ultra-relativistic projectile from the crystal constituents. The model substitutes the atom with its snapshot image: the atomic electrons are treated as point-like charges placed at fixed positions around the nucleus. The interaction of an ultra-relativistic projectile (e.g., an electron) with each atomic constituent is treated in terms of the classical Rutherford scattering. In Ref. [44] it was demonstrated, that such a snapshot model noticeably overestimates the mean scattering angle in the process of elastic scattering in a single electron-atom collision. The mean square angle for a single scattering is a very important quantity in the multiple-scattering region, where there is a large succession of small-angle deflections symmetrically distributed about the incident direction. It was noted in Ref. [44] that the snapshot approximation underestimates the dechanneling length of 855 MeV electrons in straight Si (110) by approximately 30 per cent. Similar to this, the Si(111) data from [119], undervalues the dechanneling length presented in Table 1: L_{d0} is less than L_{p1} by $37 \pm 5\%$ whereas L_d is $17 \pm 3\%$ smaller than L_{p2} .

Let us note that the obtained length $L_{p1} = 18.70 \pm 0.69 \mu\text{m}$ is in agreement with the value $18.8 \mu\text{m}$ evaluated recently in Ref. [36] from the solution of the Fokker-Plank equation.

The simulated trajectories were used to compute spectral distribution of the emitted radiation following the formalism and algorithm described in detail in Ref. [44]. The results are presented in Figure 4.6. The calculated spectral intensities are normalized to the Bethe-Heitler values (see, for example, Ref. [80]) and, thus, are plotted as the enhancement factors over the bremsstrahlung spectrum in amorphous silicon. Statistical uncertainties due to the finite number ($\approx 3000\dots 4000$) of the analyzed trajectories are indicated by the error bars. The calculations were performed for two detector apertures: $\theta_{max} = 0.21$ and 2 mrad. The first value, which is close to the aperture used in the experiments with the 855 MeV electron beam [120, 54], is much smaller than the natural emission angle $\gamma^{-1} \approx 0.6$ mrad. Therefore, the corresponding spectra refer to nearly forward emission. On the contrary, the second angle greatly exceeds γ^{-1} , so that the cone θ_{max} collects nearly all emitted radiation.

Figures 4.5 and 4.6 present the enhancement of radiation in straight silicon crystals.

First, we note that for both electrons and positrons the intensity of radiation in the oriented crystal greatly exceeds (by more than an order of magnitude) the bremsstrahlung background. The enhancement comes from the particles moving along quasi-periodic channeling trajectories, which bear close resemblance with the undulating motion. As a result, constructive interference of the waves emitted from different but similar parts of the trajectory are added coherently. For each value of the emission angle θ the coherence is most pronounced for the radiation into harmonics, which frequencies can be estimated as (see, e.g., [78]):

$$\omega_n = \frac{2\gamma^2 \Omega_{ch}}{1 + \gamma^2 \theta^2 + K_{ch}^2/2} n, \quad n = 1, 2, 3, \dots, \quad (4.1)$$

where Ω_{ch} is the frequency of channeling oscillations and $K_{ch}^2 = 2\gamma^2 \langle v_{\perp}^2 \rangle / c^2$ is the mean square of the undulator parameter related to them. Within the framework of continuous potential approximation, these quantities are dependent on the magnitude of the transverse energy which, in turn, determines the amplitude of oscillations.

Different character of channeling by positrons and electrons results in differences in the spectra of the channeling radiation.

The nearly perfect sine-like channeling trajectories of positrons lead to the emission spectrum close to that of the undulator radiation with $K^2 \ll 1$. Two peaks in

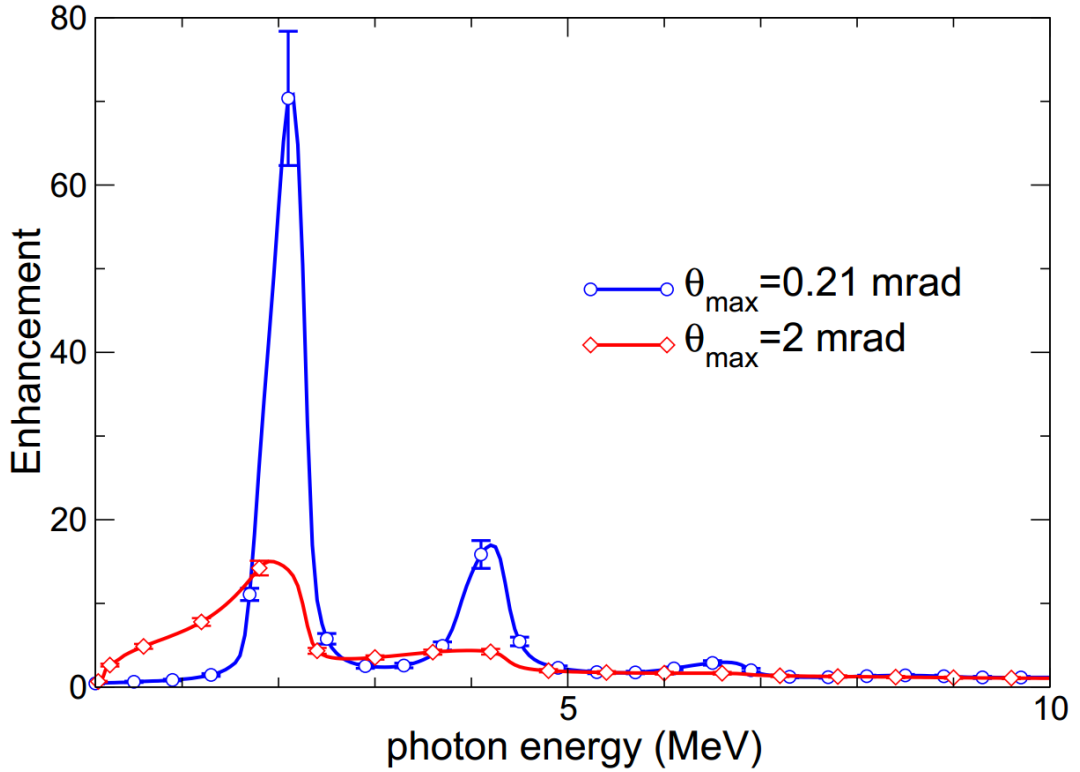


Figure 4.5: Enhancement factor for 855 MeV positrons channeled in $L = 50 \mu\text{m}$ crystalline target along Si(111) planes calculated for two values of the maximum emission angle as indicated. Figure adapted from paper [46].

the positron spectrum, see Figure 4.5, is due to two types of channeling oscillations mentioned above. The peak at ≈ 2 MeV is due to the emission in the fundamental harmonic ($n = 1$) from the trajectories corresponding to the channeling motion in the wide well of the positron Si(111) channel (see Figure 4.2 right). It is more pronounced for the smaller aperture, since in this case a strong inequality $(\gamma\theta)^2 \ll 1$, valid for all angles $\theta < \theta_{max}$, ensures the independence of ω_1 on the emission angle. The second less accented peak corresponds to the emission in the first harmonic due to the channeling motion in the narrow part of the channel. In this case, the amplitudes are smaller (this result in the decrease of the intensity) but the channeling frequencies are higher leading to the higher value of ω_1 . For the larger aperture, a big part of the energy is radiated into the cone $\gamma^{-1} < \theta < \theta_{max}$. For these relatively large emission angles the first harmonic energy decreases with θ . As a result, the peaks become broader and less intensive.

Due to strong anharmonicity of the electron channeling oscillations, the peaks

in the spectrum of channeling radiation are less pronounced even for the small aperture, see Fig. 4.6 left. For the large aperture $\theta_{max} = 2$ mrad the second peak is completely smeared out. The right panel in the figure illustrates the differences in the emission spectra (for the small aperture) for electron channeling in Si(111) and Si(110) channel (the calculations of the latter were performed in [44]). The Si(110) channel can be modeled as a single-well interplanar potential which leads to a single peak in the emission spectrum.

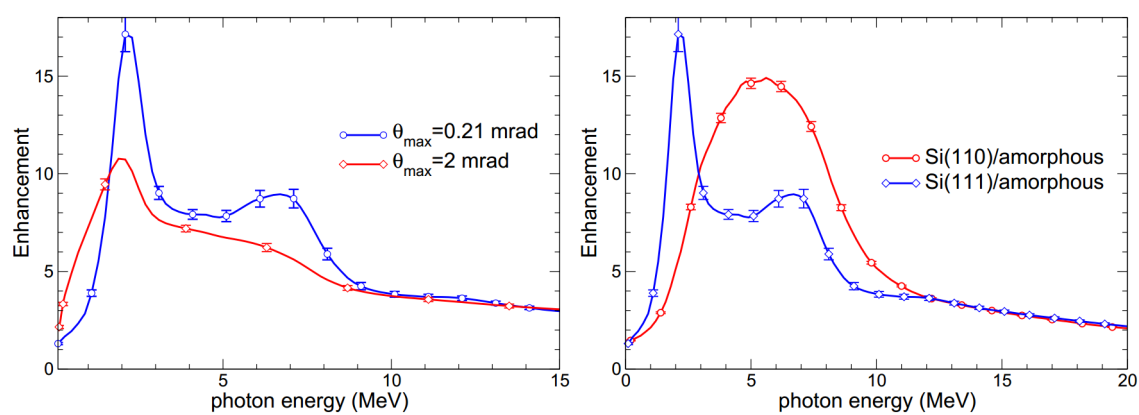


Figure 4.6: Left panel. Enhancement factors, calculated for two indicated apertures θ_{max} , for 855 MeV electron channeling in $L = 50 \mu\text{m}$ straight Si crystal along (111) planes. Right panel. Enhancement factor for 855 MeV electrons channeled in $L = 50 \mu\text{m}$ straight silicon crystal along (110) and (111) planes. The data refer to $\theta_{max} = 0.21$ mrad. Figure adapted from paper [46].

4.2.2 Results for 6.7 GeV electrons and positrons

For the Si(110) planar orientation, both positrons and electrons exhibit channeling motion as it is illustrated in Figure 4.7 by sets of typical simulated trajectories.

For positrons, noticeable are nearly harmonic oscillations between the neighboring planes. This is in accordance with a well-known result established within the framework of the continuum model of channeling (see, e.g., [2]). Indeed, for a positively charged projectile the interplanar potential can be approximated by parabola in most part of the Si(110) channel. Therefore, the channeling oscillations are very close to the harmonic type. Another feature of positron channeling through a $L = 105 \mu\text{m}$ thick crystal is a small number of the dechanneling events (the two examples presented in the figure were found in forty randomly chosen trajectories). This is also not surprising if one compares the crystal size with the dechanneling

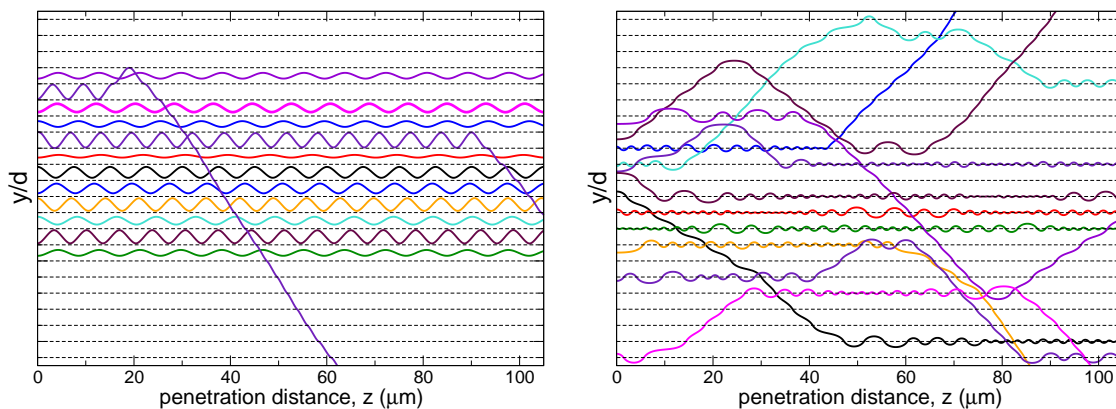


Figure 4.7: Channeling of 6.7 GeV positrons (left) and electrons (right) in a 105 μm thick silicon crystal. The plots show typical trajectories of the particles initially collimated along Si(110) crystallographic planes. Horizontal dashed lines indicate the planes separated by the distance $d = 1.92 \text{ \AA}$. Adapted from paper [44]

length $L_d \approx 0.4 \text{ mm}$ for a 6.7 GeV positron in Si(110). The latter value can be obtained using Eq. (1.50) from [117] with the correction for a light projectile introduced in [118].

Much less regular are the channeling oscillations of electrons, see Figure 4.7(right). In contrast to positrons, the electron trajectories exhibit a broader variety of features: channeling motion, over-barrier motion, rechanneling process, rare events of hard collisions etc. First, let us note that the dechanneling length of a 6.7 GeV electron in Si(110), estimated with the help of Eq. (10.1) from [78], is $L_d \approx 130 \mu\text{m}$. Therefore, it is not surprising that a noticeable fraction of electrons, although channeling in close vicinity to the plane, stays in the channeling mode from the entrance point up to the end of the crystal. The events of rechanneling, i.e., capture to the channeling mode of an over-barrier particle, are quite common for electrons. Even the multiple rechanneling events are not rare. This phenomenon has been already noted in the Monte Carlo simulations of the electron channeling [119] with a qualitative explanation provided of the difference in the rechanneling rate for positively and negatively charged projectiles. The conclusion drawn on the much lower rechanneling probability for a positron than that for an electron is clearly illustrated by comparing the trajectories on the left and right panels of the figure. Also it is worth noting a visible anharmonicity in the channeling oscillations of electrons which is a direct consequence of a strong deviation of the electron interplanar potential from a harmonic shape (see, e.g., [8]). As a result, the period of the oscillations varies with

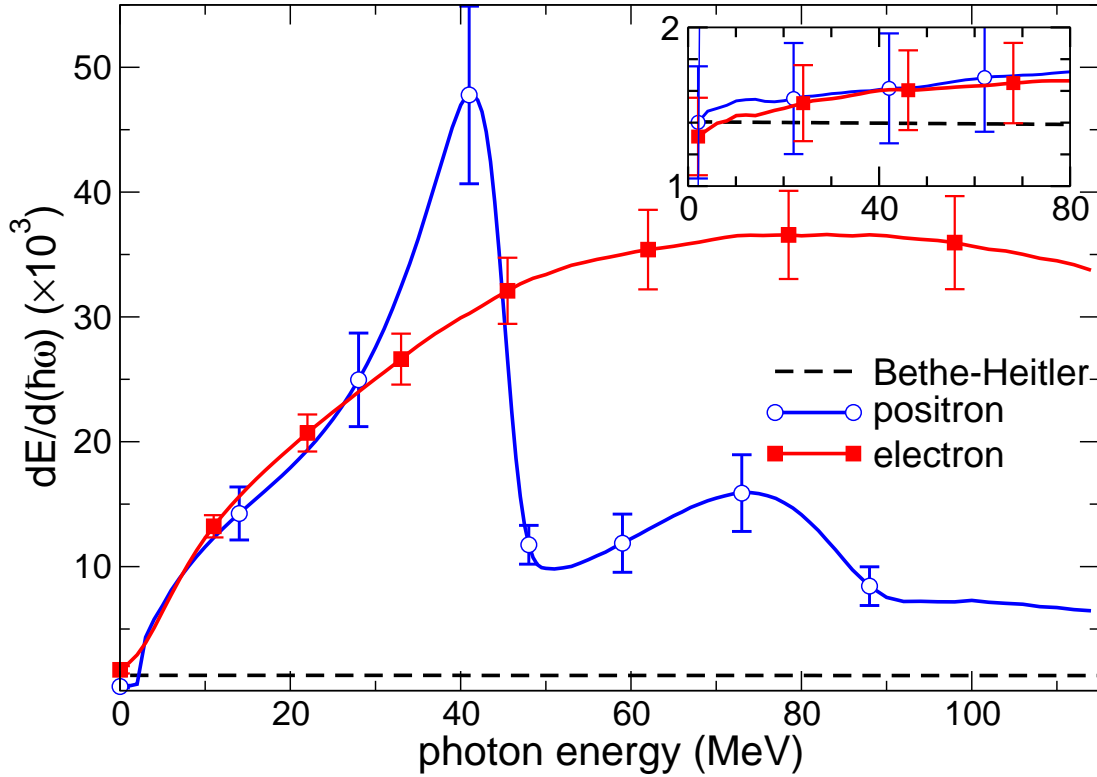


Figure 4.8: Radiation spectra from 6.7 GeV positrons and electrons (as indicated) channeling through a 105 μm thick Si(110). Dashed black line shows the Bethe-Heitler spectrum in amorphous silicon. The inset presents the spectra calculated for the simulated trajectories in amorphous Si. Adapted from paper [44]

the amplitude.

The simulated trajectories were used to calculate spectral distribution of the emitted radiation using procedure described in Section 2.2. The solid curves in Figure 4.8 represent the spectral dependencies $dE/d(\hbar\omega)$ calculated for 6.7 GeV electrons and positrons aligned along Si(110) crystallographic plane at the crystal entrance. Statistical uncertainties due to the finite number (≈ 500 in each case) of the analyzed trajectories are indicated by the error bars (the confidence interval) which correspond to the probability $\alpha = 0.999$. The spectra were computed for a detector aperture of $\theta_a = 0.35$ mrad hinted by the description of the experiments [8, 121]. This value exceeds the “natural” emission cone γ^{-1} by a factor of ≈ 5 . Therefore, the calculated curves account for nearly all emitted radiation.

First, it can be noted that for both electrons and positrons the intensity of radiation in the oriented crystal greatly exceeds (by more than an order of magnitude) that by the same projectile in an amorphous medium. The latter is indicated

by the dashed line and was calculated within the framework of Bethe-Heitler approach using Eqs. (2.42) and (2.43). The enhancement is due to the contribution to $dE/d(\hbar\omega)$ coming from the particles moving along quasi-periodic channeling trajectories, which bear close resemblance with the undulating motion. As a result, constructive interference of the waves emitted from different but similar parts of the trajectory increases the intensity. For each value of the emission angle θ the coherence effect is most pronounced for the radiation into harmonics, which frequencies can be estimated using Eq. 4.1.

Different character of channeling by positrons and electrons results in differences in the spectra of the channeling radiation.

The nearly perfect sine-like channeling trajectories of positrons lead to the emission spectrum close to that of the undulator radiation with $K^2 < 1$.¹ A pronounced peak in the photon energy range 20...45 MeV is due to the emission in the fundamental harmonic ($n = 1$). The maximum corresponds to the forward emission ($\theta = 0$) and can be estimated from (4.1) as $\hbar\omega \approx 40$ MeV. The second, less accented peak corresponds to the emission in the second harmonic.

In contrast, in the electron spectrum the undulator effect is smeared completely due to strong anharmonicity of the channeling trajectories.

In addition to the channeling spectra the spectra for amorphous Si medium was computed. For doing this, the trajectories of electrons and positrons were simulated for a random orientation of the crystal with the care taken to avoid major crystallographic directions along the beam axis. The spectral-angular distributions of the simulated radiation were integrated over $\theta_a = 0.4$ mrad aperture. The calculated spectra are compared in the inset of Figure 4.8. Remarkably, the spectra produced by positrons and electrons in amorphous Si appeared to practically coincide with each other and to agree quite well with the Bethe-Heitler result. This agreement can be considered as indicating the reliability of the numerical simulations.

By normalizing the channeling spectral intensities to the Bethe-Heitler values, the enhancement spectral factors can be obtained for the channeling radiation by the positrons and electrons. These factors were computed using two sets of the simulated trajectories for each of the projectiles. The first set, discussed above, corresponds to the case when the velocity of a projectile at the crystal entrance is parallel to Si(110) plane, i.e., the incident angle ψ is zero. The second set of the

¹Using Eq. (B.5) from [32], one estimates $K_{\text{ch}}^2 \approx 0.4$.

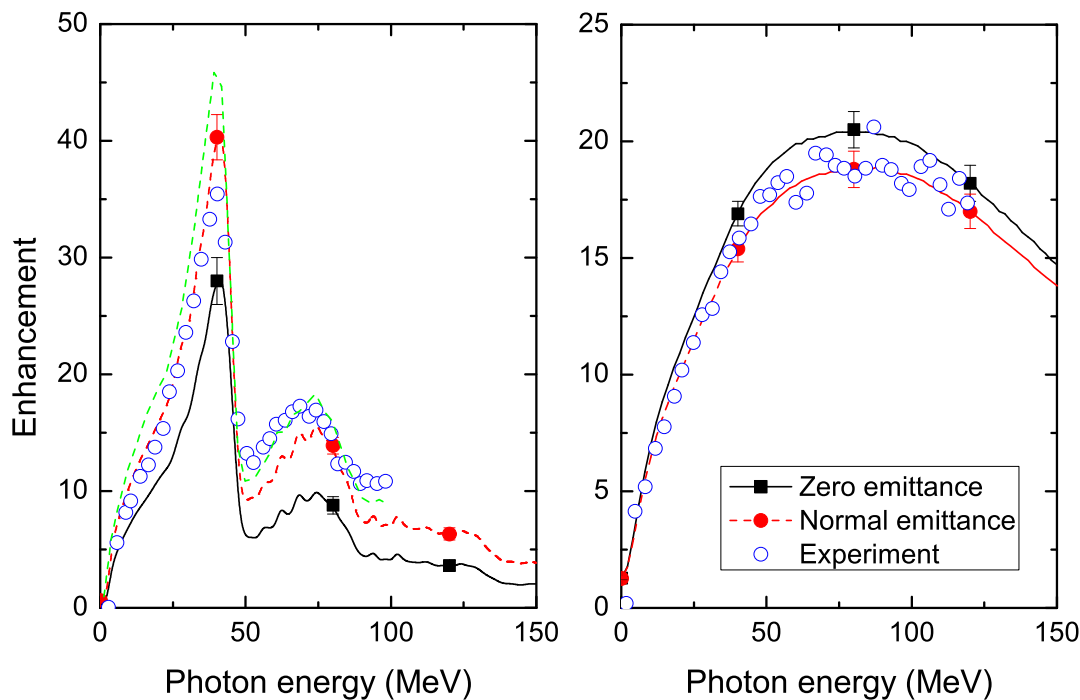


Figure 4.9: Enhancement factor of the channeling radiation over the radiation in amorphous medium spectrum. The left and right plots are for the positrons and electrons, respectively. Open circles stand for the experimental data from Ref. [8]. Solid curves correspond to the calculations shown in Figure 4.8 and correspond to the zero incident angle, $\psi = 0$. Dashed curves correspond to the calculations with the incident angle lying within $\psi = [-\psi_L, \psi_L]$ with $\psi_L = 62 \mu\text{rad}$. Green dashed line corresponds to results of simulations from the paper [35]. See also explanation in the text.

trajectories was simulated allowing the incident angle to be uniformly distributed within the interval $[-\psi_L, \psi_L]$ with $\psi_L = 62 \mu\text{rad}$ being Lindhard's planar critical value calculated in accordance with Eq. (1) from Ref. [8].

The calculated enhancement factors are compared in Figure 4.9 with the experimental results for 6.7 GeV presented in [8]² and results of the simulations for positrons from the paper [35]. The open circles stand for the experimental data obtained by digitizing Figure 12 from the cited paper. The solid and dashed curves represent the calculated dependencies for the two sets of trajectories as indicated in the caption. Figure 4.9 demonstrates that the results reproduce rather well the

²In the main text of the cited paper these data refer to 7 GeV projectiles. However, in the Note added in proof it is indicated that the actual beam momentum is 4 % lower. This is also stressed in [121] where the beam energy of 6.7 GeV, used at the experiments, is indicated.

shape of the spectra and, in the case of the positron channeling, the positions of the main and the secondary peaks. With respect to the absolute values both calculated spectra, $\psi = 0$ and $|\psi| \leq \psi_L$, exhibit some deviations from the measured dependencies.

For positrons, the curve with $\psi = 0$ perfectly matches the experimental data in vicinity of the main peak but underestimates the measured yield of the higher harmonics. Increasing the incident angle results in some overestimation of the main maximum but improves the agreement above $\hbar\omega = 40$ MeV. For electrons, the $\psi = 0$ curve exceeds the measured values, however, the increase in ψ leads to a very good agreement if one takes into account the statistical errors of the calculated dependence.

The aforementioned deviations can be due to several reasons. Modeling a crystalline field as a superposition of the atomic fields described by the Molière potentials can lead to intrinsic errors. Though the Molière approximation is a well-established and efficient approach, more realistic schemes for the crystalline fields, based, for example, on X-ray scattering factors [122, 123], can also be employed for the channeling simulations. In the Section 5.1.3 the use of the Pacios potential for these calculations is tested.

Another source of the discrepancies can be attributed to some uncertainties in the experimental set-up described in [8, 121]. In particular, it was indicated that the incident angles were in the interval $[-\psi_L, \psi_L]$ with the value $\psi_L = 62 \mu\text{rad}$ for a 6.7 GeV projectile. However, no clear details were provided on the beam emittance which becomes an important factor for comparing theory vs experiment. In the calculations a uniform distribution of the particles within the indicated interval of ψ was used, and this is also a source of the uncertainties. The spectra was also simulated for larger cutoff angle equal to $2\psi_L$ (these curves are not presented in the figure). It resulted in a considerable ($\approx 30\%$) decrease of the positron spectrum in the vicinity of the first harmonic peak.

On the basis of the comparison with the experimental data it can be concluded that the code produces reliable results and can be further used to simulate the propagation of ultra-relativistic projectiles along with the emitted radiation.

4.3 Axial channeling

In this section the results of the simulation of axial channeling are presented. In this case both positive and negative projectiles follow crystalline axes instead of planes. In the planar case the motion of a projectile is finite only in the direction, orthogonal to crystalline planes. The system of channels in this case is one-dimensional. In axial channeling case the motion of a projectile is finite in two dimensions and the system of channels is also two-dimensional. The structure of axial channels is illustrated in Figure 4.10. Each channel corresponds to a 2D geometrical shape in the plane perpendicular to the direction of the beam. Dots in this figure mark the centers of channels of corresponding sign. The borders of channels are shown with light blue lines, these borders are defined by planes on equal distances from center lines of channels.

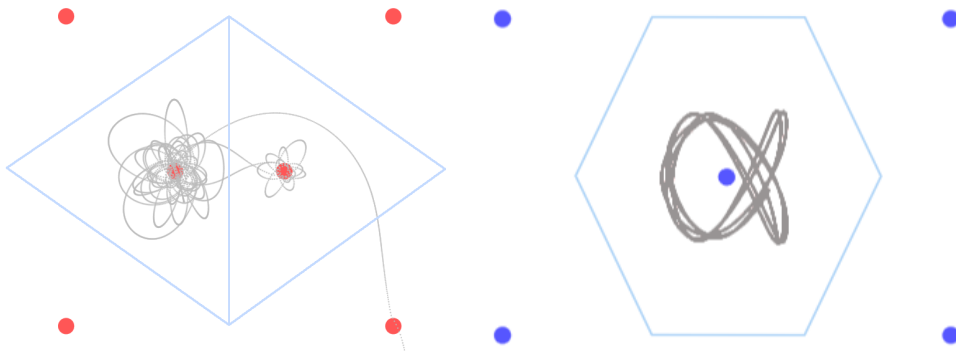


Figure 4.10: Examples of trajectories of an electron (left) and positron (right) in $\langle 110 \rangle$ axial channel in Si crystal with FCC crystal structure. These trajectories illustrate channeling regime of both particles and motion outside of the channel and rechanneling for electron. Red dots mark centers of the channels for negative projectiles, blue dots mark centers for positive projectiles.

The implemented algorithm described in Chapter 3 allows natural study of propagation of projectile in both axial and planar channels. The general algorithm of calculation of trajectories of projectiles or radiation spectrum needs no specific modification for the case of axial channeling. The only difference in algorithm is the procedure of the analysis of channeling fractions which requires taking into account the specific shape of channels in axial case.

The direct result of the simulation of the channeling is the trajectory of the projectile. Examples of such trajectories for electrons and positrons are shown in Figure 4.10 where several regimes of motion can be seen. First, the channeling

| Projectile, axis | \mathcal{A} (%) | L_{p1} (μm) | L_{p2} (μm) | L_d (μm) |
|-------------------------------|-------------------|----------------------------|----------------------------|-------------------------|
| e^- , $\langle 100 \rangle$ | 49 ± 2 | 21 ± 1 | 23 ± 1 | 15 ± 1 |
| e^- , $\langle 110 \rangle$ | 36 ± 2 | 19 ± 1 | 21 ± 1 | 13 ± 1 |
| e^- , $\langle 111 \rangle$ | 48 ± 2 | 21 ± 1 | 23 ± 1 | 14 ± 1 |
| e^+ , $\langle 100 \rangle$ | 65 ± 2 | 246 ± 5 | 111 ± 3 | 2760+ |
| e^+ , $\langle 110 \rangle$ | 77 ± 2 | 252 ± 5 | 121 ± 3 | 3670+ |
| e^+ , $\langle 111 \rangle$ | 40 ± 2 | 212 ± 8 | 63 ± 2 | 2660+ |

Table 4.2: Acceptance and mean dechanneling lengths for straight crystals in different axis for 10 GeV electron and positrons in a 320 μm thick crystal.

regime, i.e. motion near the center of the channel. Second, the over-barrier motion above the potential barrier through the crystal without capturing of the particle by channels. Third, rechanneling, i.e. recapture of the projectile by the channel. The general definitions of characteristics of axial channeling are same as described in Section 3.5

Consider axial channeling of 10 GeV electrons and positrons in Si crystal in three axial directions $\langle 100 \rangle$, $\langle 110 \rangle$, $\langle 111 \rangle$. The values of acceptance and mean dechanneling lengths are presented in Table 4.2. Three cases show very different acceptance value, and less different dechanneling lengths. These values also depend strongly on the sign of the charge of the projectile. The $\langle 110 \rangle$ axis is most favorable for positrons but least favorable for electrons. The dechanneling length for electrons is at least order of magnitude lower than for positrons due to closer passage of projectiles near the axis during channeling. The exponential approximation works well for electrons, but is not describing channeling fraction for positrons see Figures 4.11, 4.12.

For positrons the values of L_{p1} and L_{p2} are limited more by total crystal thickness of 320 μm , then by real dechanneling length. In Figure 4.12 one can see, that the channeling fractions show very little decrease even at the end of the crystal. The difference between L_{p1} and L_{p2} , and low values of L_{p2} indicate high number of rechanneling events and short channeling segments.

In order to describe difference between channeling in various channels consider the plot of average potential energy of interaction of positrons with different axes, see Figure 4.13. For electrons value of interaction energy have an opposite sign.

Most important characteristic for each channel for positrons is the difference of the potential energy between the position of equilibrium in the minimum of the potential (center of the channel) and the point on the border of two channels. This value is the depth of the potential well and its growth lowers the chance of projectile

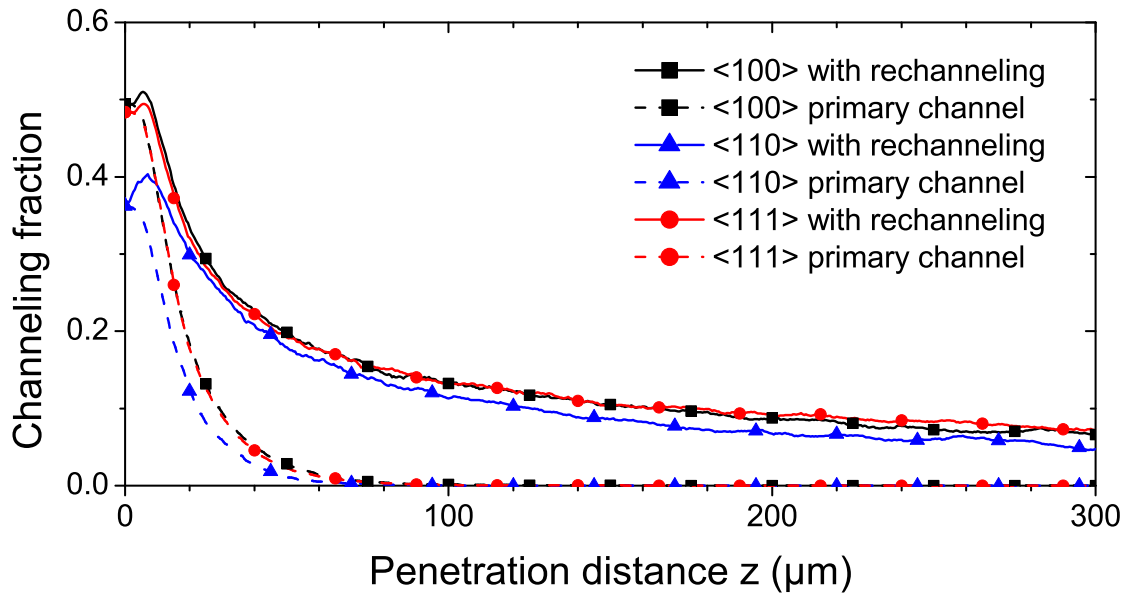


Figure 4.11: Channeling fraction for 10 GeV electrons in a 320 μm thick silicon crystal depending on penetration distance for different orientations of crystal. For each direction two fractions are calculated: with and without rechanneling.

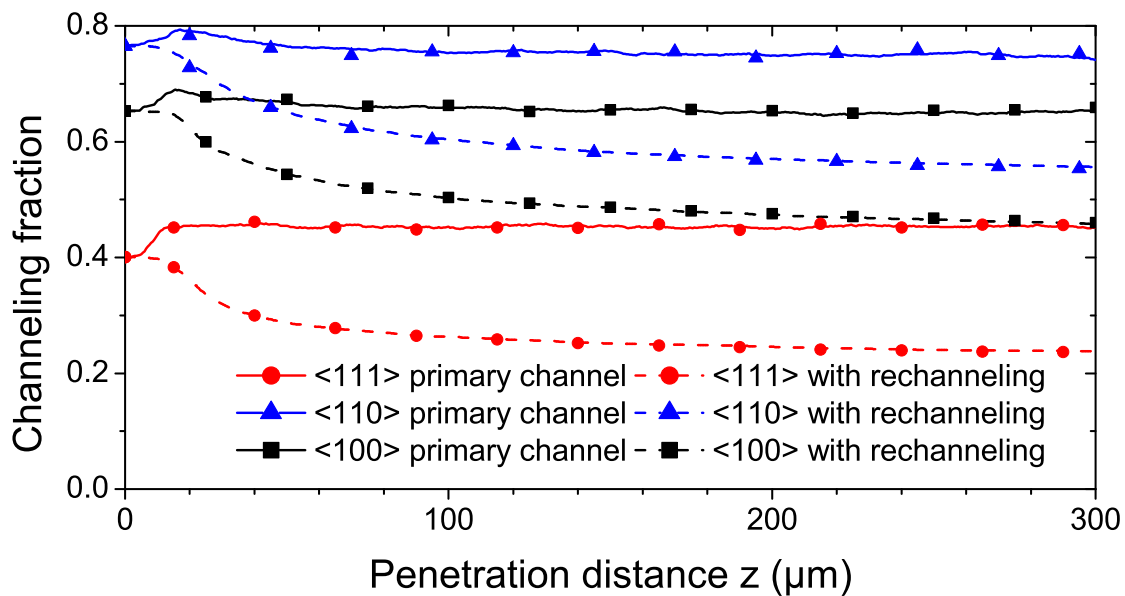


Figure 4.12: Channeling fraction for 10 GeV positrons in a 320 μm thick silicon crystal depending on penetration distance for different orientations of crystal. For each direction two fractions are calculated: with and without rechanneling.

to dechannel.

The following values were calculated for channeling of positron in different direc-

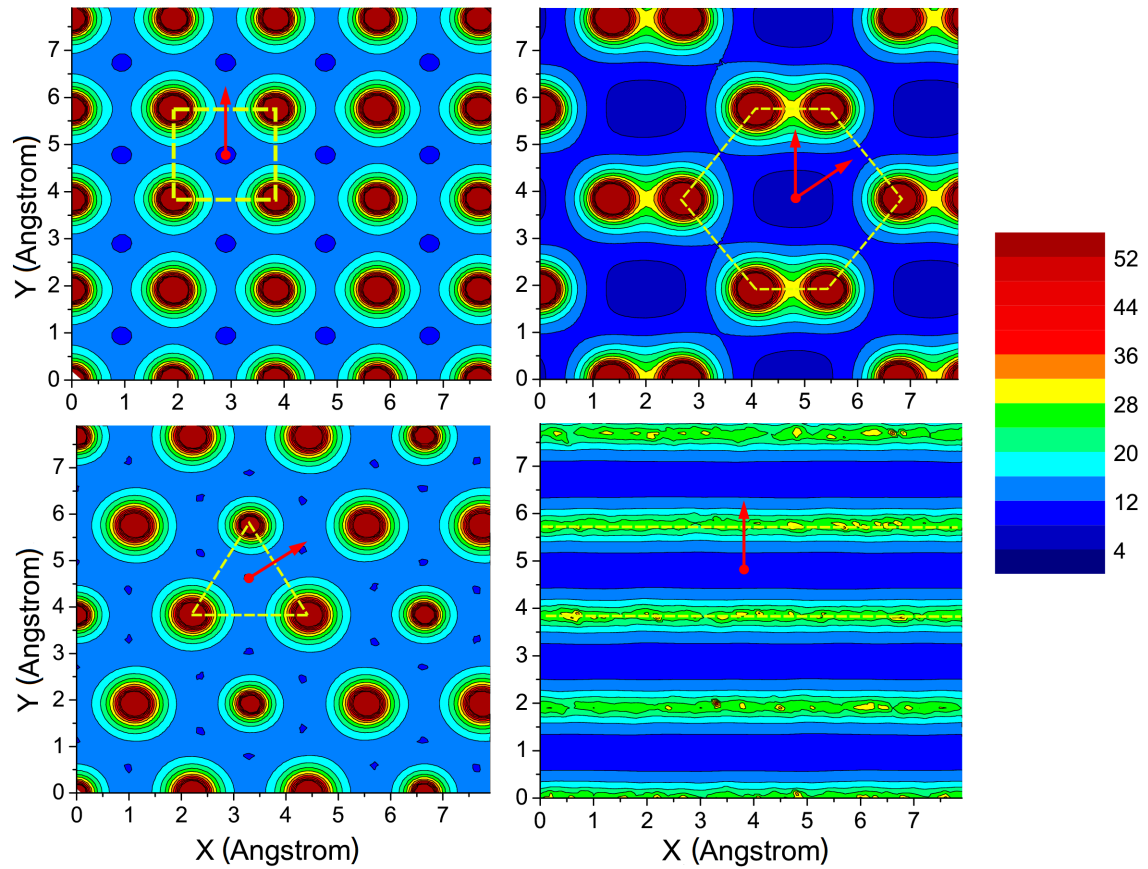


Figure 4.13: Average potential energy in eV of interaction of positrons with lines of atoms in different axes: $\langle 100 \rangle$ (top left), $\langle 110 \rangle$ (top right), $\langle 111 \rangle$ (bottom left), and (110) plane (bottom right). Dashed lines show approximate borders of channels for positrons. Arrows start from centers of channels and show characteristic directions of dechanneling.

tions: $\langle 100 \rangle$ - 2.89 eV, $\langle 110 \rangle$ - 5.04 eV and 23.28 eV in Y direction, $\langle 111 \rangle$ - 0.43 eV. For axes $\langle 100 \rangle$ and $\langle 111 \rangle$ barriers in any direction are the same, for $\langle 110 \rangle$ barriers are very different for different directions and much bigger than for other axes. This leads to better channeling in $\langle 110 \rangle$ axis and better channeling in the case of bent crystals for bending in Y direction.

Chapter 5

Channeling in bent and periodically bent crystals

In this chapter the channeling in bent crystalline systems is studied. In the Section 5.1 a simulation of channeling in a uniformly bent crystal is described for the wide range of energies of electrons and positrons. These results were previously published paper [47]. The results of these simulations were compared with the results of recent experiment, which was performed at the SLAC (Stanford Linear Accelerator Center) research facility. In the Section 5.1.3 the simulation model is validated by the comparison of simulation results for two interaction potentials. The comparison shows the stability of the simulation results with respect to the interaction potential selection. The Section 5.1.4 describes the influence of the parameters of the beam and medium on the simulation results. The Section 5.2 describes the channeling in periodically bent crystals. These results were previously published paper [46]. In the Section 5.3 the numerical comparison of channeling in bent axial and planar channels is performed. The Section 5.5 describes the special case of channeling in periodically bent crystals with small amplitude and small period of bending. It is shown that this type of bending can be used to emit photons of very high energy. These results were previously described in the paper [63] which is in the process of publication.

5.1 Channeling in bent crystals

Using the algorithm outlined in Chapter 3, classical trajectories were simulated for $\varepsilon = 3 \dots 20$ GeV electrons and positrons incident along the (111) crystallographic plane in a bent silicon crystal. The crystal thickness $L = 60 \mu\text{m}$ and bending radius $R = 15 \text{ cm}$ were chosen in accordance with the values quoted in [11]. These correspond to the bending angle $L/R = 400 \mu\text{rad}$.

For each set of energy and projectile type the number $N_0 \approx 10000$ of trajectories was simulated with random sampling of initial parameters of a projectile.

In the course of propagation through a crystal, the projectile can experience the re-channeling process which is opposite to the dechanneling one. In this case, the transverse energy of an over-barrier particle is decreased in due to collisions, so that it becomes captured into the channeling mode somewhere inside the crystal. It can be noted that rechanneling efficiency is much higher for negatively charged projectiles than for positively charged ones of the same energy [119]. With rechanneling taken into account, the number of particles staying in the channeling mode $N_{\text{ch}}(z)$ exceeds $N_{\text{ch0}}(z)$. The excess is more pronounced (up to several times and even more in some cases) for straight crystals at penetration distances $z \gtrsim L_{\text{p1}}$ due to a non-exponential decay rate of $N_{\text{ch}}(z)$ [119]. For the crystals with bending radius $R \sim (10 \dots 100)R_c$ (where R_c is Tsyganov's critical radius [124]) it gradually reduces to the tens per cent level and virtually vanishes for smaller values of R [45, 53]. This is illustrated in Figure 5.1 where the fractions $N_{\text{ch0}}/N_{\text{acc}}$ and $N_{\text{ch}}/N_{\text{acc}}$ are plotted versus z for $\varepsilon = 3.35$ (left) and 6.3 (right) GeV electron channeling in straight and bent ($R = 15 \text{ cm}$) Si(111). Note the non-monotonous dependence of $N_{\text{ch}}/N_{\text{acc}}$ at small penetration length which is due to the rechanneling effect occurring in the vicinity of the entrance. For the straight crystal the excess is quite large for both energies, whereas the bent crystal it becomes less pronounced and decreases with increase of ε in accordance with the statement made above. Indeed, estimating the critical radius as $\varepsilon/U'_{\text{max}}$ and using the value $U'_{\text{max}} = 5.7 \text{ GeV/cm}$ for the maximal gradient of the continuous interplanar potential for Si(111) [117], one derives $R/R_c \approx 25$ for $\varepsilon = 3.35 \text{ GeV}$ and ≈ 14 for 6.3 GeV electrons.

The calculated values of acceptance and penetration distance L_{p1} , as well as the estimates for L_{d} (for electron channeling, only) are summarized in Table 5.1. The indicated statistical uncertainties are due to the finite number N_0 of the analyzed trajectories and correspond to the confidence probability $\alpha = 0.999$.

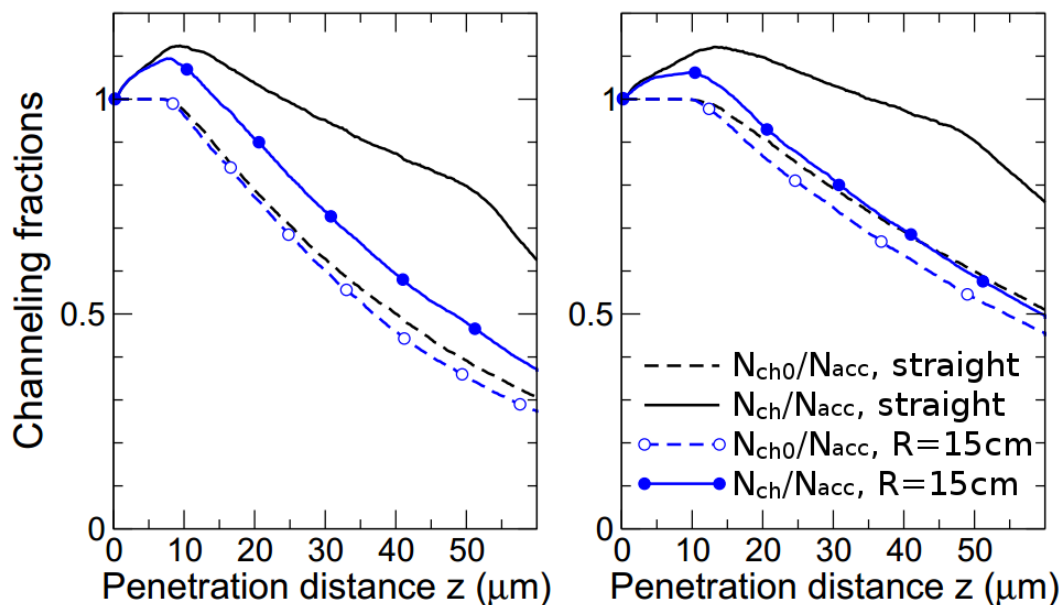


Figure 5.1: Channeling fractions vs penetration distances calculated for 3.35 GeV (left) and 6.3 GeV (right) electrons channeling in straight and bent Si(111) channel. Figure adapted from [47].

On total, the \mathcal{A} and L_{p1} values for positrons are higher than for electrons of the same energy. This is not at all surprising and is due to the well-known difference in the channeling motion of negatively and positively charged particles. The latter tend to channel in between two planes, i.e. in the domain with low content of crystal electrons and nuclei, whereas the former channel in the vicinity of a plane where the content of the constituents is order of magnitude higher. As a result, the electrons dechannel faster than positrons. It is seen for positrons $L_{p1} \approx L = 60 \mu\text{m}$, i.e. nearly all captured positrons channel through the whole crystal. Thus, the thickness is too small to provide an estimate for the dechanneling length. For electrons, the presented values of L_d correspond to the lower boundary for the dechanneling length since the exponential decay law can be expected to be valid at the distances $z \gtrsim L_d$. Also, to be noted, the decrease of acceptance with the energy growth which is due to the increase of the centrifugal force ε/R in a bent crystal.

Direct measurement of the dependencies $N_{ch0}(z)$ and $N_{ch}(z)$ is hardly possible. However, they can be deduced as well as the quantities \mathcal{A} and L_d can be estimated if one measures (or calculate) the angular distribution of the particles leaving the crystal. Figure 5.2 presents the calculated distributions of electrons (top graph) and positron (bottom graph) of different energies with respect to the deflection angle,

| ε | electron | | | positron | |
|---------------|---------------|----------------|----------------|---------------|----------------|
| | \mathcal{A} | L_{p1} | L_d | \mathcal{A} | L_{p1} |
| 3 | 62 | 39.5 ± 0.7 | 37.8 ± 2.3 | 0.89 | 56.7 ± 0.5 |
| 4 | 60 | 43.1 ± 0.9 | 45.9 ± 3.8 | 0.87 | 56.8 ± 0.5 |
| 5 | 58 | 45.4 ± 0.8 | 51.7 ± 4.6 | 0.87 | 57.1 ± 0.5 |
| 6 | 55 | 47.5 ± 0.8 | 57.3 ± 5.3 | 0.86 | 57.6 ± 0.4 |
| 7 | 55 | 48.3 ± 0.8 | 58.6 ± 5.5 | 0.84 | 57.8 ± 0.4 |
| 8 | 54 | 49.2 ± 0.8 | 63.3 ± 6.2 | 0.84 | 58.0 ± 0.4 |
| 9 | 52 | 54.4 ± 0.8 | 69.7 ± 7.5 | 0.82 | 58.1 ± 0.3 |
| 10 | 50 | 50.9 ± 0.8 | 73.4 ± 8.3 | 0.80 | 58.2 ± 0.4 |
| 20 | 39 | 51.4 ± 0.9 | 62.8 ± 7.3 | 0.58 | 59.7 ± 0.2 |

Table 5.1: Acceptance \mathcal{A} (in %), penetration L_{p1} and dechanneling L_d lengths (in μm) for electrons and positrons of different energies ε (in GeV). Statistical errors for \mathcal{A} are 0.02 in all cases.

i.e. the angle between the projectile velocities at the crystal entrance and exit. The vertical dashed lines mark the initial beam direction (zero angle) and the crystal bending angle. The maxima of the distributions are located in the vicinity of this direction. The first maximum is due to the particles which, being not captured at the entrance passed through the whole crystal in the non-channeling mode. Its position is displaced from the initial direction by the interval equal to the Lindhard critical angle Θ_L [1]. The width of the maximum is determined by the larger of the two angles: Θ_L and beam emittance. The distributions presented correspond to the zero beam emittance. The second maximum is formed by projectiles which leave the crystal moving in the channeling mode. It is positioned at exactly $400 \mu\text{rad}$ and has the width equal to Θ_L . The distribution between the maxima corresponds to the particles which stayed in the channeling mode (including the segments due to the rechanneling events) throughout part of the crystal. Comparing two graphs in Figure 5.2 one notices that the second maximum is much more powerful for positrons since most of them, being captured at the entrance channel through the whole crystal. The first maximum is also more pronounced for positrons reflecting the higher values of the acceptance.

Each curve in Figure 5.2 is normalized to the unit area. Approximating the maxima with the Gaussian distributions and the curve in between them by the exponent $\propto \exp(-ax)$, one can calculate the acceptance (subtracting the area under the first maximum from one), the *channeling efficiency* (the area under the second maximum), and estimate the dechanneling length as $= 1/a$. This methodology of

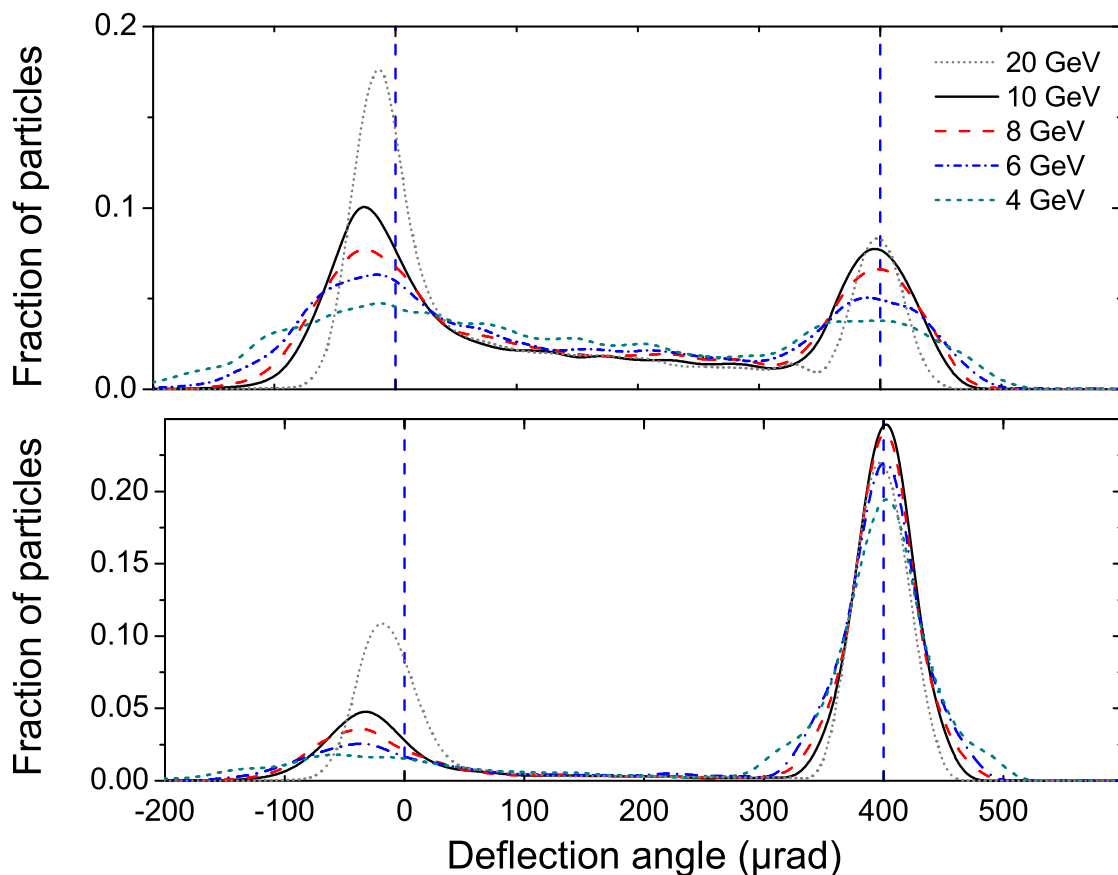


Figure 5.2: Angular distribution of electrons (top) and positrons (bottom) of several energies (as indicated in the top graph) at the exit from bent oriented Si(111) crystal. The crystal thickness is $L = 60\mu\text{m}$, the bending radius $R = 15\text{ cm}$. Vertical lines correspond to the incident beam direction ($0\ \mu\text{rad}$) and the bending angle $L/R = 400\ \mu\text{rad}$. Figure adapted from [47].

estimating L_d has been widely exploited recently for various ultra-relativistic projectiles in straight and bent crystals [87, 125, 11]. It can be noted that, intrinsically, this scheme has two drawbacks which influence the estimated value of L_d . First, the rechanneling effect is neglected, and, second, the exponential decay law is assumed to be valid for all penetration distances, whereas at $z \lesssim L_d$ it must be supplemented with additional terms [117, 126].

5.1.1 Comparison with experimental results

Comparison of the calculated results with the experimental data [11, 127] is shown in Table 5.2 and Figs. 5.3, 5.4.

| ε (GeV) | Method | \mathcal{A} (%) | L_d (μm) | Efficiency (%) |
|---------------------|-----------------|-------------------|-------------------------|----------------|
| 3.35 | this work | 62 ± 2 | 39 ± 2 | 22 ± 1 |
| | exp. [11] | 64 ± 2 | 43 ± 6 | 22 ± 1 |
| | calc. [11, 40] | – | 37 | 23 |
| | calc. [127, 40] | 67 | 42 | 21 |
| 6.3 | this work | 55 ± 2 | 54 ± 6 | 26 ± 2 |
| | exp. [11] | 57 ± 2 | $33 + 5 - 2$ | 22 ± 1 |
| | calc. [11, 40] | – | 42 | 23 |
| | calc. [127, 40] | 51 | 31 | 20 |

Table 5.2: Comparison of acceptance \mathcal{A} , dechanneling length and channeling efficiency for electrons with the results of experimental measurements [11, 127] and simulations with DYNECHARM++ [40]. The term acceptance corresponds to the term "surface transmission" used in [11].

In Table 5.2 the acceptance, channeling efficiency and the dechanneling lengths for 3.35 and 6.3 GeV electrons are compared. The experimental data as well as the data calculated by means of the DYNECHARM++ code [40] are taken from Table I in Ref. [11], and Table I in Ref. [127]. The overall agreement for the lower electron energy can be stated. For 6.3 GeV electrons the results do agree with experiment on the acceptance but slightly (on the level of 10...15 per cent) overestimate the channeling efficiency. A larger discrepancy is seen in the L_d values. The simulated lower value of the dechanneling, 48 μm is 1.25 times larger than the experimentally measured upper boundary of 38 μm . It can be noted, though, that simulations performed with the code [11, 40] result in the L_d value also exceeding the experimental one.

In Figure 5.3 the simulated and experimentally detected angular distributions for 6.3 GeV and 3.35 GeV electrons are compared. The solid curve represents the dependence obtained by means of the simulation procedure for the bending radius $R = 15$ cm in accordance with the value quoted in [11]. However, it is clearly seen that the second maximum in the experimental distribution (red broken curve) is shifted from the expected position of 400 μrad towards larger values. This may indicate that the bending radius of the crystalline sample used in the experiment was slightly less than as quoted.¹ To check this, the distribution for a smaller radius, $R = 14$ cm was calculated. This distribution is drawn in the figure with blue chained line. The positions of both of its maxima coincide with those of the experimental curve.

¹In fact, the value of 60 ± 1 μm for the crystal thickness, and 402 ± 9 μrad for the bending angle indicated in [11] correspond to the bending radius 14.9 ± 0.4 cm.

Comparing other features it can be stated that the simulation overestimates slightly the channeling efficiency (the area under the second maximum) and underestimates the number of non-accepted particles (the area under the first maximum).

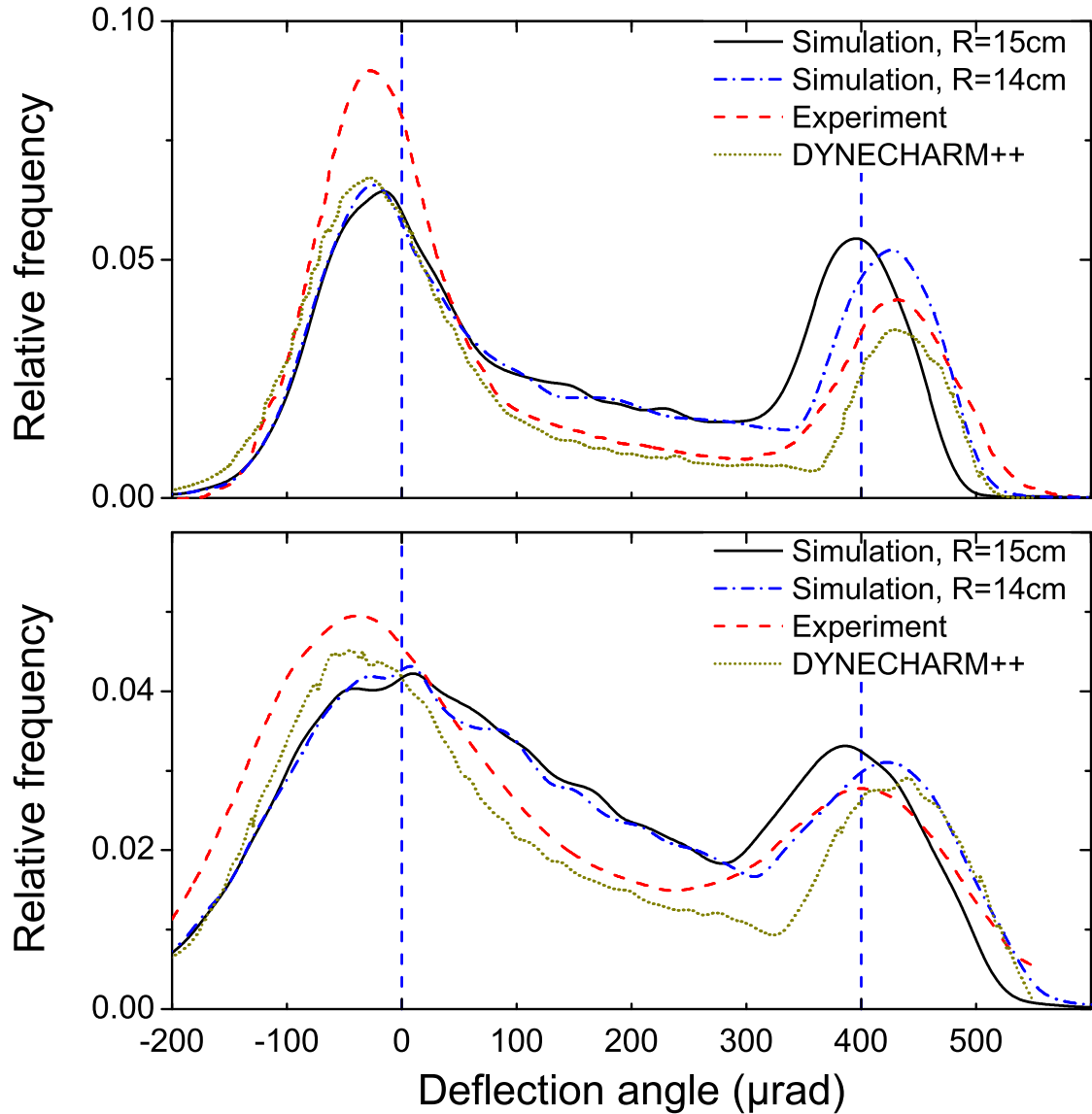


Figure 5.3: Angular distribution of 6.3 GeV (top) and 3.35 GeV (bottom) electrons in bent Si(111) planar channel. Broken (red) curve represents the experimental data [11], dot (olive) line represent simulation results with DYNECHARM++ [127, 40], solid (black) and chained (blue) curves correspond to the simulations carried out for two indicated values of the bending radius R . Vertical lines correspond to the incident beam direction ($0 \mu\text{rad}$) and the bending angle $400 \mu\text{rad}$ for $R = 15 \text{ cm}$. Figure adapted from [47].

Dechanneling length as a function of electron energy is presented by Figure 5.4. The experimental data (squares) [11, 127] and the results of current simulations (filled circles) correspond to the bent Si(111) crystal. As mentioned, the correspondence is seen for the lower energy. The simulated data show steady increase of L_d with ε which is, although, slower than in the straight crystal. The latter case, represented by diamonds, shows virtually a linear dependence (illustrated by the straight line) and, thus, is in accordance with prediction of the diffusion theory of electron dechanneling [78] which is expected to be valid in the multi-GeV energy range. Open circles correspond to the model estimation of the dechanneling length in the straight crystal. These data are obtained by the division of the simulated L_d values for bent Si(111) by the factor $(1 - R/R_c)^2$. The validity of this model, utilized in [11], can be proven for positively charged particles channeling in the harmonic interplanar potential [117] but is less obvious for negatively charged projectiles. However, in the latter case its applicability was demonstrated for electrons within the framework of the continuous potential model [30, 128]. Comparing the data marked in Figure 5.4 by the open circles with the diamonds one concludes that the model can be used for quantitative estimations.

Nearly linear form of the dependence of dechanneling length on beam energy is also in agreement with theoretical estimation, and indicates self-consistency of the results.

5.1.2 Radiation spectrum

The simulated trajectories were used to compute spectral distribution of the radiation emitted within the cone $\theta < \theta_{\max}$ with respect to the incident beam using quasi-classical method [78] described in Section 2.2. This approach explicitly takes into account the quantum corrections due to the radiative recoil, i.e. the change in the projectile energy due to the photon emission, which can be quantified by the ratio $\hbar\omega/\varepsilon$. The limit $\hbar\omega/\varepsilon \ll 1$ corresponds to the classical description of the radiative process. As a rule, the classical framework is adequate to describe the emission spectra by electrons and positrons of the sub-GeV energy range (see, for example, [53] and references therein). The quantum corrections must be accounted for if $\hbar\omega/\varepsilon \lesssim 1$. In recent paper [34] it was demonstrated, that the corrections lead to strong modifications of the radiation spectra of multi-GeV electrons and positrons channeling in small-amplitude short-period crystalline undulators.

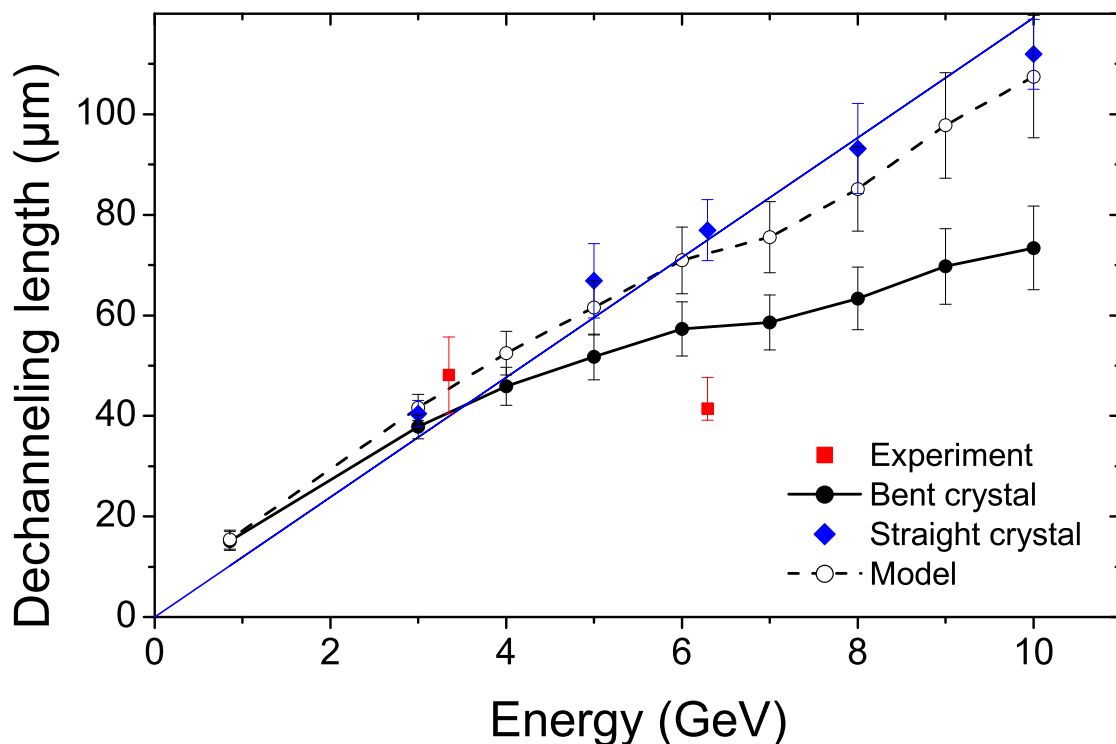


Figure 5.4: Dechanneling length in 60 μm Si(111) crystals with bending radius $R = 15$ cm versus the energy of electron beam. The experimental data (squares) [11] are compared with the results of current simulation (filled circles and diamonds). Open circles and straight line stand for the model calculations, see explanations in the text. Figure adapted from [47].

The emission spectra calculated for several energies of projectiles and in a broad range of the photon energies are presented in Figs. 5.5 (positrons) and 5.6 (electrons). The spectra correspond to the emission cone $\theta_{\text{max}} = 1.2$ mrad. For all specified energies, this cone is order of magnitude larger than the natural emission angle $\sim 1/\gamma$ and three times larger the bending angle of the crystal. Therefore, the dependencies presented correspond to virtually all emitted radiation.

Several features in the spectra can be noted. First, the planar direction (111) contains two types of channels, which results in a broad radiation spectrum with several maximal values [46]. In case of positrons oscillations in these types of channels lead to distinguishable features in radiation spectrum. For electrons channeling oscillations are anharmonic and, therefore, the channeling radiation peaks are broadened and merged in a single distribution. Second, crystal bending leads to the increase of the yield of low-energy photons due to the synchrotron radiation. This effect, seen

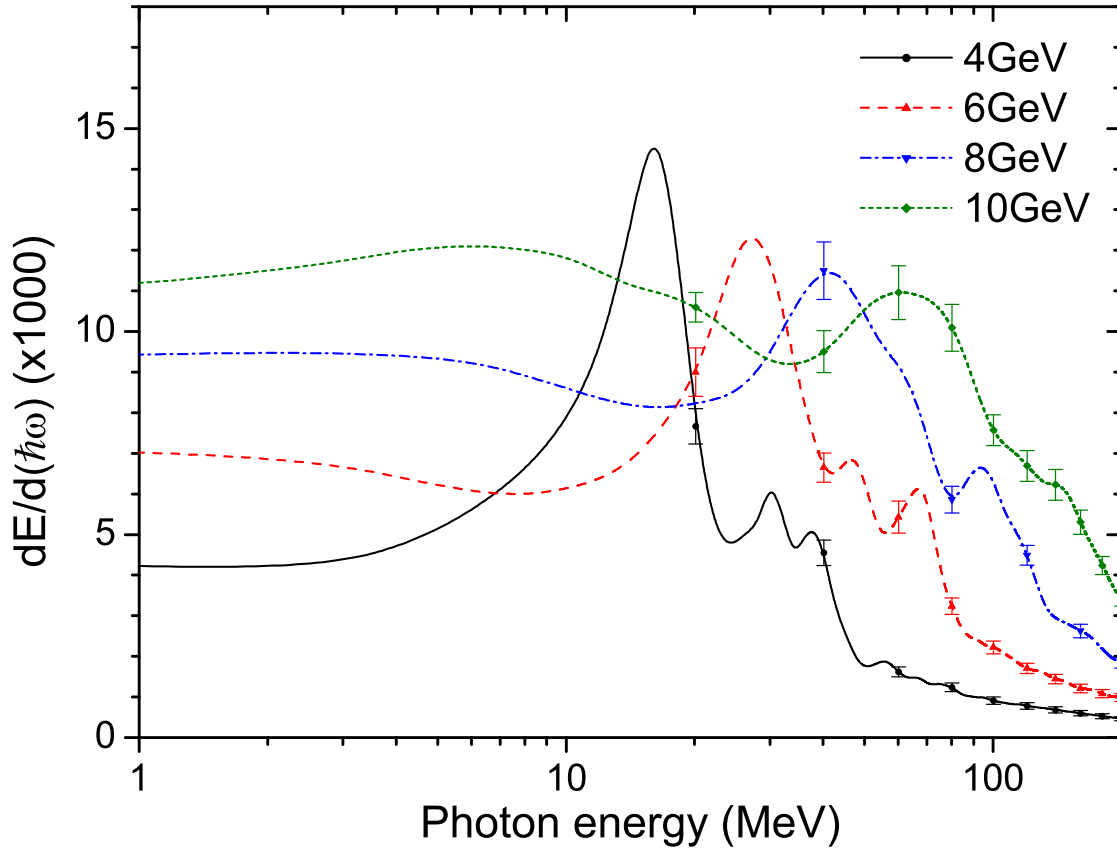


Figure 5.5: Radiation spectra of 4...10 GeV positrons in bent Si(111) crystal. Figure adapted from [47].

explicitly in Figure 5.5, becomes more pronounced with increase of the beam energy, as it follows from the general theory of synchrotron radiation. The third feature, illustrated by Figure 5.6, is in lowering the peak of channeling radiation in a bent crystal (compare the solid and broken lines). This is mainly due to the decrease in the channeling length due to the crystal bending. For the sake of comparison, the spectrum of incoherent bremsstrahlung in amorphous silicon is also presented in the figure.

5.1.3 Comparison of results for Molière and Pacios potential

In order to verify the use of the Molière potential for the simulations another type of the potential was taken for comparison: the Pacios potential of interaction of electrons with atoms of the medium. The form of this potential and its parameters are described in Section 3.3.2. In Figure 5.7 the comparison of interaction potential

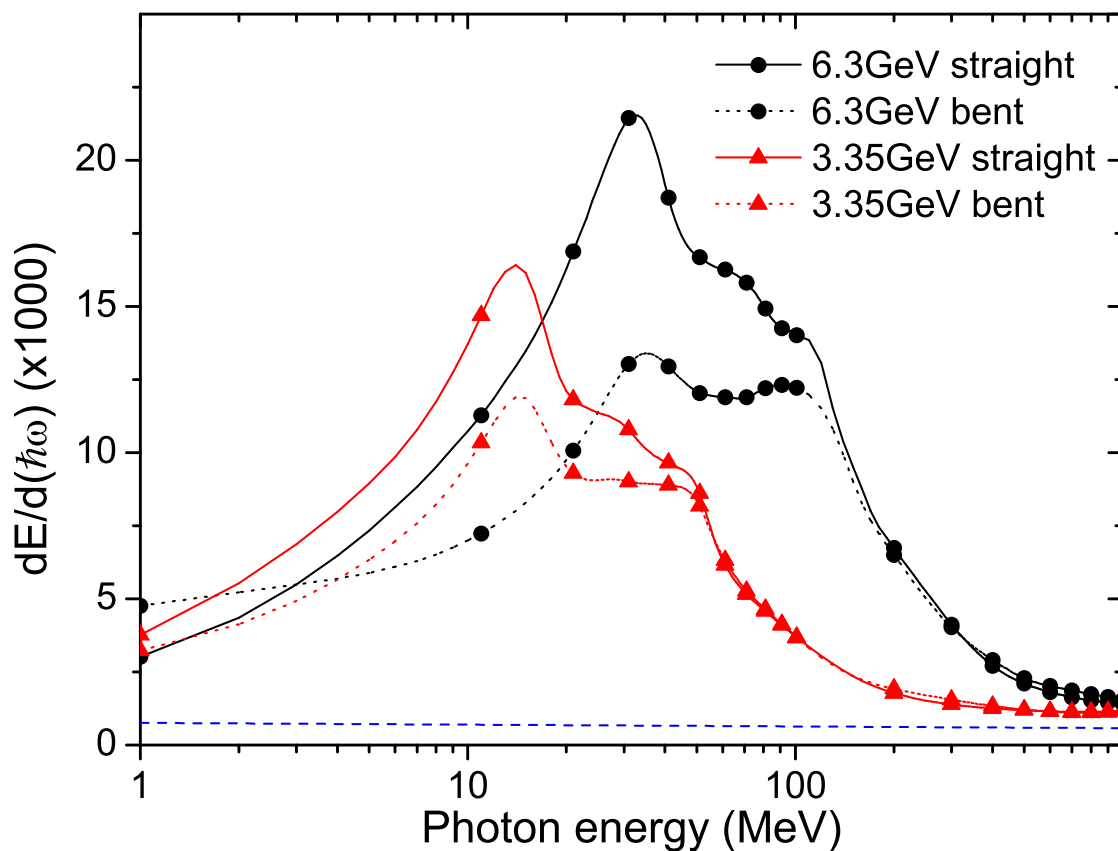


Figure 5.6: Radiation spectra by 3.35 and 6.3 GeV electrons in bent and straight Si(111). Broken line stands for the emission spectrum in amorphous silicon by the 3.35 GeV projectile calculated within the Bethe-Heitler approximation. Figure adapted from [47].

of a positron with Si atom is shown for Molière, Pacios and Coulomb potentials. Molière and Pacios approximations give similar values of the potential for the distances below 1 Å, but are different for higher distances. Therefore the difference between the results is more likely to be observed for positrons than for electrons as they move far from planes of atoms.

In Table 5.3 the comparison of channeling characteristics of 3.35, 6.3 and 10 GeV electrons in straight and bent ($R=15\text{cm}$) Si(111) channels simulated using same method but with Molière and Pacios potentials is provided. The results of the simulations are same within the statistical errors.

For positrons the situation is similar. In Table 5.4 the comparison of channeling characteristics of 10 GeV positrons in straight and bent ($R=15\text{ cm}$) Si(111) channels is shown. The difference in this case is also on the level of statistical error for both

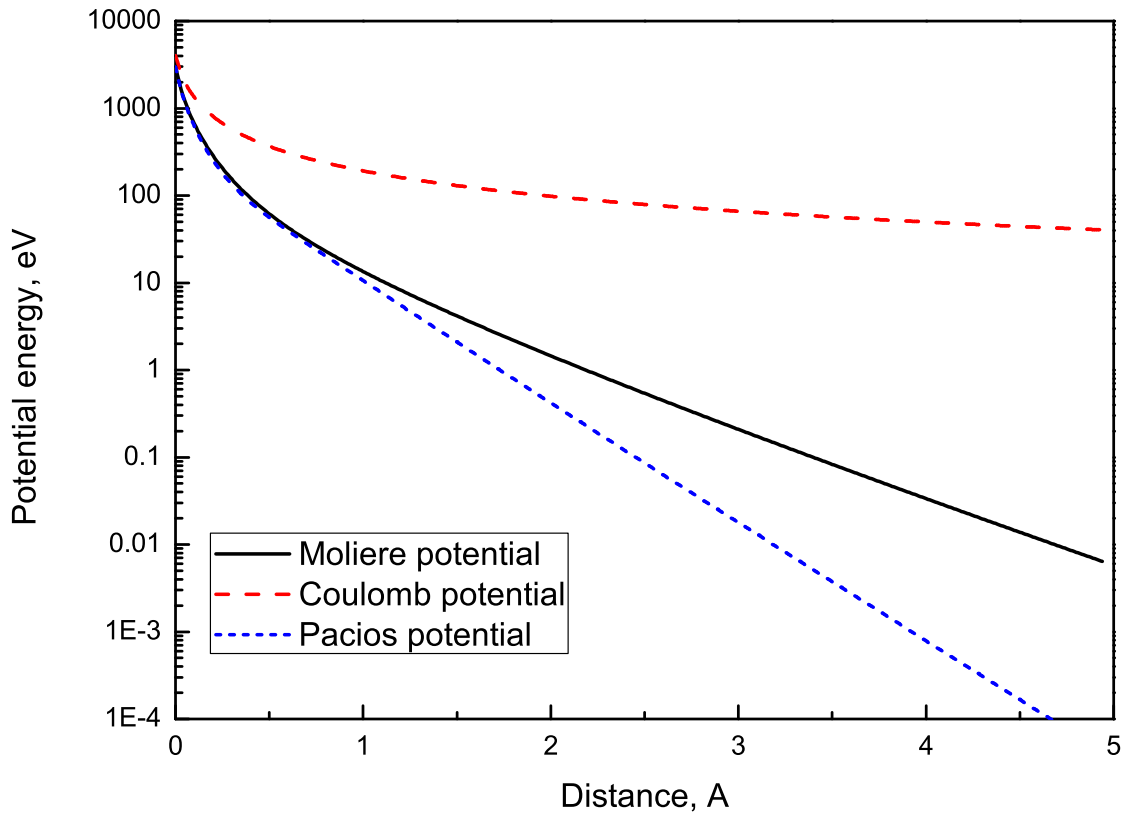


Figure 5.7: Comparison of Pacios and Molière potential with Coulomb potential for the description of interaction of a positron with Si atom. The behavior of both potentials is same for distances below 1 Å, for larger distances the Pacios potential decreases faster.

straight and bent crystals.

In order to check the influence of the interaction potential on a photon emission spectrum consider results of simulation of 6.7 GeV electrons and positrons in straight Si(110) crystal. In Figure 5.8 the comparison of simulated photon emission spectrum of 6.7 GeV electrons in straight Si(110) crystal with experimental results [8] for the cases of Molière and Pacios interaction potentials is given. It is shown, that the results of simulations with Pacios potential show slightly different result (up to 5-10% lower intensity). Within the statistical errors both results are in a good agreement with the experimental measurements.

The similar comparison for positrons is provided in Figure 5.9. The results of the comparison show, that the difference between simulation with Molière and Pacios interaction potentials influences less on positrons, than on electrons. The reason for this is that electrons are propagating closer to atomic planes and experience

| ε (GeV) | Pot. | \mathcal{A} (%) | L_{p1} (μm) | L_{p2} (μm) | L_d (μm) |
|---------------------|---------|-------------------|----------------------------|----------------------------|-------------------------|
| 3.35 | Pacios | 66.0 ± 2.9 | 43.3 ± 1.3 | 40.6 ± 1.1 | 42.5 ± 1.5 |
| | Molière | 61.4 ± 1.4 | 41.4 ± 0.7 | 38.9 ± 0.6 | 41.9 ± 0.8 |
| 3.35 bent | Pacios | 60.1 ± 3.0 | 40.0 ± 1.4 | 39.3 ± 1.3 | 37.2 ± 1.4 |
| | Molière | 61.8 ± 1.4 | 41.3 ± 0.7 | 40.6 ± 0.6 | 39.2 ± 0.7 |
| 6.3 | Pacios | 68.4 ± 1.9 | 52.3 ± 0.7 | 50.3 ± 0.7 | 73.4 ± 6.7 |
| | Molière | 70.4 ± 1.6 | 52.4 ± 0.6 | 50.2 ± 0.6 | 76.9 ± 6.1 |
| 6.3 bent | Pacios | 55.0 ± 2.1 | 48.2 ± 0.9 | 48.0 ± 0.9 | 55.2 ± 5.3 |
| | Molière | 56.2 ± 2.7 | 48.8 ± 1.1 | 48.6 ± 1.2 | 53.7 ± 6.4 |
| 10.0 | Pacios | 72.8 ± 2.7 | 56.6 ± 0.8 | 55.5 ± 0.8 | 108.9 ± 16.8 |
| | Molière | 70.8 ± 1.0 | 56.8 ± 0.3 | 55.5 ± 0.3 | 111.9 ± 6.9 |
| 10.0 bent | Pacios | 49.1 ± 3.0 | 51.4 ± 1.3 | 51.3 ± 1.3 | 62.8 ± 9.7 |
| | Molière | 50.4 ± 1.9 | 50.9 ± 0.8 | 50.8 ± 0.8 | 73.4 ± 8.3 |

Table 5.3: Comparison of channeling characteristics of 3.35, 6.3 and 10 GeV electrons in straight and bent (R=15 cm) Si(111) channels simulated using same method but with Molière and Pacios potentials.

| ε (GeV) | Pot. | \mathcal{A} (%) | L_{p1} (μm) | L_{p2} (μm) |
|---------------------|---------|-------------------|----------------------------|----------------------------|
| 10.0 | Pacios | 70.8 ± 1.7 | 60.9 ± 0.3 | 58.0 ± 0.6 |
| | Molière | 70.8 ± 1.8 | 61.0 ± 0.3 | 58.6 ± 0.6 |
| 10.0 bent | Pacios | 66.9 ± 3.6 | 60.8 ± 0.7 | 59.9 ± 0.9 |
| | Molière | 65.7 ± 3.5 | 60.8 ± 0.7 | 60.2 ± 0.8 |

Table 5.4: Comparison of channeling characteristics of 10 GeV positrons in straight and bent (R=15 cm) Si(111) channels simulated using same method but with Molière and Pacios potentials.

higher interaction forces. Within the statistical error the difference in the simulated radiation spectrum is negligible, and is much lower, than the influence of the incident beam parameters.

5.1.4 Influence of incident angle and temperature on channeling

The process of channeling depends on parameters of the beam and properties of the crystalline medium. In order to take into account angular beam emittance the random rotation of initial velocity was added to the model. This rotation of the velocity vector is done in both X and Y direction. The distribution of rotation angles in these two directions is uniform in the range of $[-\psi, \psi]$, where ψ is the

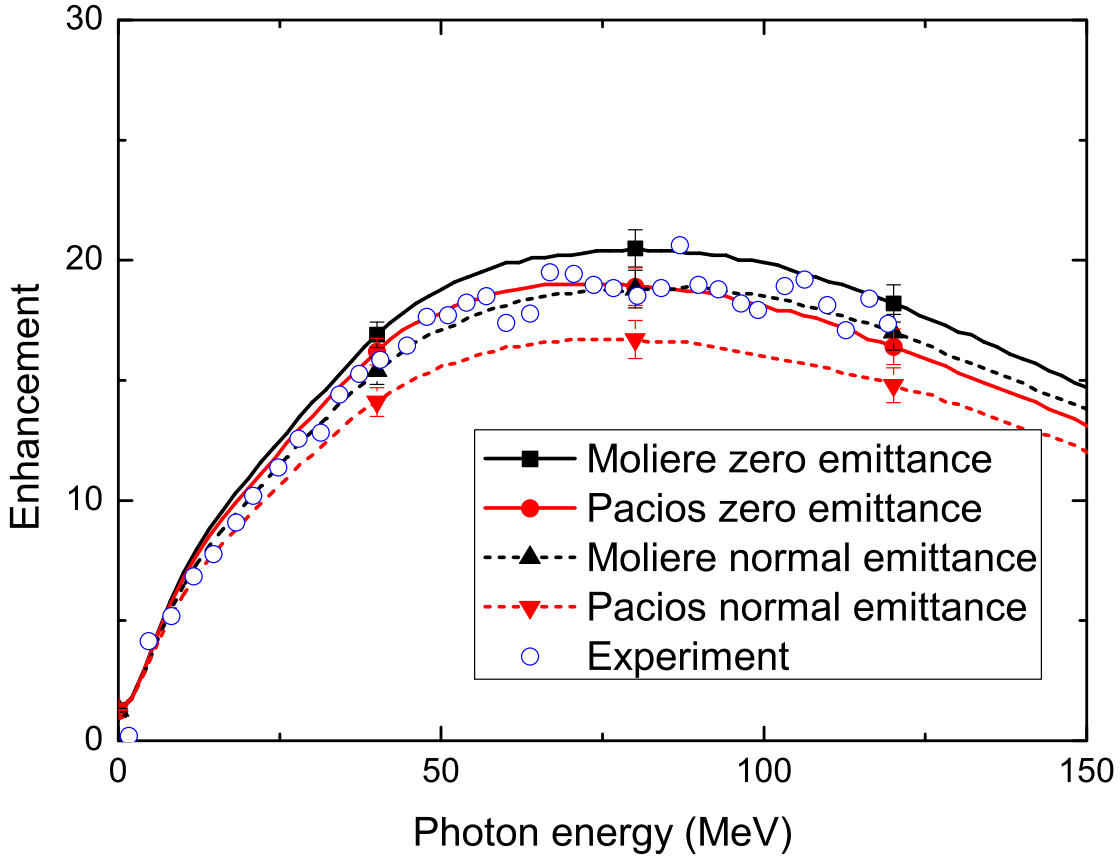


Figure 5.8: Comparison of simulated photon emission spectrum of 6.7 GeV electrons in straight Si(110) crystal with experimental results [8] for the cases of Molière and Pacios interaction potentials. The results for zero emittance of the beam are shown with solid lines, the results for beam emittance of $\psi_L = 62 \mu\text{rad}$ are shown with dashed lines.

emittance angle. In Figure 5.10 the angular beam emittance is illustrated.

In experiments the value of the angular beam emittance is known and is one of the important characteristics of the beam. In the paper [127] the characteristic value of beam emittance is $10 \mu\text{rad}$, the estimation of a critical angle for a 6.3 GeV electrons is given $\theta_{crit} = 80 \mu\text{rad}$. In Table 5.5 the comparison of simulated channeling characteristics of 6.3 GeV electrons in bent ($R=15\text{cm}$) Si(111) channels simulated with different values of angular emittance is shown.

The results of the simulations show, that within statistical errors the value of dechanneling length does not depend on angular emittance of beam. The value of acceptance \mathcal{A} on the other hand does depend on angular emittance. For the values of angle closer the critical angle the ratio of initially accepted particles drops

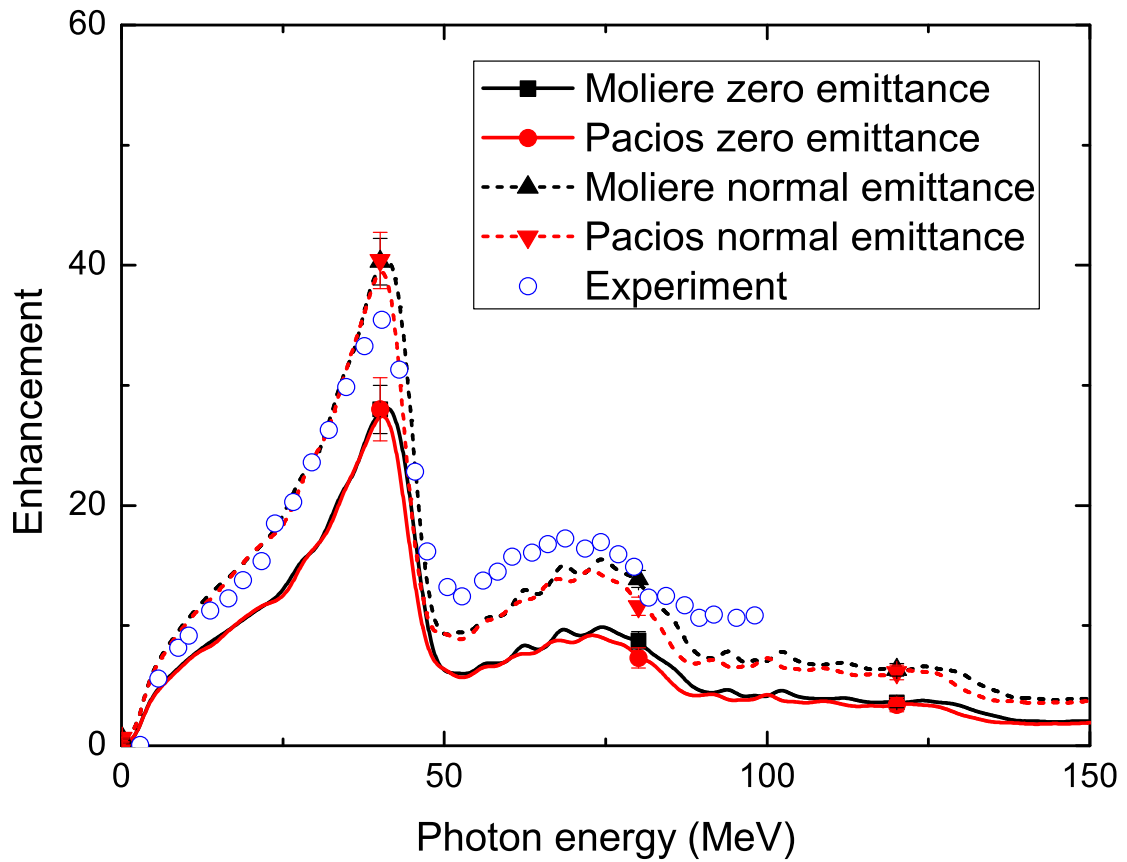


Figure 5.9: Comparison of simulated photon emission spectrum of 6.7 GeV positrons in a straight Si(110) crystal with experimental results [8] for the cases of Molière and Pacios interaction potentials. The results for zero emittance of the beam are shown with solid lines, the results for beam emittance of $\psi_L = 62 \mu\text{rad}$ are shown with dashed lines.

significantly.

Another important characteristic of a channeling process is the temperature of thermal vibrations of atoms of a medium [129]. In the book [2] the reference values of thermal vibrations of atoms in different crystalline media are given. For Si the amplitude of thermal vibration at room temperature is 0.075 \AA . In Table 5.6 the comparison of channeling characteristics of 6.3 GeV electrons in bent ($R=15\text{cm}$) Si(111) channels simulated with different amplitudes of thermal vibrations is shown.

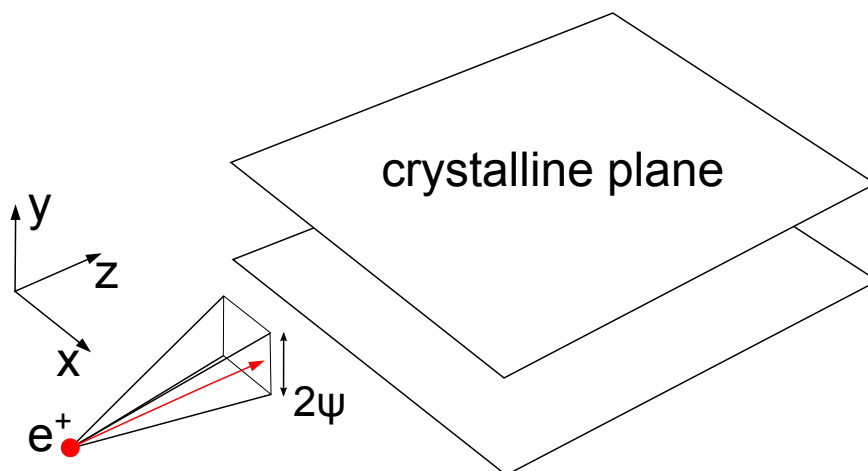


Figure 5.10: Angular beam emittance is simulated using random rotation of initial velocity in two directions. The distribution of rotation angles in these two directions is uniform.

| Angle (μrad) | \mathcal{A} (%) | L_{p1} (μm) | L_{p2} (μm) | L_d (μm) |
|---------------------------|-------------------|----------------------------|----------------------------|-------------------------|
| 0 | 56.2 ± 2.8 | 48.8 ± 1.2 | 48.6 ± 1.2 | 56.4 ± 2.2 |
| 5 | 57.4 ± 1.7 | 48.1 ± 0.8 | 47.9 ± 0.8 | 57.9 ± 1.5 |
| 10 | 57.0 ± 1.6 | 47.8 ± 0.7 | 47.6 ± 0.7 | 59.1 ± 1.4 |
| 20 | 55.7 ± 2.4 | 47.8 ± 1.1 | 47.7 ± 1.1 | 56.8 ± 2.0 |
| 30 | 54.3 ± 2.9 | 48.4 ± 1.3 | 48.2 ± 1.3 | 60.5 ± 2.7 |
| 50 | 50.6 ± 1.8 | 47.6 ± 0.9 | 47.5 ± 0.8 | 57.7 ± 1.7 |
| 100 | 30.0 ± 2.4 | 48.1 ± 1.5 | 47.7 ± 1.4 | 53.0 ± 2.9 |

Table 5.5: Comparison of channeling characteristics of 6.3 GeV electrons in bent ($R=15$ cm) Si(111) channels simulated with different values of angular emittance.

5.2 Channeling in periodically bent crystals

In this section the results of simulation of the channeling in periodically bent crystals with different parameters are given and compared with the case of straight crystal. In the first subsection the results of simulations of sub-GeV energies projectiles are given. In the second subsection the results for multi-GeV beams are described.

5.2.1 Results for sub-GeV electrons and positrons

In this section the results obtained recently [46] with the use of the MBN Explorer code [44] for the channeling phenomenon and radiation emitted in a crystalline

| Amplitude (Å) | \mathcal{A} (%) | L_{p1} (μm) | L_{p2} (μm) | L_d (μm) |
|---------------|-------------------|----------------------------|----------------------------|-------------------------|
| 0 | 67.2 ± 2.8 | 51.3 ± 1.2 | 50.8 ± 1.2 | 94.2 ± 5.2 |
| 0.0375 | 61.3 ± 3.8 | 46.5 ± 1.7 | 46.4 ± 1.7 | 50.0 ± 2.5 |
| 0.075 | 56.2 ± 2.8 | 48.8 ± 1.2 | 48.6 ± 1.2 | 56.4 ± 2.2 |
| 0.105 | 54.5 ± 3.2 | 49.2 ± 1.4 | 49.0 ± 1.4 | 60.5 ± 3.0 |
| 0.15 | 55.6 ± 2.8 | 50.1 ± 1.2 | 49.9 ± 1.1 | 61.1 ± 2.6 |

Table 5.6: Comparison of channeling characteristics of 6.3 GeV electrons in bent (R=15 cm) Si(111) channels simulated with different amplitudes of thermal vibrations.

undulator (CU) are presented. In CU, in addition to the channeling radiation, the undulator-type radiation appears due to the undulating motion of channeling particles which follow the periodic bending of crystallographic planes [19, 20, 32]. Two types of harmonic periodic bending of the channel centerline, which correspond to the sine and to the cosine profiles, can be considered:

$$y(z) = a \sin(2\pi z/\lambda_u) \quad y(z) = a \cos(2\pi z/\lambda_u) \quad (5.1)$$

Here, the z -coordinate is measured along the straight channel and the y -axis is perpendicular to the straight plane. The quantities a and λ_u are the bending amplitude and period and they satisfy the relation $d < a \ll \lambda_u$ where d is the interplanar distance (see the cited papers for more details on the description of the CU concept).

We have performed simulation of the trajectories, the quantitative analysis of the channeling motion and computation of the spectral intensities of the radiation formed by ultra-relativistic electrons and positrons within the energy range 195...855 MeV in the CU with the parameters used in the experiments at the Mainz Microtron (Germany) facility [54, 130]. The 4-periods CUs were manufactured in Aarhus University (Denmark) using the molecular beam epitaxy technology to produce strained-layer $\text{Si}_{1-x}\text{Ge}_x$ superlattices with varying germanium content as described in [28, 29].

The following values of the CU parameters were used in the calculations:

- * Channeling plane: Si(110) (the interplanar distance $d = 1.92 \text{ \AA}$)
- * Crystal thickness: $L = 39.6 \mu\text{m}$
- * Bending period: $\lambda_u = 9.9 \mu\text{m}$

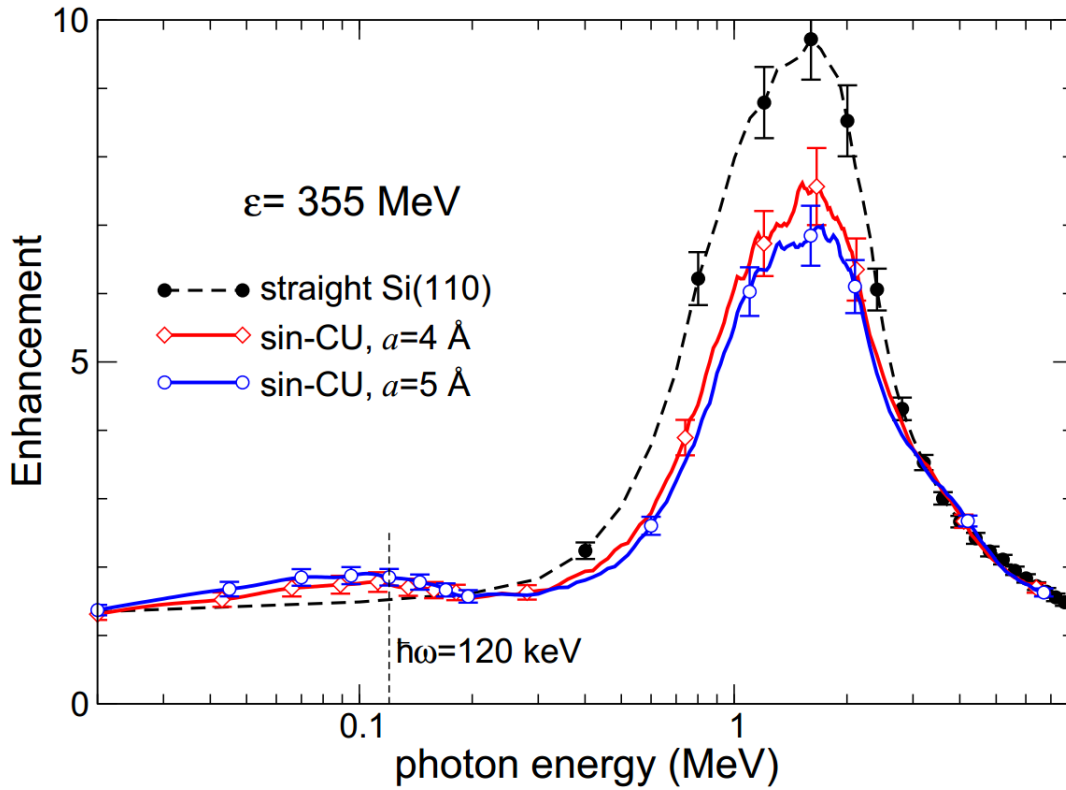


Figure 5.11: Enhancement of radiation emission in straight Si (110) (dashed lines) and in CU (solid lines) over the Bethe-Heitler spectrum. The data refer to $\epsilon = 355$ MeV electrons. Two solid lines present the dependencies for the sine-like CUs of the indicated amplitudes. The maximum emission angle is $\theta_{max} = 0.21$ mrad. Figure adapted from paper [46].

* Bending amplitude: $a = 3...5$ Å

The Figure 5.11 compares the spectral enhancement of radiation emitted by 355 MeV electrons channeled in straight Si(110) and in the sine-shaped CU with two bending amplitudes as indicated. All three dependencies exhibit powerful maximum at about 1.7 MeV which corresponds to the channeling radiation. In the case of the undulating crystals the maxima are lower is due to the decrease in the allowed amplitude of the channeling oscillations in periodically bent channel in comparison with the straight one [118]. However, the CU undulator radiation manifests itself as a hump in the photon energy range 40...100 keV (the vertical dashed line marks the first harmonic of the radiation in the forward direction). Hence, the results of simulations indicate that it is possible to observe the CU radiation even for comparatively low energies of the electron beam.

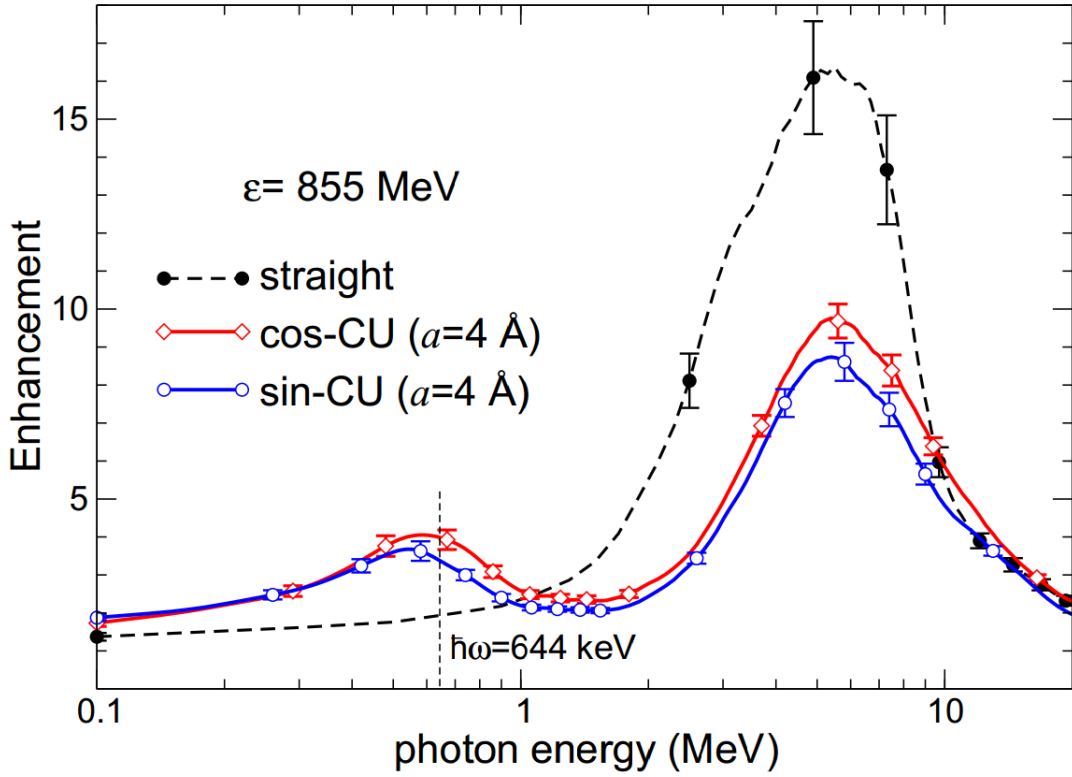


Figure 5.12: Enhancement of radiation emission in straight Si (110) (dashed lines) and in CU (solid lines) over the Bethe-Heitler spectrum. The data refer to $\epsilon = 855$ MeV electrons. Two solid lines stand for the spectra emitted from the sine- and cosine-like CUs of the same amplitude. The maximum emission angle is $\theta_{max} = 0.21 mrad$. Figure adapted from paper [46].

With the increase of the electron beam energy the CU radiation peak becomes more accented, as it is illustrated by Figure 5.12. Here, the maximum at about 600 keV is seen for both sine- and cosine-shaped CUs.

5.2.2 Results for 10 GeV electrons and positrons

In this section the results of simulations of channeling of 10 GeV electrons and positrons in large-amplitude crystalline undulator are provided.

The following values of the CU parameters were used in the calculations:

- * Channeling plane: Si(110) (the interplanar distance $d = 1.92 \text{ \AA}$)
- * Crystal thickness: $L = 320.0 \text{ \mu m}$
- * Bending period: $\lambda_u = 39.6 \text{ \mu m}$

* Bending amplitude: $a = 2...6 \text{ \AA}$

In Table 5.7 the characteristic values of acceptance and channeling segments length estimates are provided. These results show, that most of positrons in this CU stay in the channeling mode from the entrance to the crystal until its end. For electrons both acceptance and channeling segments length is much lower.

| Projectile | a (\AA) | C | \mathcal{A} (%) | L_{p1} (μm) | L_{p2} (μm) |
|------------|----------------------|------|-------------------|----------------------------|----------------------------|
| e^+ | 0 | 0 | 97.1 ± 0.9 | 301.9 ± 3.7 | 271.5 ± 5.5 |
| | 2 | 0.08 | 89.8 ± 2.1 | 300.5 ± 4.9 | 256.2 ± 7.8 |
| | 4 | 0.16 | 81.6 ± 2.6 | 287.1 ± 6.5 | 209.3 ± 8.9 |
| | 6 | 0.24 | 71.9 ± 5.8 | 272.9 ± 15.1 | 169.0 ± 16.76 |
| e^- | 0 | 0.0 | 65.8 ± 2.3 | 81.6 ± 4.1 | 72.6 ± 2.1 |
| | 4 | 0.16 | 42.9 ± 3.3 | 52.1 ± 4.3 | 45.1 ± 2.0 |

Table 5.7: Acceptance and mean channeling length for 10 GeV electrons and positrons in periodically bent planar channels Si(110). The bending parameter C is defined in (2.46).

In Figure 5.13 the comparison of radiation spectrum of 10 GeV electrons and positrons channeling in large-amplitude crystalline undulator is given. The channeling radiation can be observed in both cases in the area of 50-100 MeV. In case of positrons the dechanneling length is much higher and therefore the projectile stays in a channeling mode for several periods of crystal bending. This leads to the creation of a second peak corresponding to undulator radiation. In this figure it can be observed at 10 MeV photons energy.

The growth of undulator amplitude first leads to a decrease of the length of channeling segments results in the decrease of the channeling peak. The channeling peak is observable at the bending amplitude of 2 \AA and is 25% lower than in a straight crystal, but it vanishes completely for higher amplitudes.

In the case of electrons the effect of decrease of dechanneling length and corresponding peak is the same. The effect of undulator radiation is much lower than in the case of positrons due to much lower length of channeling segments.

5.3 Comparison of axial and planar channeling

In order to compare axial channeling with planar channeling a set of simulations were performed. In these simulations channeling in straight and periodically bent crystals

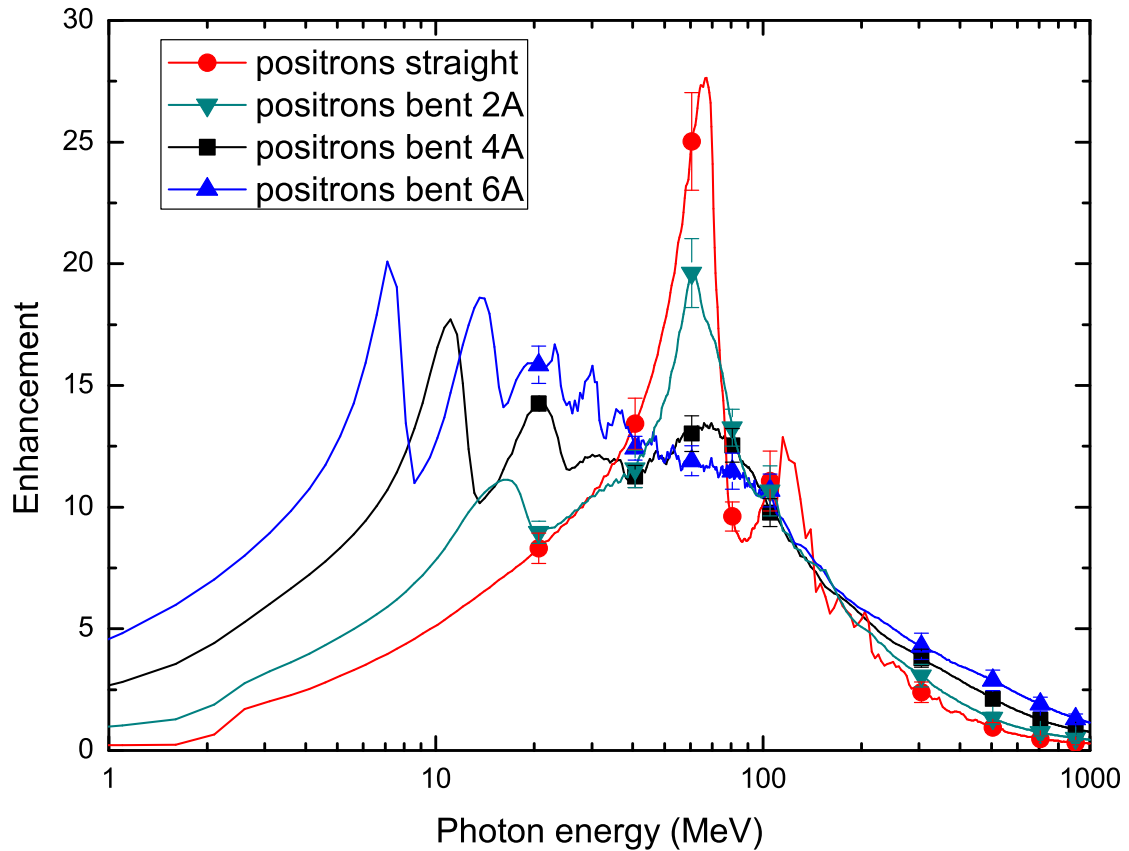


Figure 5.13: Comparison of enhancement of radiation spectrum of 10 GeV positrons channeling in large-amplitude Si(110) CU calculated for different bending amplitudes, as indicated. The spectra correspond to the emission cone $\theta_{\max} = 0.35$ mrad.

was compared for (110) planar and $\langle 110 \rangle$ axial channels of silicon crystal. In the planar case the channels are formed by equidistant planes with inter-planar distance 1.92 \AA , in axial case the shape of channels is two-dimensional and is illustrated in Figure 4.10. The comparison of parameters of channeling for axis $\langle 110 \rangle$ and plane (110) is presented in Table 5.8. Both acceptance and length characteristics are higher in planar case. Lower relative values of L_{p2} in case of axial channeling also indicate high number of short channeling segments.

The results of the simulations show that the channeling of positrons in plane (110) is characterized by much longer channeling length and higher acceptance. The only drawback of the channeling in this case is angular distribution of outgoing particles in the direction perpendicular to both normal of plane and direction of the beam. This distribution is limited for axial channeling in is much broader for the planar case.

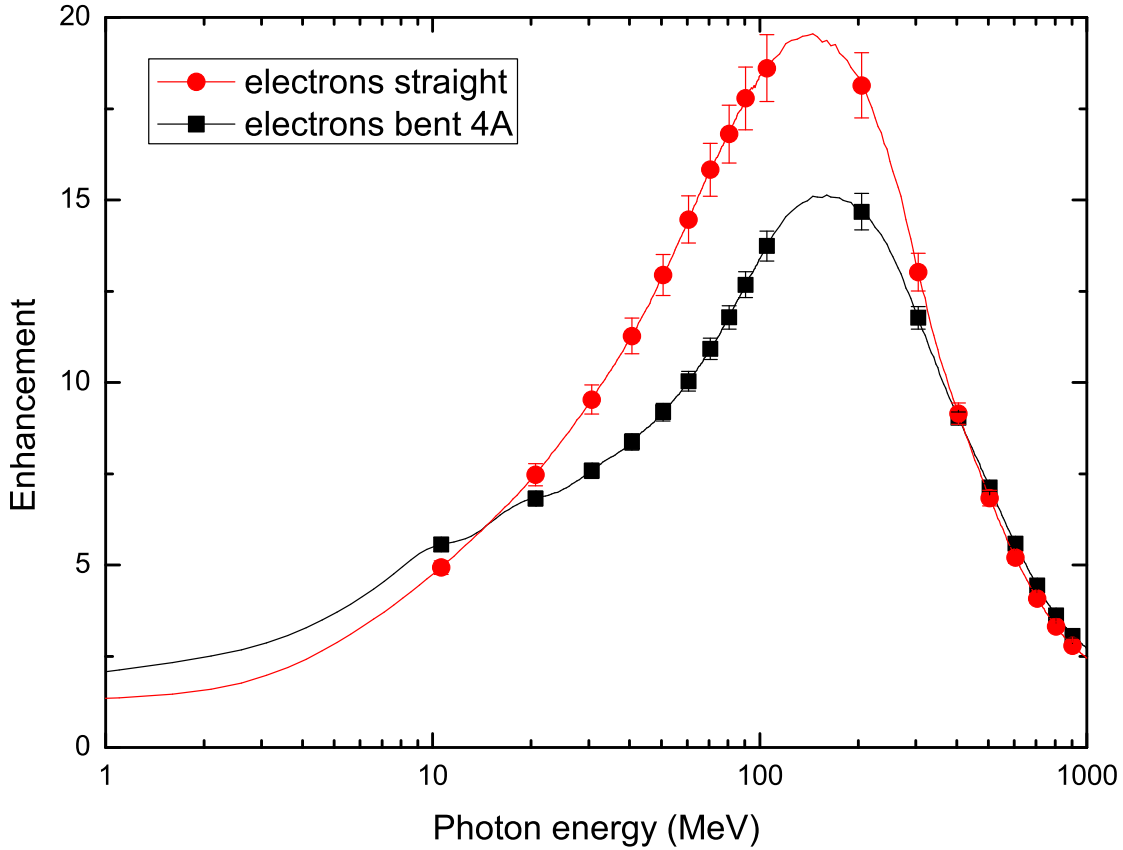


Figure 5.14: Comparison of enhancement of radiation spectrum of 10 GeV electrons channeling in large-amplitude Si(110) CU. The amplitude of bending is and 4 Å. The spectra correspond to the emission cone $\theta_{\max} = 0.35$ mrad.

For electrons the difference between axial and planar channeling is more pronounced. In Table 5.9 the comparison of acceptance and channeling lengths for axial and planar channeling of electrons with different energies is presented. The difference in the acceptance between axial and planar cases is 2-3 times, the difference in channeling length is 2-5 times depending on the calculation procedure. In this case the dechanneling length is lower, then the period of bending of the crystal and therefore the case of periodically bent crystal is omitted.

The effect of lower dechanneling length in axial case is caused by higher probability of collision with atoms of the medium. Trajectories of channeling electrons are located in close vicinity of atom strings, marked by red and green in Figure 4.13. The local density of atoms in this region is few times higher than in case of planar channeling which results in higher dechanneling rate.

To estimate quantitatively this effect, consider the cylinder directed along row

| Projectile, direction | a (Å) | \mathcal{A} (%) | L_{p1} (μm) | L_{p2} (μm) |
|-------------------------------|---------|-------------------|----------------------------|----------------------------|
| e^+ , $\langle 110 \rangle$ | 0 | 76.5 ± 1.5 | 251.6 ± 4.7 | 121.4 ± 3.3 |
| | 2 | 57.0 ± 1.0 | 171.3 ± 3.5 | 71.93 ± 1.4 |
| e^+ , (110) | 0 | 97.1 ± 0.9 | 301.9 ± 3.7 | 271.5 ± 5.5 |
| | 2 | 89.8 ± 2.1 | 300.5 ± 4.9 | 256.2 ± 7.8 |
| | 4 | 81.6 ± 2.6 | 287.1 ± 6.5 | 209.3 ± 8.9 |

Table 5.8: Acceptance and mean channeling lengths for 10 GeV positrons in 320 μm thick periodically bent Si crystals in axial $\langle 110 \rangle$ and planar (110) channels.

| Projectile, direction | ε (GeV) | \mathcal{A} (%) | L_{p1} (μm) | L_{p2} (μm) | L_d (μm) |
|-------------------------------|---------------------|-------------------|----------------------------|----------------------------|-------------------------|
| e^- , $\langle 110 \rangle$ | 0.855 | 32 ± 4 | 5 ± 1 | 5 ± 1 | 3 ± 1 |
| | 1.6 | 34 ± 3 | 6 ± 1 | 7 ± 1 | 4 ± 1 |
| | 6.7 | 36 ± 3 | 15 ± 1 | 17 ± 1 | 10 ± 3 |
| | 10 | 36 ± 2 | 19 ± 1 | 21 ± 1 | 13 ± 1 |
| | 20 | 37 ± 4 | 31 ± 3 | 31 ± 2 | 21 ± 3 |
| e^- , (110) | 0.855 | 59 ± 4 | 13 ± 1 | 14 ± 1 | 9 ± 3 |
| | 1.6 | 61 ± 4 | 19 ± 1 | 21 ± 1 | 14 ± 1 |
| | 6.7 | 64 ± 4 | 62 ± 5 | 56 ± 3 | 49 ± 4 |
| | 10 | 65 ± 4 | 81 ± 7 | 73 ± 4 | 68 ± 10 |
| | 20 | 68 ± 3 | 129 ± 10 | 112 ± 6 | 110 ± 10 |

Table 5.9: Comparison of acceptance and channeling lengths for axial and planar channeling of electrons with different energies in straight 320 μm thick Si crystal.

of atoms along $\langle 110 \rangle$ axis. The local density of atoms in such cylinder depends on its radius and for high values of radius goes to the average density of the crystal. Dependence of local density of the medium on the radius of cylinder is shown in Figure 5.15. The value of density is same for two cases at large radius limit (average density of the crystal is the same for both cases), but is few times bigger in axial case for radius lower than 0.5 Å. For small values of radius e.g. 0.3 Å such cylinder contains 3.5 times more atoms than same cylinder directed in (110) plane. This leads to proportionally higher probability of hard collision of projectiles with very low impact parameter and dechanneling.

5.4 Rechannelling in periodically bent crystals

The finite curvature radius of the crystal in simulations in Section 5.3 leads to increase of role of both dechanneling and rechannelling effects due to two reasons.

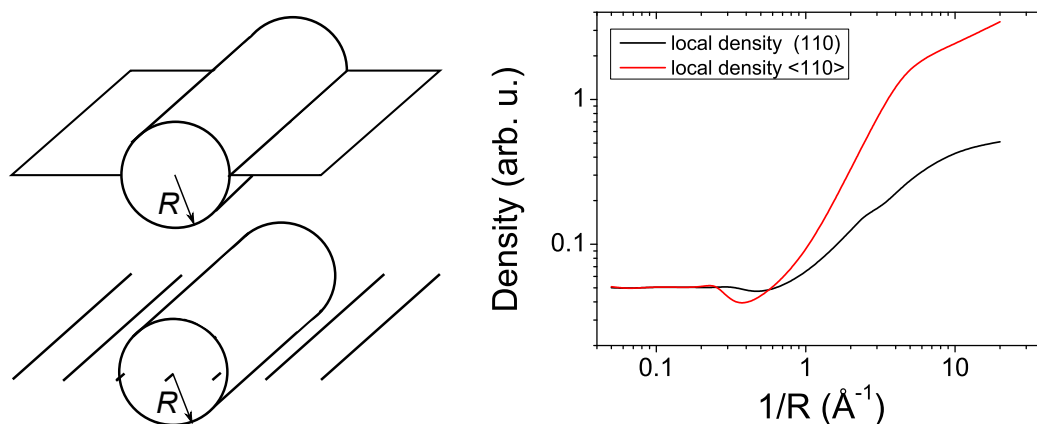


Figure 5.15: Schematic illustration of local density calculation method for planar and axial channels (left). The dependence of local density of atoms on inverse cylinder radius (right).

First, curvature of the crystal plane creates a centrifugal force and leads to the dechanneling. Second, change of the center line of the channel may lead to decrease of angle between axis and projectiles out of the channel, which results in volume capture and rechanneling. The role of these effects depends periodically on the coordinate of the projectile.

In Figure 5.16 the dependence of channeling fractions on penetration distance with and without rechanneling are presented for the periodically bent crystal. The bending is done along the $\langle 110 \rangle$ axis with amplitude of 2 \AA . The curve of channeling fraction with rechanneling consists of the normal decreasing part and includes oscillatory part with the period of bending of the crystal.

To analyze this effect quantitatively consider Figure 5.17 where the derivative of the channeling fraction (with rechanneling) is compared with the following approximate following fitting formula: $dn/dz = n(z) \sin(2\pi z/\lambda_u) + const$, where $n(z)$ is the channeling fraction and λ_u is the period of crystal bending. This fitting indicates both exponential decay of number of particles in channel and dependence on the value of first derivative of the channel bending profile. It indicates that the probability of dechanneling is proportional to the angle between direction of the beam and current direction of the channel.

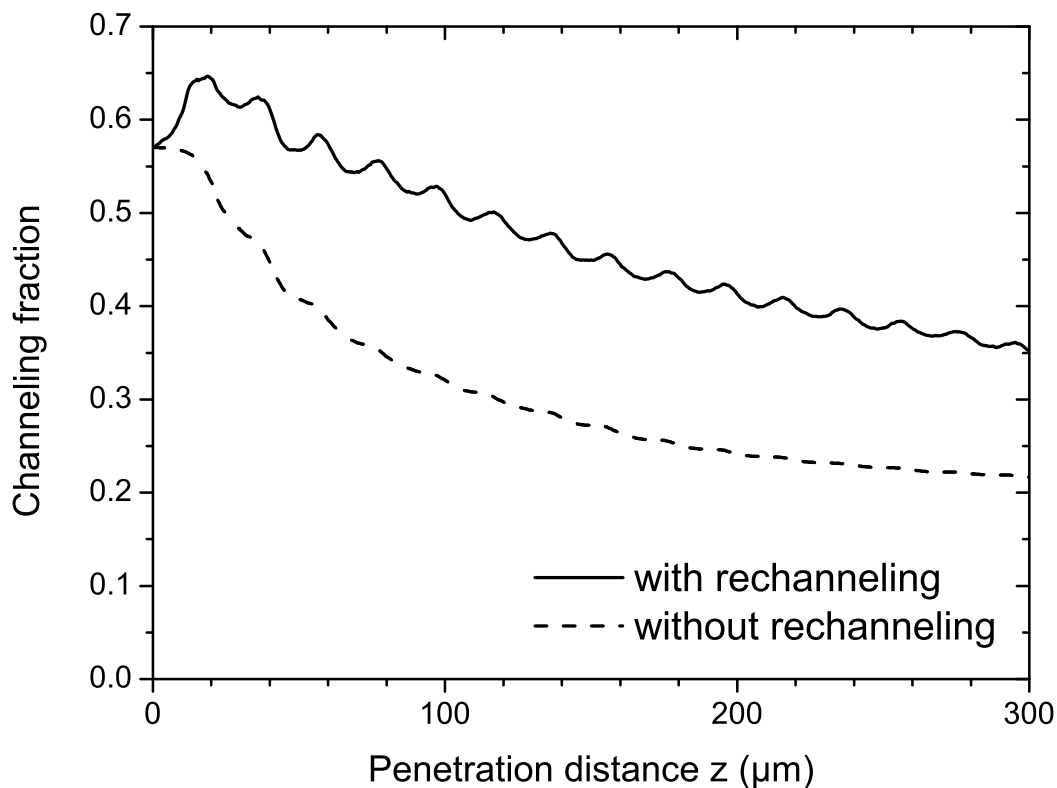


Figure 5.16: Channeling fraction versus penetration distance for 10 GeV positions in a $320 \mu\text{m}$ thick silicon crystal periodically bent along the $\langle 110 \rangle$ axis. The bending amplitude and period are 2 \AA and $39.6 \mu\text{m}$, respectively. The solid curve corresponds to the channeling fraction including rechanneling. The dashed curve corresponds to the fraction excluding rechanneling.

5.5 Small-amplitude short-period undulator case study

Another important application of channeling phenomena is the small-amplitude undulator [33, 35, 34]. In this case the projectile propagates in the bent crystalline medium but in contrast with the medium in simulations in Section 5.2 the bending amplitude and period of the crystal are lower than the interplanar distance and the period of channeling oscillations, respectively. The difference in the period of oscillations results in the higher energy of photon emission. The shape of the channel defines the amplitude and period of channeling oscillations and corresponding radiation. Channeling in bent crystals leads to the special type of radiation, which depends on the parameters of crystal bending.

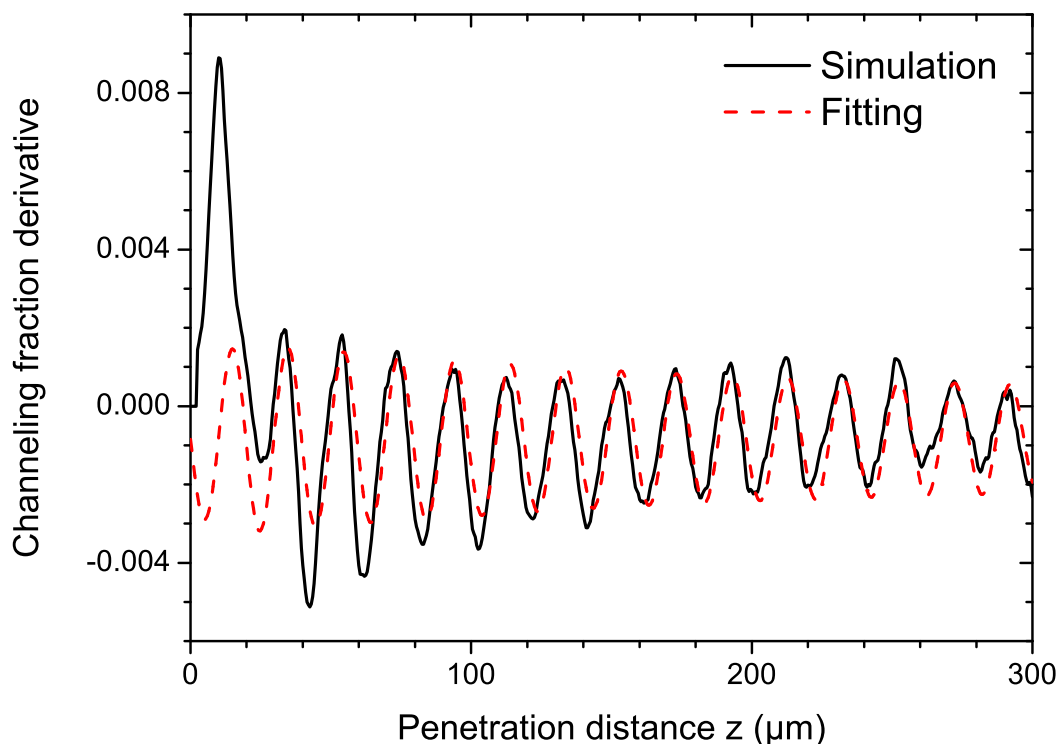


Figure 5.17: The derivative of the channeling fraction of positrons in periodically bent Si(110) axial channel: simulated versus fitting results.

In recent years two main types of crystalline undulators were discussed: small-amplitude short-period (SASP) undulators [27, 34], and large-amplitude large-period (LALP) undulators [87, 33]. The bending amplitude is considered high if its value is large then inter-planar distance of the crystal. The bending period is considered high if its value is larger than the period of channeling oscillations in this channel. Short-period undulators can be used to create radiation of higher photon energy than channeling radiation.

The cases of LALP and SASP crystalline undulators can be distinguished by the value of the parameter C defined in eq. (2.46). In the case of LALP undulator the value of this parameter is considered small $C \ll 1$ because the projectile has to follow bends of crystalline planes or axes to produce appropriate radiation. In this case the increase of amplitude of bending leads to the increase of radiation intensity, but also leads to the increase of C which is the limiting factor. In SASP undulators the parameter C can be also formally calculated and its value is higher than 1. In this case projectiles are unable to follow bends of the crystalline medium. What produces the undulator radiation in this case is the periodic force acting on

the projectile due to the rapid change of the interplanar potential. In this case the increase of amplitude of bending also increases the intensity of radiation, but decreases the number of channeling projectiles. The amplitude in this case is limited to the half of interplanar distance.

In recent series of experiments at Mainzer Microtron [27] with 600 and 855 MeV electrons the effect of small-amplitude short-period undulator was observed. Another set of experiments with diamond crystalline undulators is planned within the E-212 collaboration at the SLAC facility (USA) with 10...20 GeV electron beams [15]. Current experimental implementations of small-amplitude short-period undulators are based on thin Si or C crystals doped with small amount of Ge atoms. These crystals are produced using Molecular Beam Epitaxy technology.

As a case study consider planar channeling in straight and periodically bent crystals of silicon and diamond. The thickness of the crystal is $4 \mu\text{m}$, the period of bending λ_u is $0.4 \mu\text{m}$ and the bending amplitude is 0.4 \AA which is lower than half of interplanar distance in both cases. The motion of charged projectiles in the straight crystal corresponds to a classical channeling regime. The second case corresponds to a SASP crystalline undulator regime. The beam is oriented in a (110) plane, avoiding axial channeling directions.

In Figure 5.18 the results of the simulation of radiation of 20 GeV electrons and positrons are compared for the cases of straight and periodically bent diamond (top) and silicon (bottom) crystals. At this energy, the natural emission angle is $1/\gamma = 25.6 \mu\text{rad}$. The value of beam emittance was taken $\psi = 5 \mu\text{rad}$. The angular aperture of the detector was taken $\theta_{max} = 150 \mu\text{rad}$, which is 5.8 times higher than natural emission angle, and covers most of the radiation of projectiles.

In both figures the first peak of each curve (below 1 GeV) corresponds to channeling radiation, second (6 GeV) and other peaks are present only in radiation in bent crystals and correspond to undulator radiation. Bending of a crystal leads to significant suppression of channeling peak. This effect can be described in an average potential model of channeling. With increase of bending amplitude the depth of the potential well decreases and the width of the potential well grows. This results in a decrease of number of channeling projectiles and in lower frequencies of channeling oscillations.

Another factor of suppression of channeling radiation is that for the energy of the projectiles of 20 GeV the characteristic period of channeling oscillations in simulated trajectories for positrons in C(110) channels is $9 \mu\text{m}$ and $11.5 \mu\text{m}$ in Si(110)

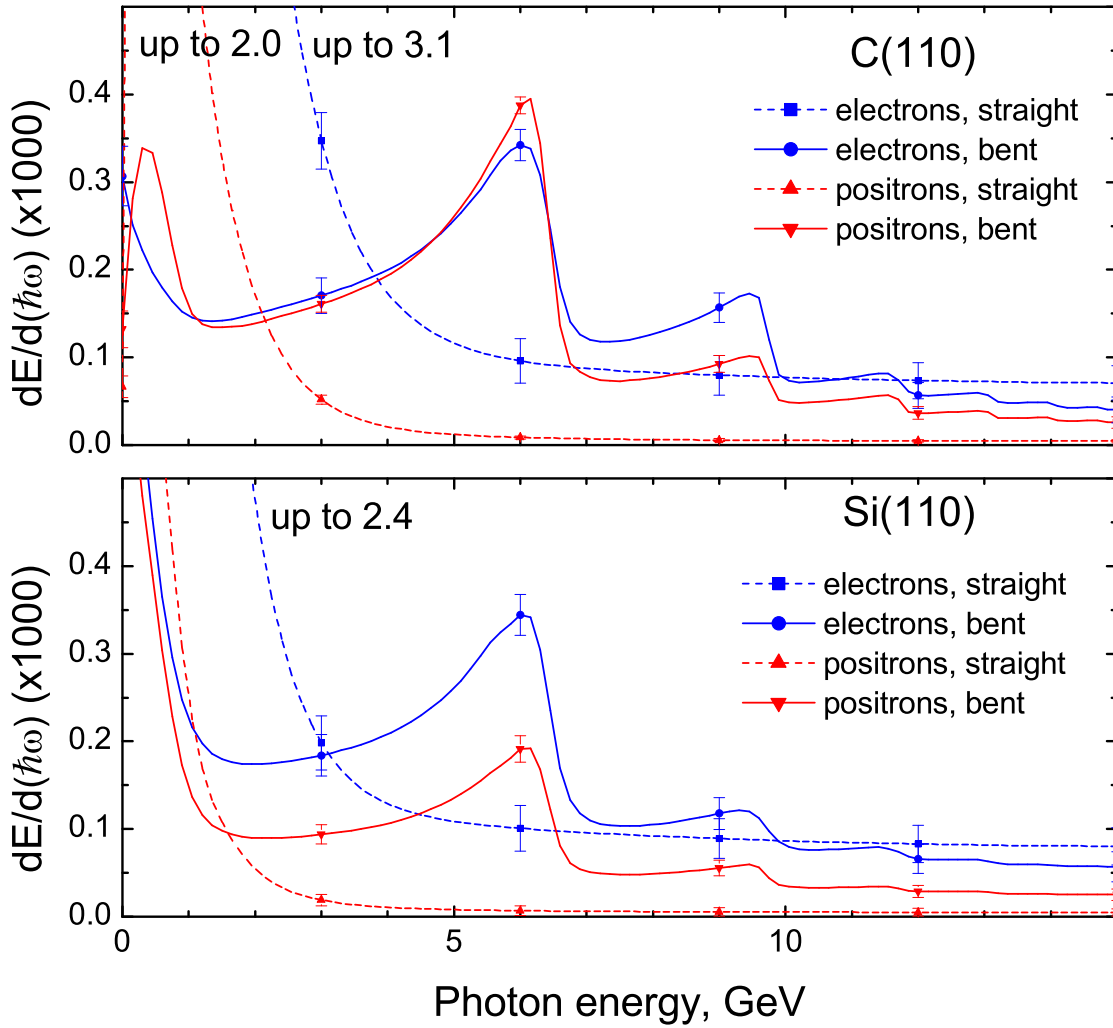


Figure 5.18: Radiation spectra for 20 GeV electrons and positrons in straight and periodically bent diamond (top) and silicon (bottom) crystals. Bending amplitude and period are 0.4 \AA and $0.4 \mu\text{m}$, respectively.

channels. This period is higher than crystal thickness and it further decreases the effect of channeling in comparison with case of pure channeling in thick crystals. The comparison of radiation spectrum for long ($24 \mu\text{m}$) and short ($4 \mu\text{m}$) crystals is shown in Figure 5.19. The values for smaller thickness are multiplied by the factor of 6 for comparison. As can be seen from the plot the undulator peaks of both curves nearly coincide, while the shape of the curves in the region of lower photon energies is significantly different. In case of a thick crystal channeling produces a sharp peak of radiation around the photon energy of 150 MeV. In case of a smaller thickness the channeling peak is not present and the radiation is produced by a synchrotron

effect.

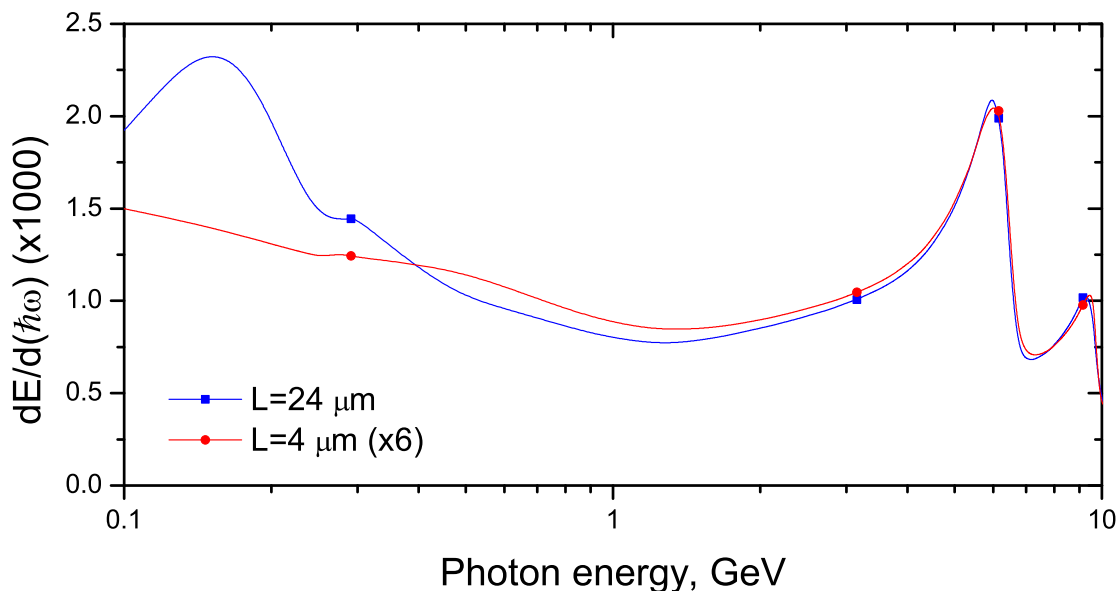


Figure 5.19: Comparison of radiation spectrum for 20 GeV electrons in bent diamond crystal for two different values of thickness, as indicated. The value $L = 24 \mu\text{m}$ exceeds characteristic channeling oscillations period while $L = 4 \mu\text{m}$ is lower than this period. Note the absence of channeling radiation peak around 150 MeV in the latter case. For the sake of comparison, the curve for $L = 4 \mu\text{m}$ is multiplied by the factor of 6.

The radiation emission of projectiles in this simulation is directed strongly along the beam. Within small aperture undulator creates radiation with very narrow distribution of photon energies. In Figure 5.20 the dependence of radiation of projectiles on aperture of detector θ_{max} is shown. In the case of narrow aperture $\theta_{max} = 10 \mu\text{rad}$ the structure of peaks is very sharp. With increase of the aperture absolute values of number of photons with high energy increases, but the width of the peak increases also. At the value of $\theta_{max} = 150 \mu\text{rad}$ the radiation spectrum saturates and is the same for higher apertures.

5.5.1 Crystalline undulator stack

The effect of suppression of channeling radiation in short periodically bent crystals can be used in order to produce undulator radiation with higher efficiency. In order to increase the energy of undulator radiation without increasing channeling radiation it is possible to use stack of short crystalline undulators instead of one

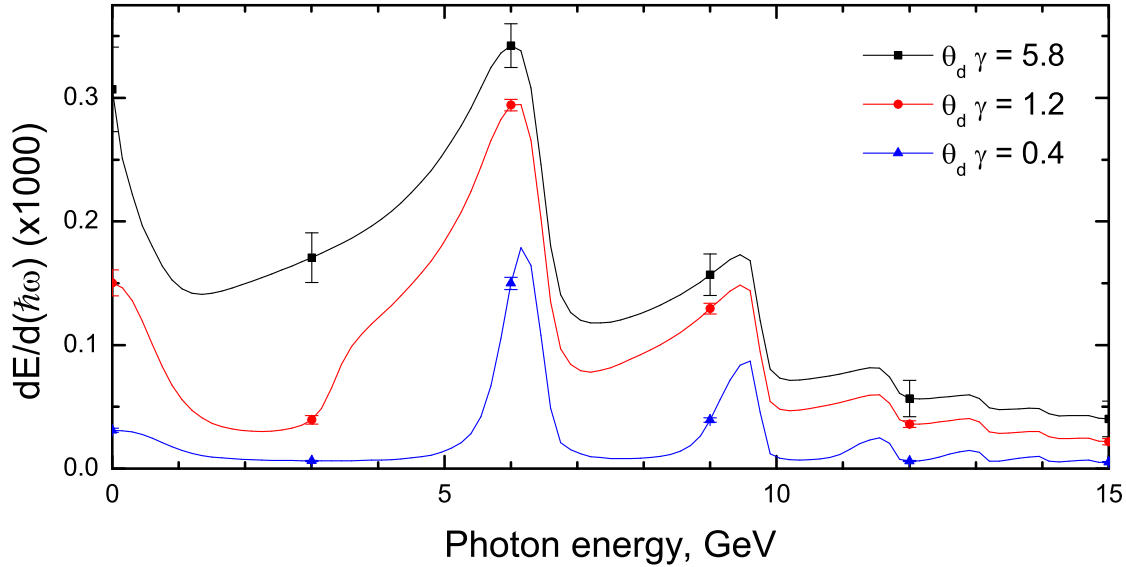


Figure 5.20: Comparison of radiation spectrum for 20 GeV electrons in CU for different apertures $\theta_{max} = 10, 30, 150 \mu\text{rad}$ which correspond to $0.4/\gamma, 1.2/\gamma$ and $5.8/\gamma$ where $1/\gamma$ is the natural emission angle.

long undulator. The scheme of such crystalline system is given in Figure 5.21. In the system the projectile passes several layers of periodically bent crystalline medium, the radiation produced at all layers adds to the total radiation produced by projectile. For SASP undulator the thickness of layers can be taken in the interval between the bending period λ_u and the characteristic channeling period of projectile. Such choice of the parameters leads to absence of full channeling oscillation periods in each channeling segment of trajectory of projectile which results in suppression of channeling radiation. The effect of undulator radiation in the system remains and grows with increase of number of layers.

To simulate the effect of channeling in CU stack the following system was modeled. A set of $l = 4 \mu\text{m}$ layers of periodically bent crystals was put in the simulation box with $l' = 4 \mu\text{m}$ gaps between layers, the period of crystal bending was set to $\lambda_u = 0.4 \mu\text{m}$. Such system corresponds to a case of the crystalline undulator stack. In this case the projectiles are captured in the first crystal, leave the crystal at some point, and have to be captured again in the next crystal layer. The process of recapturing of the projectiles in the channeling mode leads to increase of angular dispersion of velocity of projectiles and the decrease of the number of channeling particles with the growth of the number of layers.

The thickness of layers in this simulation is set below the channeling oscillations

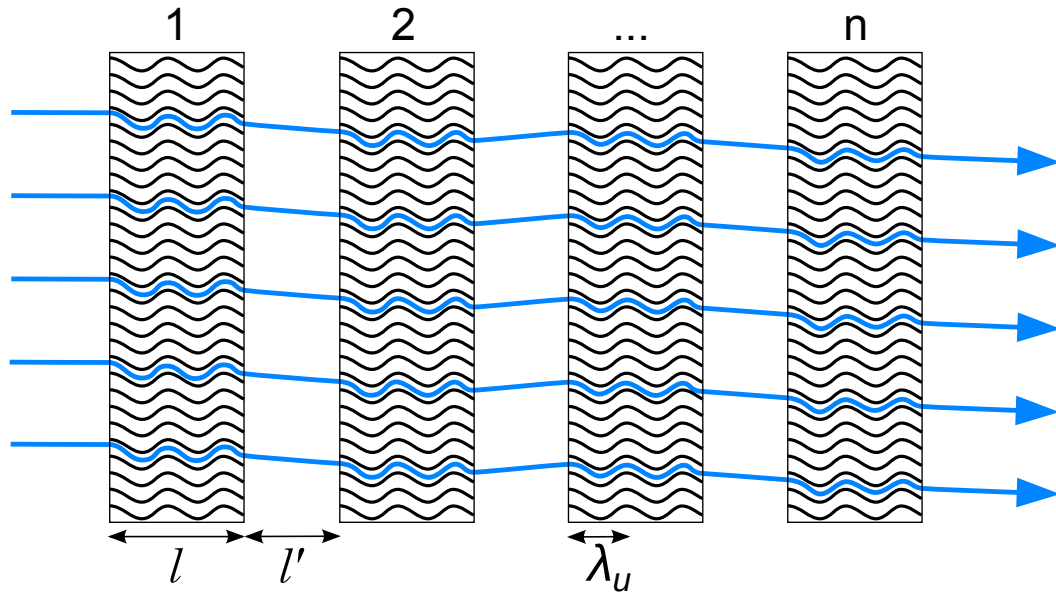


Figure 5.21: The scheme of the CU stack made of n periodically bent crystal layers each of the thickness l . The quantity l' stands for the gap between the layers. Blue lines illustrate the trajectories of projectiles.

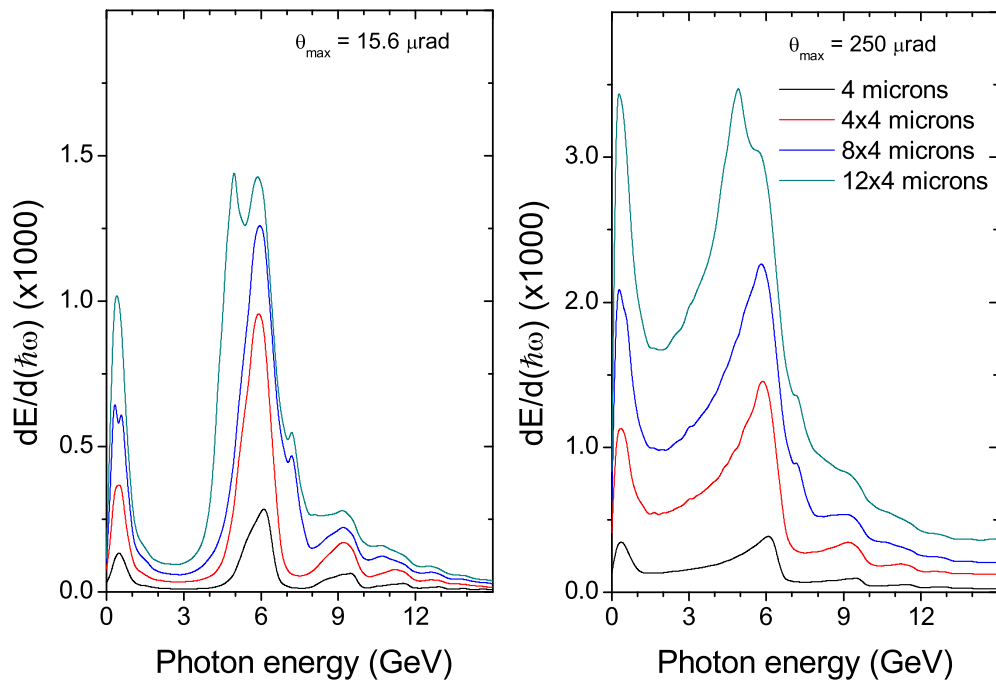


Figure 5.22: Radiation spectra for the small (left) and large (right) apertures calculated for different number of layers in a stack (as indicated in the common legend). The data refer to 20 GeV positrons, the bending amplitude and period are 0.4 \AA and 400 nm , respectively.

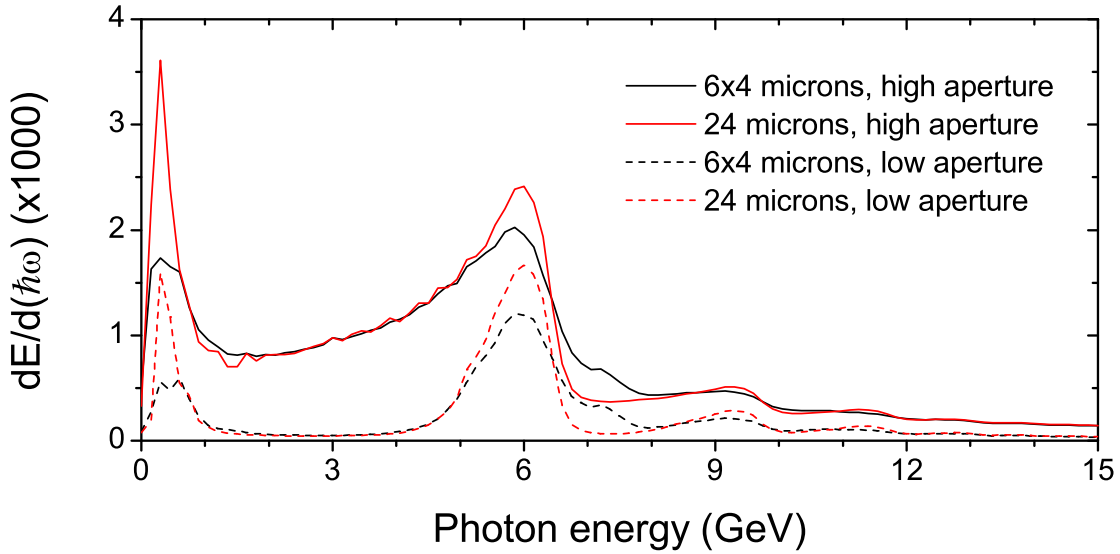


Figure 5.23: Comparison of radiation spectra formed by positrons in a crystal of $24 \mu\text{m}$ and in a stack of 6 crystals of $l = 4 \mu\text{m}$. The spectra calculated for two different apertures $15.6 \mu\text{rad}$ (dashed lines) and $250 \mu\text{rad}$ (solid lines). The beam energy is 20 GeV, crystal bending aperture and period are 0.4 \AA and 400 nm , respectively.

period ($11.5 \mu\text{m}$) but above the period of crystal bending ($0.4 \mu\text{m}$). Such choice of the crystal thickness leads to the suppression of channeling radiation due to the lack of full oscillation periods, but the undulator radiation remains.

In Figure 5.22 the comparison of radiation spectrum for different number of layers in stack is given. The energy of both synchrotron and undulator radiation grows linearly with the number of stack layers until 4 for small aperture. For higher number of stack layers the angular distribution of projectile velocities gets wider and the radiation in a narrow cone saturates. For higher aperture the growth of the intensity peak continues.

In Figure 5.23 the radiation of single crystal crystalline undulator ($24 \mu\text{m}$) is compared to a stack of undulators ($6 \times 4 \mu\text{m}$). It can be seen, that for the stack case the channeling peak in the radiation spectrum is suppressed, while the undulator peak is nearly the same, as for the case of a single crystal.

Chapter 6

Channeling in binary crystalline structures

In this chapter the channeling of electrons and positrons in Si-Ge superlattices is studied. These superlattices with variable concentration of Ge atoms can be applied for bending and periodic bending of crystals [100, 102] see Section 2.7. The use of atomistic molecular dynamics approach to channeling described in Chapter 3 allows natural description of channeling in crystals with composite structures.

In the first section the classical molecular dynamics approach is applied to study structure deformation of ideal Si crystal due to doping with Ge atoms. In Figure 6.1 the example of a Si-Ge crystalline sample with 5% Ge concentration is shown. Both Si and Ge crystals have the same FCC crystalline structure and close values of the lattice parameters. The presence of Ge atoms results in gradual change of the lattice parameter of the resulting superlattice. The functional form of the dependence of lattice parameter on the concentration of Ge is discussed in Section 6.1.

In the Section 6.2 the influence of Ge doping on channeling process and characteristic dechanneling length. It is shown that the dependence of dechanneling length on Ge concentration is monotonous and can be approximated by simple analytic function. The Section 6.3 is devoted to the study the influence of Ge concentration on the channeling radiation process of both electrons and positrons. It is shown that the dependence of the intensity of the channeling radiation on Ge concentration is monotonous and can be also described by the analytic expression. It is shown that the influence of Ge atoms on channeling radiation is less pronounce than its influence on radiation in amorphous medium case, which leads to both change of radiation

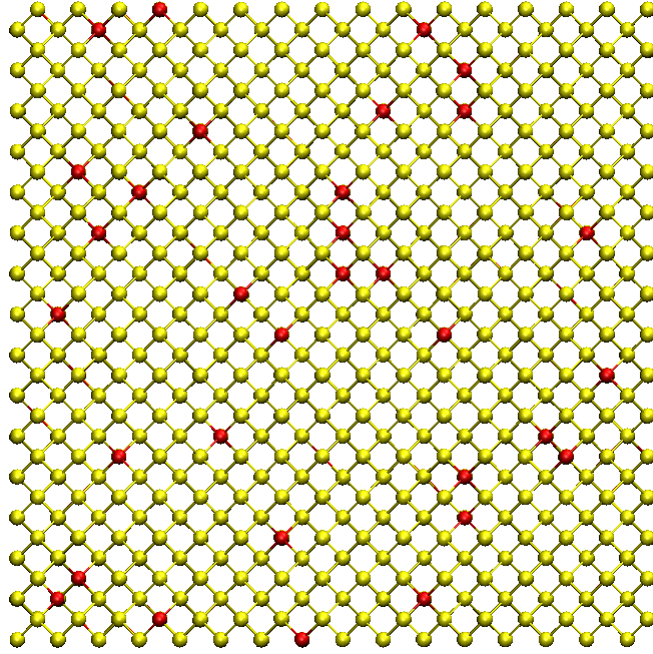


Figure 6.1: Illustrative $\text{Si}_{1-x}\text{Ge}_x$ binary crystal sample with Ge concentration $x = 0.05$. The silicon and germanium atoms are shown in yellow and red, respectively. The Ge atoms occupy position in the same grid structure as Si but the difference in the lattice parameter leads to a deformation of the whole sample.

spectrum and the enhancement of radiation spectrum.

6.1 Modeling a Si-Ge crystal structure

Si and Ge crystals have diamond cubic crystalline structure (FCC) with different lattice constant. Unit cell size for Silicon is 5.4309 \AA , for Germanium it is 5.6575 \AA . Replacing some fraction of Si atoms in crystal with Ge atoms leads to increase of linear dimensions of a crystalline structure, this expansion can be considered linear for small concentration of Ge atoms.

In order to determine parameters of the linear expansion model for small angles and to obtain the dependence of expansion coefficient on concentration consider interactions of Si and Ge atoms in Si-Ge superlattice. These interactions can be modeled using Stillinger-Weber [57] potential. This many-body potential describes interaction of Si-Si, Ge-Ge and Si-Ge atom pairs and all cases of triple interaction. The general form of this potential is described in the Section 3.4 a Eq. (3.10). The parameters for this interaction potential for Si-Ge crystals are summarized in

Table 6.1 [115].

| A | B | p | q | α | γ | $\sigma_{\text{Si-Si}}$ (nm) | $\sigma_{\text{Si-Ge}}$ (nm) | $\sigma_{\text{Ge-Ge}}$ (nm) |
|------------------------------|--------|----------|----------|----------|----------|------------------------------|------------------------------|------------------------------|
| 7.050 | 0.6022 | 4 | 0 | 1.8 | 1.2 | 0.2095 | 0.2138 | 0.2181 |
| | | Si-Si-Si | Si-Si-Ge | Si-Ge-Ge | Ge-Si-Si | Ge-Si-Ge | Ge-Ge-Ge | |
| λ_{ijk} | | 21.0 | 23.1 | 25.5 | 25.5 | 28.1 | 31.0 | |
| $\epsilon_{ijk}, 10^{-19} J$ | | 3.472 | 3.371 | 3.273 | 3.273 | 3.178 | 3.085 | |

Table 6.1: Parameters for the Stillinger-Weber potential for Si-Ge atomic interactions. The potential energy is given by Eq. (3.10). The data are taken from paper [115].

As a case study we consider a cubical sample of Si crystal with the cube side 10.7 nm and the total number of atoms 64000. To model the formation of the Si-Ge superlattice in this cube we substitute randomly some fraction of Si atoms. For several values of Ge concentration atoms of the sample were randomly replaced by atoms of Ge and the structure of the sample was optimized using Velocity Quenching energy minimization algorithm. In Figure 6.1 the sample with 5% Ge concentration is illustrated.

The basic idea behind this algorithm is to simulate molecular dynamics of the system while absorbing all kinetic energy in the most efficient way. At each step of the calculation the motion of all atoms in the system by means of the classical equations of motion is considered. The kinetic energy of all particles is monitored. At the point at which the kinetic energy of an arbitrary particle is maximal, the algorithm sets the speed of atom equal to zero. The points in the configurational space, at which the kinetic energy are maximal corresponds to the minimum of the potential well in which a particle moves. This algorithm transforms the atomic structure of the simulated sample and finds the structure corresponding to the minimal potential energy.

After optimization of energy of the system the crystalline structure type is the same, but the distances between atoms change which leads to the increase of the linear size of the sample. The dependence of the change of linear sizes on germanium concentration is presented in Figure 6.2.

The results of the simulations show, that this dependence is linear for the whole range of concentration values. The simulated value of lattice expansion for 100% concentration of Germanium atoms is 4.3%, which is in a good agreement with experimental value of 4.17% (unit cell size for Si - 5.4309 Å, for Ge - 5.6575 Å).

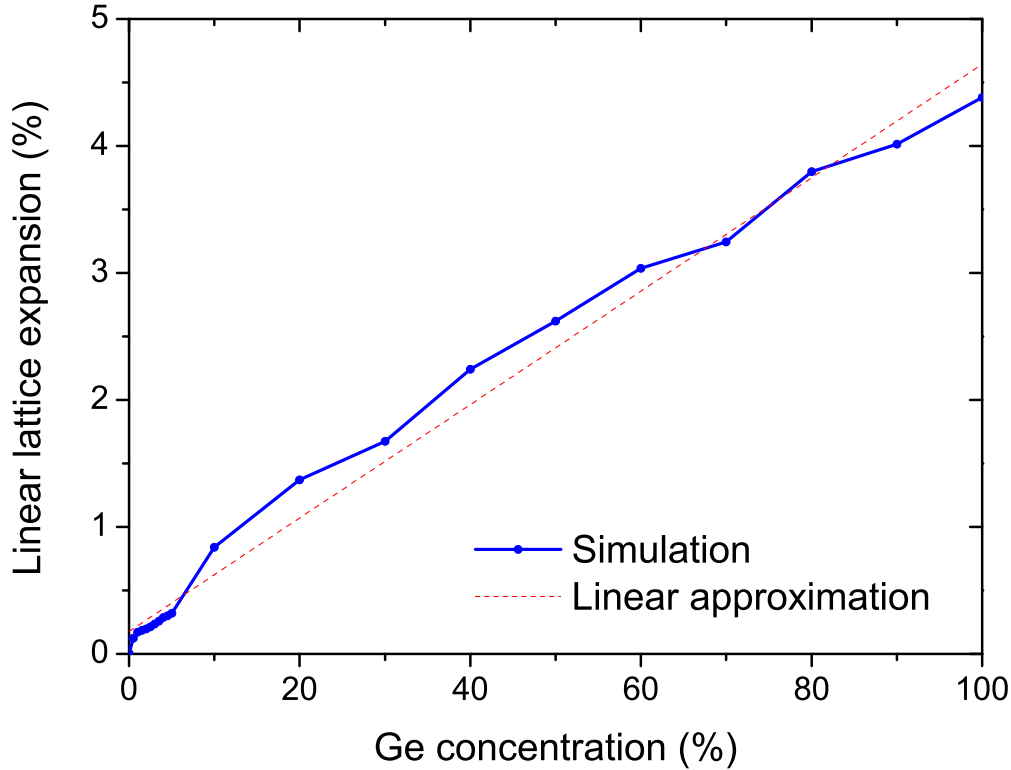


Figure 6.2: Dependence of the simulated linear grid expansion coefficient of a $\text{Si}_{1-x}\text{Ge}_x$ on the Ge atoms concentration x (in per cent). The dependence can be approximated by linear function (red dashed curve) with high precision.

Another important characteristic of crystalline medium which depend on the presence of doped atoms is the amplitude of thermal vibrations. From the literature [2] the following amplitudes for Si and Ge monocrystals are known: 0.075 Å and 0.085 Å.

In order to simulate thermal vibrations of atoms in these crystals optimized geometrical samples from previous simulations were used as initial state for molecular dynamics simulations. These simulations were carried out with a constant temperature of 300 K with Langevin thermostat algorithm. The simulation of the atomic motion was carried out using Velocity-Verlet [131, 132] algorithm. The simulation time was set to 72 psec., the time step of integration was set to 0.02 fsec., the thermostat damping time was set to 20 fsec. The computed trajectories of atoms of the sample were analyzed in term of RMSD (root-mean-square deviation).

The simulated value of thermal vibrations for Si is 0.048 Å, for Ge is 0.039 Å and for $\text{Si}_{0.5}\text{Ge}_{0.5}$ is 0.049 Å. The simulation results show systematically lower am-

plitude of thermal vibrations, but indicate that for the Si-Ge crystals in general the amplitude of thermal vibrations might be higher than for pure Si or Ge crystals due to impurity of the material.

6.2 Channeling in Si-Ge composite crystals

The variation of the Ge concentration in $\text{Si}_{1-x}\text{Ge}_x$ leads to a variation of distances between crystal planes, which lead to bending of the crystal. In order to estimate the influence of doped atoms on channeling process the series of numerical simulation were carried out. In each of these simulations the channeling was studied in a straight crystal with the constant concentration of Ge. Dependence of numerical parameters of channeling effect on the concentration of Ge was obtained.

For the simulations two energies of 5 GeV and 10 GeV were considered for the cases of both electrons and positrons. The value of the crystal thickness was taken 100 μm in order to exceed maximal dechanneling length in both pure Si and pure Ge crystals. The channeling plane is (110).

Model 1 For the small level of concentration consider a simple model of a crystal: in a first approximation some atoms of initial Si lattice were randomly substituted by Ge atoms with given probability. Interaction of a projectile with such atoms has different parameters of Molière potential. In Figure 6.3 the dependence of dechanneling length on Ge concentration for small values of concentration is shown.

Model 2 In order to simulate crystals with higher concentration of Ge atoms consider an improved model, in which the distance between crystal planes depends linearly on concentration. This dependence of crystalline grid expansion on Ge concentration is described in the Section 6.1.

Model 3 Another approach to the simulation of channeling processes in composite crystals is to use an optimized crystal geometries as a unit cell for construction of the medium. This approach was tested for the case of 5% Ge concentration. This approach showed similar results to both Model 1 and Model 2, but required much higher computational resources due to much larger number of atoms in the unit cell.

In Figure 6.4 the dependence of dechanneling length on Ge concentration is shown for all three models. Model 1 and Model 2 show very good agreement of

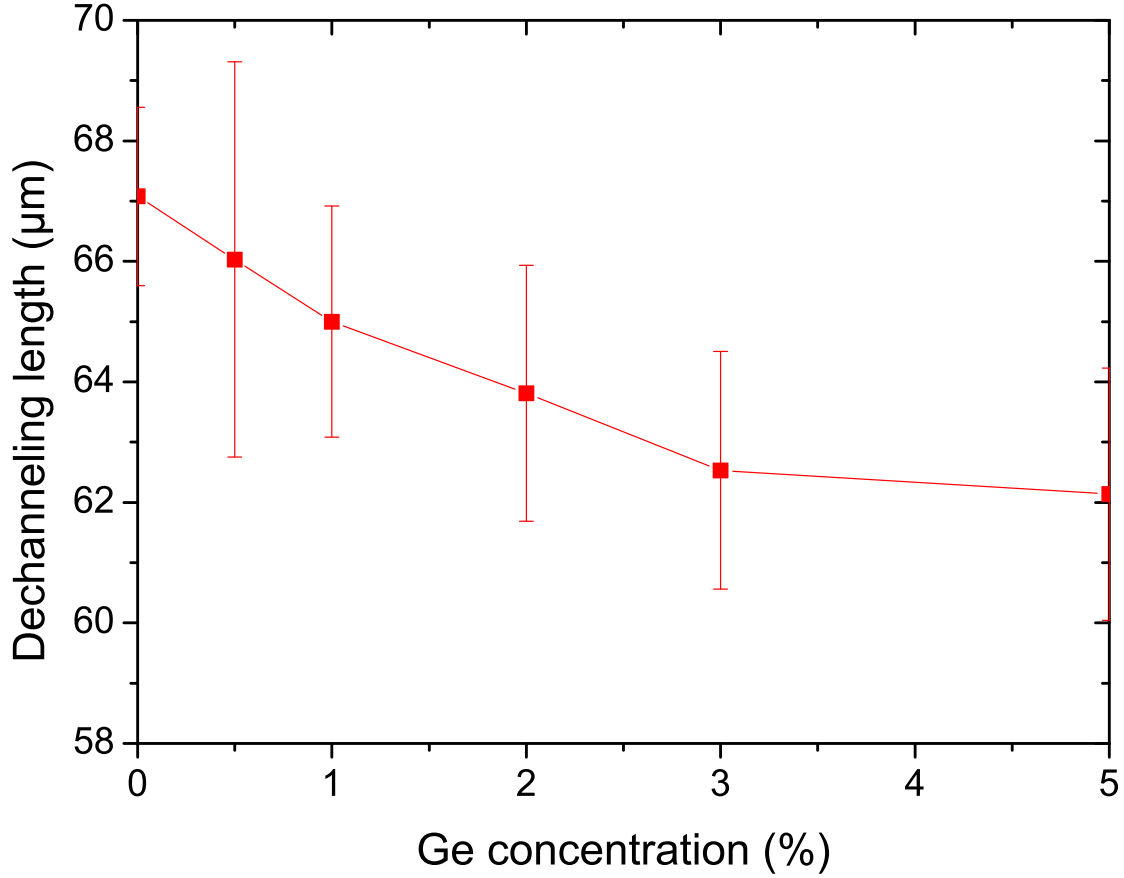


Figure 6.3: The dependence of dechanneling length of 10 GeV electrons in straight $\text{Si}_{1-x}\text{Ge}_x$ crystal on Ge concentration for small values of x .

results within error bars, the result for Model 3 gives higher value of the dechanneling length, but the statistical error is also higher. Using second model the dependence of dechanneling length on concentration of Germanium atoms in the whole range of concentration values was calculated.

In experiments the value of concentration of Ge atoms is usually set below 5% due to other restrictions. Therefore the decrease of dechanneling length with respect to pure Si crystal should be limited by 10%.

The dependence of the dechanneling length on the concentration of Ge can be fitted by following functional dependence:

$$L_d(x) = L_d(0)^{(1-x)^\alpha} L_d(1)^{x^\alpha} \quad (6.1)$$

where $L_d(0)$ is the dechanneling length of electrons in Si, $L_d(1)$ is the dechan-

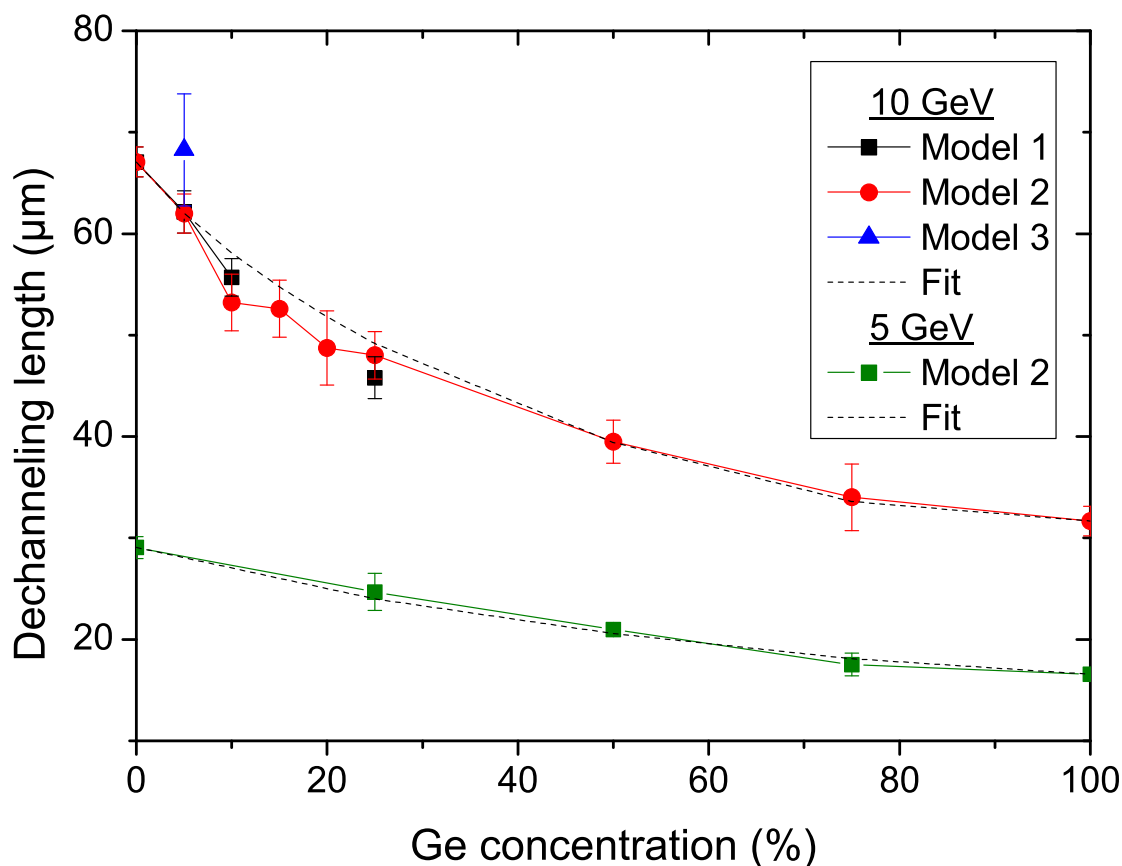


Figure 6.4: The dependence of dechanneling length of 10 GeV electrons in straight $\text{Si}_{1-x}\text{Ge}_x$ crystal on Ge concentration. Model 1 refers to simple random replacement of Si atoms with Ge, Model 2 adds linear scaling of crystalline lattice, Model 3 uses optimized geometry of the crystal.

channeling length of electrons in Ge, α is the fitting parameter. As a result of fitting of simulated curve in Figure 6.4 with such function the value of α was set to 1.06 for 10 GeV and 1.03 for 5 GeV.

6.3 Channeling radiation in composite crystals

The variation of Ge concentration in $\text{Si}_{1-x}\text{Ge}_x$ crystals leads to the change of parameters of channeling radiation of projectiles in medium. The following factors affect this process: increase of Ge concentration leads to increase of the depth of the interplanar potential energy well, increase of crystalline lattice scales leads to the higher interplanar distance and the higher channeling oscillations amplitude, lower

dechanneling length leads to decrease of intensity of radiation.

Using the trajectories calculated with model 2 from the previous section the spectrum of radiation of electrons in a composite crystal was studied. The results of calculations for electrons are given in Figure 6.5 and for positrons in Figure 6.6.

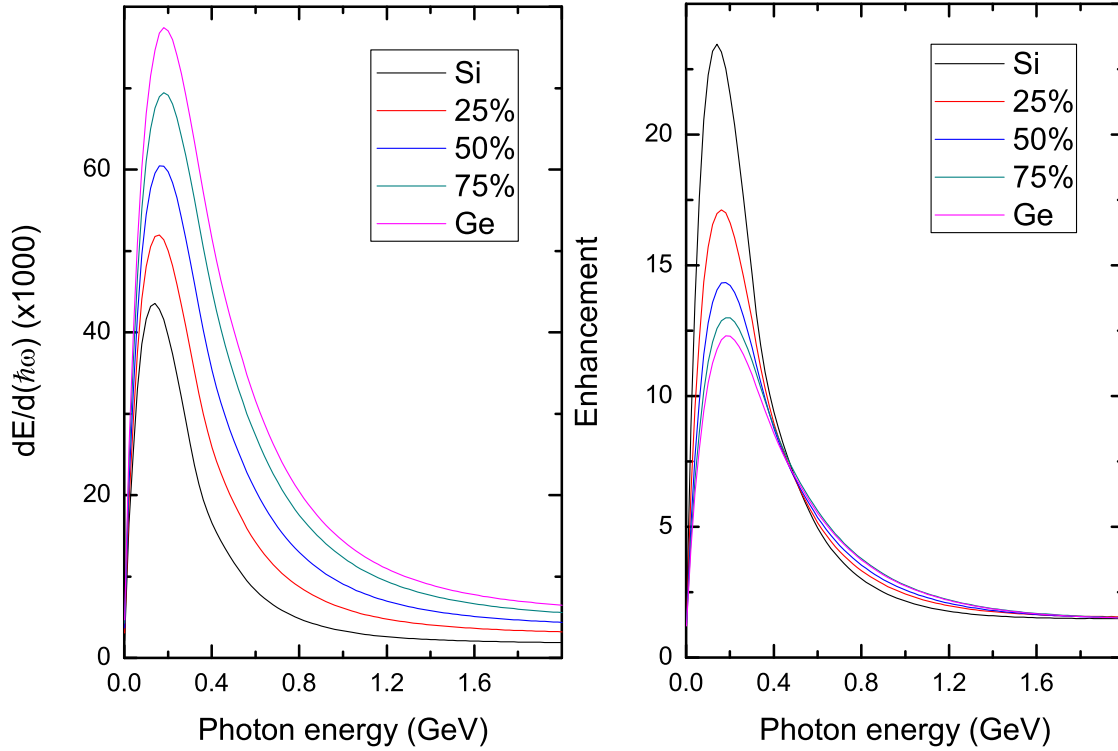


Figure 6.5: The radiation spectrum (left) and the radiation spectrum enhancement (right) of 10 GeV electrons channeling through $\text{Si}_{1-x}\text{Ge}_x$ crystals with different concentration of Ge ($x \cdot 100\%$) in (110) direction. Crystal thickness is 100 μm ; radiation aperture is 0.25 mrad ($4.9/\gamma$).

For both electrons and positrons the radiation spectrum (left panels) varies gradually with the change of Ge concentration and increases with higher concentration of Ge. The ratio of intensity in the maximum is 1.77 for electrons and 1.35 for positrons. The position of the maximum varies for electrons: 0.141 GeV for Si and 0.181 GeV for Ge, for positrons it is 0.061 GeV in both cases.

In the case of positrons the dechanneling length is much higher than the total thickness of the crystal sample for both Si and Ge. It means that the difference in intensity is caused only by increase of interplanar distance and change of the potential energy gradient. In case of electrons in addition to these factors the intensity is changing due to the change of dechanneling length, which is 30-50% lower in

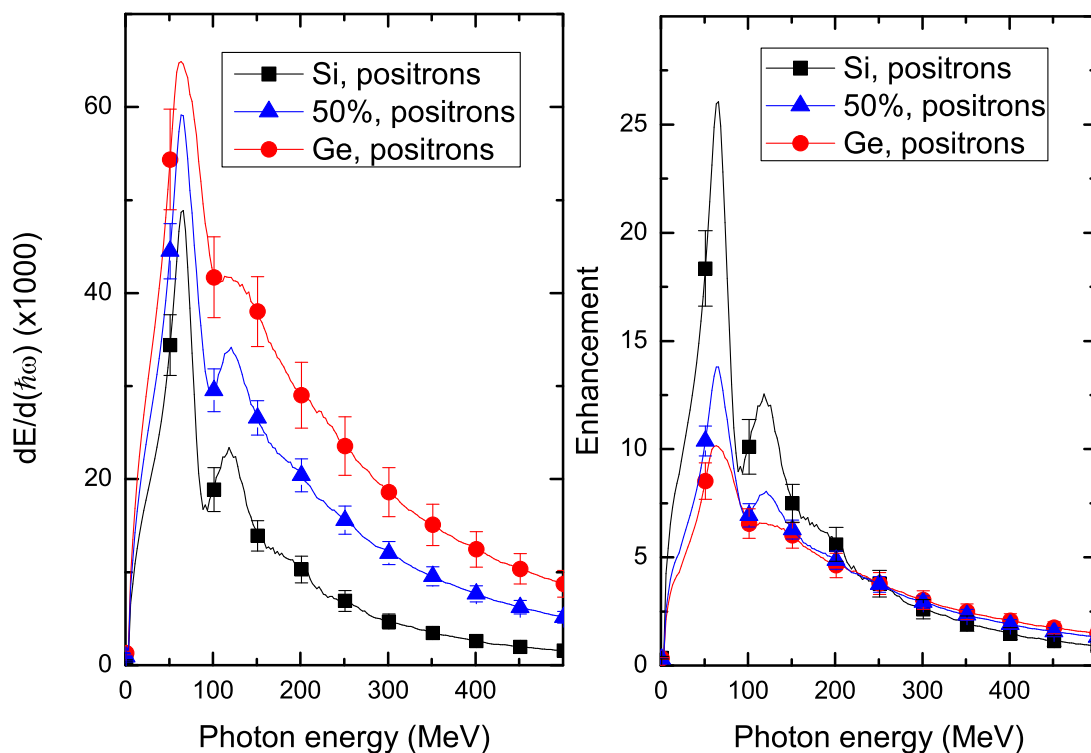


Figure 6.6: The radiation spectrum (left) and the radiation spectrum enhancement (right) of 10 GeV positrons channeling through $\text{Si}_{1-x}\text{Ge}_x$ crystals with different concentration of Ge ($x \cdot 100\%$) in (110) direction. Crystal thickness is 100 μm , radiation aperture is 0.25 mrad ($4.9/\gamma$).

case of Ge, then in Si crystals, depending on the calculation method. The second additional factor to the change of intensity is the change of the photon energy at the maximum of intensity by 28%. This factor gives a major contribution because intensity is proportional to the fourth power of frequency:

$$I \propto \omega^4 L_c d^2 \quad (6.2)$$

where I is the intensity of the radiation, ω is the frequency, d is the interplanar distance, and L_c is the characteristic channeling length, which can be determined as the minimum of the dechanneling length L_d and the total thickness L of the crystal sample.

The change of the content of Ge leads also to the change of the radiation spectrum in amorphous medium. As a result the situation for the calculated radiation spectrum enhancement (right panels) looks rather different from the radiation spectrum itself. The highest enhancement can be observed for pure Si crystals, the lowest

is for pure Ge crystals, for intermediate concentrations the spectrum enhancement is between these two cases. The dependence of the enhancement of the concentration of doped atoms is nonlinear and even small percentage of Ge atoms leads to substantial drop of enhancement.

Chapter 7

Summary and conclusions

This work is devoted to the theoretical study of process of channeling and channeling radiation emission in oriented crystals. It is focused on the case of light projectiles (electrons and positrons) in the energy range between 0.3 and 20 GeV and uses an atomistic molecular dynamics approach for studying this process. The results of this study were published in several papers [45, 46, 44, 48, 47]. The validity of this approach was tested on several case studies and compared to the results of recent experimental measurements [11, 127] and theoretical methods [35, 40].

In the Chapter 2 it is shown that for this energy range the classical relativistic equations of motion can be used, and the radiation damping force can be omitted. In that chapter the overview of the quasi-classical formalism for calculation of radiation spectrum of emitted photons is outlined. The overview of existing theoretical methods of description of channeling and propagation in amorphous media is given.

The Chapter 3 introduces an atomistic molecular dynamics approach for studying channeling of charged particles in complex oriented crystals. This approach involves an integration mechanism, the algorithm of generation of the local crystalline medium representation, and the proper choice of the interaction potential of the projectile and the atoms of the medium. In this chapter the molecular dynamics many-body potential is described for simulation of the structure of Si-Ge crystals.

The Chapter 4 contains the results of the simulations of the propagation of electrons and positrons in amorphous medium and the process of planar and axial channeling in straight crystals. The results for amorphous medium case are compared with the analytic calculations using Bethe-Heitler approximation in Section 4.1. The results for planar channeling are compared with the results of experiments in terms

of dechanneling length and radiation spectrum in Section 4.2. The good agreement of the results of calculations obtained using the developed method with the results of experimental measurements shows, that it can be used for theoretical predictions.

The Chapter 5 contains results of the simulation of channeling in bent and periodically bent crystals. The results of these simulations are compared with recent experimental results for the case of uniformly bent crystals in Section 5.1 and for the periodically bent crystals with high period of bending in Section 5.2. The case of short-period periodic bending is studied numerically in Section 5.5. This chapter also contains the detailed study of the parameters of simulation on its results. The choice of the interaction potential is verified by the comparison of results for Moliere and Pacios potentials. It is shown that the results of simulations do not depend much on the selection between these interaction potentials.

The use of this approach allowed to study channeling in a complex case of binary Si-Ge crystals, and to obtain numerical characterization of influence of small concentrations of Ge on dechanneling length and radiation spectra of multi-GeV electrons. The Chapter 6 contains results of channeling simulations for this case and the study of the dependence of parameters of channeling and radiation emission of the concentration of Ge atoms.

The simulation of the propagation of projectiles with higher energy requires taking into account the effect of radiation damping. This is one of the directions of the further development of the model. As it was described in Section 2.1.2 this extension of the model is required for projectile with energy above 50 GeV.

Another topic of future work is the study of channeling in non-ideal crystals. The presence of defects in the crystalline structure leads to the decrease of effect of channeling. The use of atomistic approach allows direct modeling of defects in crystalline lattice and simulation of propagation of projectiles in such medium. This approach allows direct simulation of propagation of projectiles in Si-Ge superlattices with both constant and variable concentration of Ge atoms, and therefore can be used for simulation of channeling in periodically bent crystals taken into account their variable composition.

Another topic of future work is the study of channeling in nanostructured materials such as nanotubes and graphene. The use of these materials allows fine tuning of crystal properties such as potential energy well depth and interplanar distance. These materials can be applied for construction of radiation sources with specific properties of channeling and undulator radiation.

Chapter 8

Acknowledgments

The research on which this dissertation reports has been conducted during the years 2012 to 2015 while employed at the Frankfurt Institute for Advanced Studies (FIAS), Johann Wolfgang Goethe University. First I would like to thank my scientific advisers Prof. Dr. Andrey V. Solov'yov and Prof. Dr. Stefan Schramm who has guided my scientific work at FIAS and who have set interesting scientific goals for my study. I would also like to thank my colleague Prof. Dr. Andrei Korol for his help in the scientific work and proofreading of this manuscript. I would also like Christian Kexel and Alexey Verkhovtsev for proofreading the Kurzfassung and Zusammenfassung.

I would like to thank my colleagues Dr. Viktor Beschastnov, Dr. Alexander Yakubovich, Alexey Verkhovtsev, Prof. Dr. Vadim Ivanov and Dr. Roman Polozkov with whom I have published several works on channeling and also on studies of properties of titanium and nickel-titanium alloys.

I am very grateful to professors and lecturers of the Moscow Institute of Physics and Technology who were teaching me physics, maths and programming during my undergraduate study. I would like to thank professors Vasily Kondourov, Andrey Aksenov and Sergey Kharchenko who were my scientific advisers in that period and who have introduced me to the application of numerical methods and high performance computing to the problems of physics of rigid bodies and fluids.

My work in Frankfurt was supported by the European Commission CUTE (the CUTE-IRSES project, grant GA-2010-269131), FP7 European Program "Theoretical analysis, design and virtual testing of biocompatibility and mechanical properties of titanium-based nanomaterials (ViNaT)" and COST Action MP1002 "Nano-scale

Insights into Ion Beam Cancer Therapy”. The possibility to perform complex computer simulations at the Frankfurt Center for Scientific Computing is gratefully acknowledged.

Most importantly, I would like to thank my family for supporting me in this work. Especially I want to mention my parents Elena and Boris, my wife Anastasia, my son Ivan and my brother Vladimir.

Bibliography

- [1] J. Lindhard, "Influence of crystal lattice on motion of energetic charged particles," *K. Dan. Vidensk. Selsk. Mat. Fys. Medd.*, vol. 34, pp. 1–64, 1965.
- [2] D. S. Gemmel, "Channeling and related effects in the motion of charged particles through crystals," *Reviews of Modern Physics*, vol. 46, pp. 129–227, 1974.
- [3] G. Piercy, F. Brown, J. Davies, and M. McCargo, "Experimental evidence for the increase of heavy ion ranges by channeling in crystalline structure," *Physical Review Letters*, vol. 10, 1963.
- [4] S. Andersen, O. Fich, H. Nielsen, H. E. Schiøtt, E. Uggerhøj, C. V. Thomsen, G. Charpak, G. Petersen, F. Sauli, J. Ponpon, *et al.*, "Influence of channeling on scattering of 2–15 gev/c protons, π^+ , and π^- incident on si and ge crystals," *Nuclear Physics B*, vol. 167, no. 1, pp. 1–40, 1980.
- [5] J. Bak, J. A. Ellison, B. Marsh, F. E. Meyer, O. Pedersen, J. B. B. Petersen, E. Uggerhøj, S. P. Møller, H. Sørensen, and M. Suffert, "Channeling radiation from 2 to 20 gev/c electrons and positrons: (II) axial case," *Nucl. Phys. B.*, vol. 302, pp. 525–558, 1988.
- [6] B. Appleton, C. Erginsoy, and W. Gibson, "Channeling effects in the energy loss of 3-11-mev protons in silicon and germanium single crystals," *Physical Review*, vol. 161, no. 2, p. 330, 1967.
- [7] J. Davies, J. Denhartog, and J. Whitton, "Channeling of mev projectiles in tungsten and silicon," *Physical Review*, vol. 165, no. 2, p. 345, 1968.
- [8] J. Bak, J. A. Ellison, B. Marsh, F. E. Meyer, O. Pedersen, J. B. B. Petersen, E. Uggerhøj, and K. Østergaard, "Channeling radiation from 2-55 gev/c elec-

- trons and positrons: (I) planar case,” *Nucl. Phys. B.*, vol. 254, pp. 491–527, 1985.
- [9] R. Medenwaldt, S. Møller, S. Tang-Petersen, E. Uggerhøj, K. Elsener, M. Hage-Ali, P. Siffert, J. Stoquert, P. Sona, and K. Maier, “Hard photon yields from (70–240) gev electrons incident near axial directions on si, ge and w single crystals with a large thickness variation,” *Physics Letters B*, vol. 242, no. 3, pp. 517–522, 1990.
- [10] J. Watson and J. Koehler, “Coherent bremsstrahlung and channeling radiation from mev electrons in silicon and gold,” *Physical Review A*, vol. 24, no. 2, p. 861, 1981.
- [11] U. Wienands, T. Markiewicz, J. Nelson, R. Noble, J. Turner, U. Uggerhøj, T. Wistisen, E. Bagli, L. Bandiera, G. Germogli, *et al.*, “Observation of a remarkable deflection of multi-gev electron beams by a thin crystal,” tech. rep., SLAC National Accelerator Laboratory (SLAC), 2014.
- [12] E. Bøgh, “Defect studies in crystals by means of channeling,” *Canadian Journal of Physics*, vol. 46, no. 6, pp. 653–662, 1968.
- [13] L. C. Feldman, J. W. Mayer, and S. T. Picraux, *Materials analysis by ion channeling: submicron crystallography*. Academic Press, 2012.
- [14] M. Kumakhov, “Theory of radiation of charged particles channeled in a crystal,” *physica status solidi (b)*, vol. 84, no. 1, pp. 41–54, 1977.
- [15] U. Uggerhøj and T. Wistisen, “Intense and energetic radiation from crystalline undulators,” *Nucl. Instrum. Methods B*, 2015.
- [16] L. Gevorgian, K. Ispirian, and R. Ispirian, “High energy particle channeling in nanotubes,” *Nucl. Instrum. Methods B*, vol. 145, no. 1, pp. 155–159, 1998.
- [17] S. Bellucci, V. Biryukov, Y. A. Chesnokov, V. Guidi, and W. Scandale, “Channeling of high energy beams in nanotubes,” *Nucl. Instrum. Methods B*, vol. 202, pp. 236–241, 2003.
- [18] X. Artru, S. Fomin, N. Shulga, K. Ispirian, and N. Zhevago, “Carbon nanotubes and fullerites in high-energy and x-ray physics,” *Physics reports*, vol. 412, no. 2, pp. 89–189, 2005.

- [19] A. V. Korol, A. V. Solov'yov, and W. Greiner, "Coherent radiation of an ultrarelativistic charged particle channeled in a periodically bent crystal," *J. Phys. B*, vol. 24, pp. L45–L53, 1998.
- [20] A. V. Korol, A. V. Solov'yov, and W. Greiner, "Photon emission by an ultrarelativistic particle channeling in a periodically bent crystal," *Int. J. Mod. Phys.*, vol. 8, pp. 49–100, 1999.
- [21] S. Bellucci, V. Biryukov, G. Britvich, Y. A. Chesnokov, C. Balasubramanian, G. Giannini, V. Guidi, Y. M. Ivanov, V. Kotov, V. Maisheev, *et al.*, "Crystal undulator as a new compact source of radiation," *Physical Review Special Topics-Accelerators and Beams*, vol. 7, no. 2, p. 023501, 2004.
- [22] V. T. Baranov, S. Bellucci, V. M. Biryukov, G. I. Britvich, C. Balasubramanian, V. Guidi, G. Giannini, V. N. Zapol'sky, V. I. Kotov, A. E. Kushnirenko, V. A. Maisheev, G. Martinelli, E. Milan, V. A. Pikalov, V. I. Terekhov, U. Uggerhøj, V. N. Chepegin, and Y. A. Chesnokov, "First results of investigation of radiation from positrons in a crystalline undulator," *JETP Letters*, vol. 82, pp. 562–564, 2005.
- [23] A. Afonin, V. Baranov, S. Bellucci, V. Biryukov, G. Britvich, V. Chepegin, Y. A. Chesnokov, C. Balasubramanian, G. Giannini, V. Guidi, *et al.*, "Crystal undulator experiment at ihep," *Nuclear Instruments and Methods in Physics Research Section B: Beam Interactions with Materials and Atoms*, vol. 234, no. 1, pp. 122–127, 2005.
- [24] V. T. Baranov, S. Bellucci, V. M. Biryukov, G. I. Britvich, V. N. Chepegin, Y. A. Chesnokov, C. Balasubramanian, G. Giannini, V. Guidi, V. I. Kotov, A. E. Kushnirenko, V. A. Maisheev, G. Martinelli, V. A. Pikalov, V. I. Terekhov, U. Uggerhøj, and V. N. Zapol'sky, "Preliminary results on the study of radiation from positrons in a periodically deformed crystal," *Nucl. Instrum. Methods B*, vol. 252, pp. 32–35, 2006.
- [25] H. Backe, D. Krambrich, W. Lauth, K. Andersen, J. L. Hansen, and U. I. Uggerhøj, "Channeling and radiation of electrons in silicon single crystals and $\text{Si}_1\text{-xGe}_x$ crystalline undulators," in *Journal of Physics: Conference Series*, vol. 438, p. 012017, IOP Publishing, 2013.

-
- [26] E. Bagli, L. Bandiera, V. Bellucci, A. Berra, R. Camattari, D. De Salvador, G. Germogli, V. Guidi, L. Lanzoni, D. Lietti, *et al.*, “Experimental evidence of planar channeling in a periodically bent crystal,” *The European Physical Journal C*, vol. 74, no. 10, pp. 1–7, 2014.
- [27] T. N. Wistisen, K. K. Andersen, S. Yilmaz, R. Mikkelsen, J. L. Hansen, U. I. Uggerhøj, W. Lauth, and H. Backe, “Experimental realization of a new type of crystalline undulator,” *Physical review letters*, vol. 112, no. 25, p. 254801, 2014.
- [28] U. Mikkelsen and E. Uggerhøj, “A crystalline undulator based on graded composition strained layers in a superlattice,” *Nucl. Instrum. Methods B*, vol. 160, pp. 435–439, 2000.
- [29] W. Krause, A. V. Korol, A. Solov’yov, and W. Greiner, “Photon emission by relativistic positrons in crystalline undulators: the high-energy regime,” *Nucl. Instrum. Methods A*, vol. 483, pp. 455–460, 2002.
- [30] M. Tabrizi, A. V. Korol, A. V. Solov’yov, and W. Greiner, “Feasibility of an electron-based crystalline undulator,” *Physical Review Letters*, vol. 98, p. 164801, 2007.
- [31] V. Baryshevsky and V. Tikhomirov, “Crystal undulators: from the prediction to the mature simulations,” *Nucl. Instrum. Methods B*, vol. 309, pp. 30–36, 2013.
- [32] A. V. Korol, A. V. Solov’yov, and W. Greiner, *Channeling and Radiation in Periodically Bent Crystals*. Springer-Verlag Berlin Heidelberg, 2013.
- [33] A. Kostyuk, “Crystalline undulator with a small amplitude and a short period,” *Physical Review Letters*, vol. 110, no. 11, p. 115503, 2013.
- [34] V. G. Bezchastnov, A. V. Korol, and A. V. Solovyov, “Radiation from multi-gev electrons and positrons in periodically bent silicon crystal,” *Journal of Physics B: Atomic, Molecular and Optical Physics*, vol. 47, no. 19, p. 195401, 2014.
- [35] V. V. Tikhomirov, “A benchmark construction of positron crystal undulator,” *arXiv preprint arXiv:1502.06588*, 2015.

-
- [36] O. Bogdanov, E. Fiks, K. Korotchenko, Y. Pivovarov, and T. Tukhfatullin, “Basic channeling with mathematica[©]: A new computer code,” *J. Phys.: Conf. Ser.*, vol. 236, p. 012029, 2010.
- [37] V. M. Biryukov, “Computer simulation of beam steering by crystal channeling,” *Physical Review E*, vol. 51, pp. 3522–3528, 1995.
- [38] V. A. Maishev, “Model-independent description of planar channeling at high energies,” *Nucl. Instrum. Methods B*, vol. 119, pp. 42–47, 1996.
- [39] J. H. Barrett, “Monte carlo channeling calculations,” *Physical Review B*, vol. 3, no. 5, p. 1527, 1971.
- [40] E. Bagli and V. Guidi, “Dynecharm++: a toolkit to simulate coherent interactions of high-energy charged particles in complex structures,” *Nucl. Instrum. Methods B*, vol. 309, pp. 124–129, 2013.
- [41] P. S. D. Boerma, “Computer simulation of channeling in single crystals,” *Nucl. Instrum. Methods B*, vol. 29, pp. 471–489, 1987.
- [42] S. Fomin, A. Jejcic, V. Kasilov, N. Lapin, J. Maillard, V. Noga, S. Shcherbak, N. Shul’ga, and J. Silva, “Investigation of the electron channeling by means of induced electronuclear reactions,” *Nucl. Instrum. Methods B*, vol. 129, pp. 29–34, 1997.
- [43] N. Shul’ga and V. Syshchenko, “Investigation of the electron channeling by means of induced electronuclear reactions,” *Nucl. Instrum. Methods B*, vol. 227, p. 125131, 2005.
- [44] G. B. Sushko, V. G. Bezchastnov, I. A. Solovyov, A. V. Korol, W. Greiner, and A. V. Solovyov, “Simulation of ultra-relativistic electrons and positrons channeling in crystals with mbn explorer,” *Journal of Computational Physics*, vol. 252, pp. 404–418, 2013.
- [45] G. Sushko, V. Bezchastnov, A. Korol, W. Greiner, A. Solov’yov, R. Polozkov, and V. Ivanov, “Simulations of electron channeling in bent silicon crystal,” *Journal of Physics: Conference Series*, vol. 438, no. 1, p. 012019, 2013.

- [46] G. Sushko, A. Korol, W. Greiner, and A. Solov'yov, "Sub-gev electron and positron channeling in straight, bent and periodically bent silicon crystals," *Journal of Physics: Conference Series*, vol. 438, no. 1, p. 012018, 2013.
- [47] G. B. Sushko, A. V. Korol, and A. V. Solovyov, "Multi-gev electron and positron channeling in bent silicon crystals," *Nucl. Instrum. Methods B*, vol. 355, no. 0, pp. 39 – 43, 2015.
- [48] R. Polozkov, V. Ivanov, G. Sushko, A. V. Korol, and A. V. Solov'yov, "Radiation emission by electrons channeling in bent silicon crystals," *European Physical Journal D*, vol. 68, no. 9, p. 268, 2014.
- [49] G. Molière, "Theorie der streuung schneller geladener teilchen I: Einzelstreuung am abgeschirmten coulomb-feld," *Z. f. Naturforsch. A*, vol. 2, pp. 133–145, 1947.
- [50] L. F. Pacios, "Analytical density-dependent representation of hartree-fock atomic potentials," *J. Comp. Chem.*, vol. 14, pp. 410–421, 1993.
- [51] I. A. Solov'yov, A. V. Yakubovich, P. V. Nikolaev, I. Volkovets, and A. V. Solov'yov, "Mesobionano explorer – a universal program for multiscale computer simulations of complex molecular structure and dynamics," *J. Comp. Chem.*, vol. 33, pp. 2412–2439, 2012.
- [52] <http://www.mbnexplorer.com/>, 2012.
- [53] W. G. A.V. Korol, A.V. Solov'yov, *Channeling and Radiation in Periodically Bent Crystals. 2nd Edition*. Springer Berlin/Heidelberg, 2014.
- [54] H. Backe, D. Krambrich, W. Lauth, J. L. Hansen, and U. K. I. Uggerhøj, "X-ray emission from a crystal undulator: Experimental results at channeling of electrons," *Nuovo Cimento C*, vol. 34, pp. 157–165, 2011.
- [55] A. Korol, A. Solov'yov, and W. Greiner, "Estimation of peak brilliance for a crysalline undulator laser," tech. rep., 2012.
- [56] G. C. Andonian, *Experimental and Analytical Study of a High Gain Self Amplified Spontaneous Emission Free Electron Laser Operating in a Large Spectral Bandwidth Regime*. PhD thesis, University of California Los Angeles, 2006.

-
- [57] F. Stillinger and T. Weber, “New interatomic potential for silicon,” *Physical Review B*, vol. 31, pp. 5262–5267, 1984.
- [58] H. Bethe and W. Heitler, “On the stopping of fast particles and on the creation of positive electrons,” *Proc. Roy. Soc. London. Series A*, vol. 146, pp. 83–112, 1934.
- [59] H. A. Bethe and L. C. Maximon, “Theory of bremsstrahlung and pair production. I. Differential cross section,” *Physical Review*, vol. 93, pp. 768–784, 1954.
- [60] H. Davis, H. A. Bethe, and L. C. Maximon, “Theory of bremsstrahlung and pair production. II. Integral cross section for pair production,” *Physical Review*, vol. 93, pp. 788–795, 1954.
- [61] U. Wienands, T. Markiewicz, J. Nelson, R. Noble, J. Turner, U. Uggerhøj, T. Wistisen, E. Bagli, L. Bandiera, G. Germogli, *et al.*, “Observation of a remarkable deflection of multi-gev electron beams by a thin crystal,” *SLAC Scientific Publications*, 2014.
- [62] G. B. Sushko, A. V. Korol, and A. V. Solovyov, “Electron and positron propagation in straight and periodically bent axial and planar si channels,” *St. Petersburg State Polytechnical University Journal*, 2015.
- [63] G. B. Sushko, A. V. Korol, and A. V. Solovyov, “Simulation of 20 gev electron and positron -based small-amplitude short-period crystalline undulator,” *St. Petersburg State Polytechnical University Journal*, 2015.
- [64] R. Brinkmann, G. Mateerlik, J. Rossbach, J. Schneider, and B. Wiik, “An x-ray fel laboratory as part of a linear collider design,” tech. rep., Deutsches Elektronen-Synchrotron DESY, 1996.
- [65] A. Korol, A. Solov’yov, and W. Greiner, “Number of photons and brilliance of the radiation from a crystalline undulator,” in *International Conference on Charged and Neutral Particles Channeling Phenomena*, pp. 597405–597405, International Society for Optics and Photonics, 2005.
- [66] M. Dohlus, J. Rossbach, and P. Schmüser, “Ultraviolet and soft x-ray free-electron lasers,” 2008.

- [67] V. B. Berestetskii, E. M. Lifshitz, and L. P. Pitaevskii, *Course of Theoretical Physics, vol.4. Quantum Electrodynamics*. Pergamon Press, Oxford, 1982.
- [68] L. V. Hau and J. U. Andersen, “Channeling radiation beyond the continuum model: The phonon “lamb shift” and higher-order corrections,” *Physical Review A*, vol. 47, pp. 4007–4032, May 1993.
- [69] M. A. Kumakhov, *Radiation from Channeling Particles in Crystals*. Energoatomizdat, Moscow, 1986.
- [70] L. D. Landau and E. M. Lifshitz, *Course of Theoretical Physics, vol.2. The Classical Theory of Fields*. Pergamon Press, Oxford, 1971.
- [71] J. Larmor, “Lxiii. on the theory of the magnetic influence on spectra; and on the radiation from moving ions,” *The London, Edinburgh, and Dublin Philosophical Magazine and Journal of Science*, vol. 44, no. 271, pp. 503–512, 1897.
- [72] O. Heaviside, “Waste of energy from a moving electron,” *Nature*, vol. 67, p. 32, 1902.
- [73] M. Abraham, “Prinzipien der dynamik des elektrons,” *Annalen der Physik*, vol. 315, no. 1, pp. 105–179, 1902.
- [74] F. Rohrlich, “The dynamics of a charged sphere and the electron,” *American Journal of Physics*, vol. 65, no. 11, pp. 1051–1056, 1997.
- [75] I. Y. Pomeranchuk, “Maximum energy that primary cosmic-ray electrons can acquire on the surface of the earth as a result of radiation in the earths magnetic field. jetp, 1939, v. 9, 915,” *J. Phys. USSR*, vol. 2, p. 65, 1940.
- [76] A. Di Piazza, T. N. Wistisen, and U. I. Uggerhøj, “Investigation of classical radiation reaction with aligned crystals,” *arXiv preprint arXiv:1503.05717*, 2015.
- [77] F. Rohrlich, “Dynamics of a charged particle,” *Physical Review E*, vol. 77, no. 4, p. 046609, 2008.
- [78] V. N. Baier, V. M. Katkov, and V. M. Strakhovenko, *Electromagnetic Processes at High Energies in Oriented Single Crystals*. World Scientific, Singapore, 1998.

- [79] V. N. Baier and V. M. Katkov, “Processes involved in the motion of high energy particles in magnetic field,” *Zh. Eksp. Teor. Fiz.*, vol. 53, pp. 1478–1491, 1967.
- [80] Y.-S. Tsai, “Pair production and bremsstrahlung of charged leptons,” *Reviews of Modern Physics*, vol. 46, pp. 815–851, 1974.
- [81] A. I. Akhiezer and V. B. Berestetsky, *Quantum Electrodynamics*. Interscience Publishers, New York, 1965.
- [82] K. Nakamura *et al.*, “Review of particle physics,” *J. Phys. G: Nucl. Part. Phys.*, vol. 37, p. 075021, 2010.
- [83] C. Kittel, P. McEuen, and P. McEuen, *Introduction to solid state physics*, vol. 8. Wiley New York, 1976.
- [84] S. Flugge, *Practical quantum mechanics*, vol. 1. Springer Berlin, 1971.
- [85] A. Taratin, “Particle channeling in a bent crystal,” *Physics of Particles and Nuclei*, vol. 29, no. 5, pp. 437–462, 1998.
- [86] W. Scandale, R. Losito, E. Bagli, L. Bandiera, P. Dalpiaz, M. Fiorini, V. Guidi, A. Mazzolari, D. Vincenzi, G. Della Mea, *et al.*, “Measurement of the dechanneling length for high-energy negative pions,” *Physics Letters B*, vol. 719, no. 1, pp. 70–73, 2013.
- [87] A. Mazzolari, E. Bagli, L. Bandiera, V. Guidi, H. Backe, W. Lauth, V. Tikhomirov, A. Berra, D. Lietti, M. Prest, *et al.*, “Steering of a sub-gev electron beam through planar channeling enhanced by rechanneling,” *Physical Review Letters*, vol. 112, no. 13, p. 135503, 2014.
- [88] A. I. Sytov and V. V. Tikhomirov, “Crystal simulation code and new coherent effects in bent crystal at the lhc,” *arXiv preprint arXiv:1412.0110*, 2014.
- [89] W. Scandale, G. Arduini, M. Butcher, F. Cerutti, M. Garattini, S. Gilardoni, L. Lari, A. Lechner, R. Losito, A. Masi, *et al.*, “Observation of nuclear dechanneling length reduction for high energy protons in a short bent crystal,” *Physics letters B*, vol. 743, pp. 440–443, 2015.

- [90] E. Bagli, M. Asai, D. Brandt, A. Dotti, V. Guidi, and D. Wright, “A model for the interaction of high-energy particles in straight and bent crystals implemented in geant4,” *The European Physical Journal C*, vol. 74, no. 8, pp. 1–11, 2014.
- [91] Y. M. Ivanov, A. Petrunin, and V. V. Skorobogatov, “Observation of the elastic quasi-mosaicity effect in bent silicon single crystals,” *Journal of Experimental and Theoretical Physics Letters*, vol. 81, no. 3, pp. 99–101, 2005.
- [92] V. Guidi, A. Mazzolari, D. De Salvador, and A. Carnera, “Silicon crystal for channelling of negatively charged particles,” *Journal of Physics D: Applied Physics*, vol. 42, no. 18, p. 182005, 2009.
- [93] G. Germogli, A. Mazzolari, L. Bandiera, E. Bagli, and V. Guidi, “Manufacturing and characterization of bent silicon crystals for studies of coherent interactions with negatively charged particles beams,” *Nucl. Instrum. Methods B*, 2015.
- [94] A. Kostyuk, A. Korol, A. Solovyov, and W. Greiner, “The influence of the structure imperfectness of a crystalline undulator on the emission spectrum,” *Nuclear Instruments and Methods in Physics Research Section B: Beam Interactions with Materials and Atoms*, vol. 266, no. 6, pp. 972–987, 2008.
- [95] P. Balling, J. Esberg, K. Kirsebom, D. Q. S. Le, U. I. Uggerhøj, S. Connell, J. Härtwig, F. Masiello, and A. Rommeveaux, “Bending diamonds by femtosecond laser ablation,” *Nuclear Instruments and Methods in Physics Research Section B: Beam Interactions with Materials and Atoms*, vol. 267, no. 17, pp. 2952–2957, 2009.
- [96] S. Bellucci, S. Bini, V. Biryukov, Y. A. Chesnokov, S. Dabagov, G. Giannini, V. Guidi, Y. M. Ivanov, V. Kotov, V. Maishev, *et al.*, “Experimental study for the feasibility of a crystalline undulator,” *Physical review letters*, vol. 90, no. 3, p. 034801, 2003.
- [97] V. Baranov, S. Bellucci, V. Biryukov, G. Britvich, V. Chepegin, Y. A. Chesnokov, C. Balasubramanian, G. Giannini, V. Guidi, V. Kotov, *et al.*, “Preliminary results on the study of radiation from positrons in a periodically deformed

- crystal,” *Nuclear Instruments and Methods in Physics Research Section B: Beam Interactions with Materials and Atoms*, vol. 252, no. 1, pp. 32–35, 2006.
- [98] V. Guidi, L. Lanzoni, A. Mazzolari, G. Martinelli, and A. Tralli, “Design of a crystalline undulator based on patterning by tensile Si_3N_4 strips on a Si crystal,” *Applied physics letters*, vol. 90, no. 11, p. 114107, 2007.
- [99] V. Guidi, A. Antonini, S. Baricordi, F. Logallo, C. Malagù, E. Milan, A. Ronzoni, M. Stefancich, G. Martinelli, and A. Vomiero, “Tailoring of silicon crystals for relativistic-particle channeling,” *Nuclear Instruments and Methods in Physics Research Section B: Beam Interactions with Materials and Atoms*, vol. 234, no. 1, pp. 40–46, 2005.
- [100] U. Mikkelsen and E. Uggerhøj, “A crystalline undulator based on graded composition strained layers in a superlattice,” *Nuclear Instruments and Methods in Physics Research Section B: Beam Interactions with Materials and Atoms*, vol. 160, no. 3, pp. 435–439, 2000.
- [101] M. Breese, “Beam bending using graded composition strained layers,” *Nuclear Instruments and Methods in Physics Research Section B: Beam Interactions with Materials and Atoms*, vol. 132, no. 3, pp. 540–547, 1997.
- [102] W. Krause, A. V. Korol, A. V. Solov’yov, and W. Greiner, “Photon emission by ultra-relativistic positrons in crystalline undulators: the high-energy regime,” *Nuclear Instruments and Methods in Physics Research Section A: Accelerators, Spectrometers, Detectors and Associated Equipment*, vol. 483, no. 1, pp. 455–460, 2002.
- [103] V. Baryshevsky, I. Y. Dubovskaya, and A. Grubich, “Generation of γ -quanta by channeled particles in the presence of a variable external field,” *Physics Letters A*, vol. 77, no. 1, pp. 61–64, 1980.
- [104] O. Bogdanov, E. Fiks, K. Korotchenko, Y. L. Pivovarov, and T. Tukhfatullin, “Basic channeling with mathematica©: A new computer code,” in *Journal of Physics: Conference Series*, vol. 236, p. 012029, IOP Publishing, 2010.
- [105] E. Bagli, V. Guidi, and V. A. Maishev, “Calculation of the potential for interaction of particles with complex atomic structures,” *Physical Review E*, vol. 81, p. 026708, Feb 2010.

- [106] L. Bandiera, E. Bagli, V. Guidi, and V. V. Tikhomirov, “Radcharm++: A c++ routine to compute the electromagnetic radiation generated by relativistic charged particles in crystals and complex structures,” *Nucl. Instrum. Methods B*, 2015.
- [107] S. Agostinelli, J. Allison, K. a. Amako, J. Apostolakis, H. Araujo, P. Arce, M. Asai, D. Axen, S. Banerjee, G. Barrand, *et al.*, “Geant4a simulation toolkit,” *Nuclear instruments and methods in physics research section A: Accelerators, Spectrometers, Detectors and Associated Equipment*, vol. 506, no. 3, pp. 250–303, 2003.
- [108] J. Allison, K. Amako, J. Apostolakis, H. Araujo, P. A. Dubois, M. Asai, G. Barrand, R. Capra, S. Chauvie, R. Chytracsek, *et al.*, “Geant4 developments and applications,” *Nuclear Science, IEEE Transactions on*, vol. 53, no. 1, pp. 270–278, 2006.
- [109] A. Kostyuk, A. Korol, A. Solovyov, and W. Greiner, “Planar channelling of 855 mev electrons in silicon: Monte carlo simulations,” *Journal of Physics B: Atomic, Molecular and Optical Physics*, vol. 44, no. 7, p. 075208, 2011.
- [110] W. H. Press, B. P. Flannery, S. A. Teukolsky, and W. T. Vetterling, *Numerical Recipes. The Art of Scientific Computing*. University Press, Cambridge, 1988.
- [111] J. Tersoff, “New empirical approach for the structure and energy of covalent systems,” *Physical Review B*, vol. 37, no. 12, pp. 6991–7000, 1988.
- [112] J. Tersoff, “Empirical interatomic potential for carbon, with applications to amorphous carbon,” *Physical Review Letters*, vol. 61, no. 25, pp. 2879–2882, 1988.
- [113] D. W. Brenner, “Empirical potential for hydrocarbons for use in simulating the chemical vapor deposition of diamond films,” *Physical Review B*, vol. 42, pp. 9458–9471, 1990.
- [114] Ş. Erkoç, “Empirical many-body potential energy functions used in computer simulations of condensed matter properties,” *Physics Reports*, vol. 278, no. 2, pp. 79–105, 1997.

- [115] S. Ethier and L. J. Lewis, “Epitaxial growth of Si_3N_4 on $\text{Si}(100) 2 \times 1$: A molecular-dynamics study,” *Journal of materials research*, vol. 7, no. 10, pp. 2817–2827, 1992.
- [116] R. V. Hogg, J. McKean, and A. T. Craig, *Introduction to mathematical statistics*. Pearson Education, 2005.
- [117] V. M. Biryukov, Y. A. Chesnokov, and V. I. Kotov, *Crystal Channeling and its Application at High-Energy Accelerators*. Springer, Berlin, Heidelberg, 1996.
- [118] A. V. Korol, A. V. Solov’yov, and W. Greiner, “The influence of the dechanneling process on the photon emission by an ultra-relativistic positron channeling in a periodically bent crystal,” *J. Phys. G: Nucl. Part. Phys.*, vol. 27, pp. 95–125, 2001.
- [119] A. Kostyuk, A. V. Korol, A. V. Solov’yov, and W. Greiner, “Planar channeling of 855 meV electrons in silicon: Monte carlo simulations,” *J. Phys. B: At. Mol. Opt. Phys.*, vol. 44, p. 075208, 2011.
- [120] H. Backe, P. Kunz, W. Lauth, and A. Rueda, “Planar channeling experiments with electrons at the 855-MeV mainz microtron,” *Nucl. Instrum. Methods B*, vol. 266, pp. 3835–3851, 2008.
- [121] E. Uggerhøj, “Some recent experimental investigations of photon emission and shower formation in strong crystalline fields,” *Rad. Eff. Def. Solids*, vol. 25, pp. 3–21, 1993.
- [122] P. A. Doyle and P. S. Turner, “Relativistic hartree-fock x-ray and electron scattering factor,” *Acta Crystallogr. A*, vol. 24, pp. 390–397, 1968.
- [123] K. Chouffani and H. Überall, “Theory of low energy channeling radiation: Application to a germanium crystal,” *Physica Status Solidi (b)*, vol. 213, pp. 107–151, 1999.
- [124] E. N. Tsyganov, “(a) some aspects of the mechanism of a charge particle penetration through a monocrystal. (b) estimates of cooling and bending processes for charged particle penetration through a monocrystal,” *Fermilab Preprint*, vol. TM-682, TM-684, 2005.

-
- [125] W. Scandale, R. Losito, E. Bagli, L. Bandiera, P. Dalpiaz, M. Fiorini, V. Guidi, A. Mazzolari, D. Vincenzi, G. Della Mea, *et al.*, “Measurement of the dechanneling length for high-energy negative pions,” *Physics Letters B*, vol. 719, no. 1, pp. 70–73, 2013.
- [126] T. Waho, “Planar dechanneling of protons in si and ge,” *Physical Review B*, vol. 14, no. 11, p. 4830, 1976.
- [127] U. Wienands, W. Markiewicz, T. J. Nelson, J. Noble, R. L. Turner, J. I. Uggerhøj, U. N. Wistisen, T. E. Bagli, L. Bandiera, G. Germogli, V. Guidi, A. Mazzolari, R. Holtzapple, and M. Miller, “Observation of deflection of a beam of multi-gev electrons by a thin crystal,” *Physical Review Letters*, vol. 114, p. 074801, Feb 2015.
- [128] M. Tabrizi, A. V. Korol, A. V. Solov’yov, and W. Greiner, “An electron-based crystalline undulator,” *Journal of Physics G: Nuclear and Particle Physics*, vol. 34, no. 7, p. 1581, 2007.
- [129] E. Bagli, M. Asai, A. Dotti, V. Guidi, and M. Verderi, “Channeling efficiency dependence on bending radius and thermal vibration amplitude of the model for the channeling of high-energy particles in straight and bent crystals implemented in geant4,” *Nucl. Instrum. Methods B*, 2015.
- [130] H. Backe, W. Lauth, P. Kunz, A. Rueda, J. Esberg, K. Kirsebom, J. L. Hansen, and U. K. I. Uggerhøj, *Charged and Neutral Particles Channeling Phenomena – Channeling 2008*, ch. Photon Emission of Electrons in a Crystalline Undulator, pp. 281–290. Singapore, World Scientific, 2010.
- [131] L. Verlet, “Computer experiments on classical fluids,” *Physical Review*, vol. 159, p. 98103, 1967.
- [132] D. Levesque and L. Verlet, “Molecular-dynamics and time reversibility,” *J. Stat. Phys.*, vol. 72, pp. 519–537, 1993.

Biography (Lebenslauf)



Name: Gennady Sushko

Date of Birth: 06.06.1986

Business Address: Frankfurt Institute for Advanced Studies, Johann Wolfgang Goethe University, Ruth-Moufang-Str. 1, 60438 Frankfurt am Main, Germany

Work Phone: +49-069-798-47534

Mobile Phone: +49-151-267-39732

E-mail: gennady.sushko@gmail.com

Education:

9/2012 – present: Johann Wolfgang Goethe University, Frankfurt Institute for Advanced Studies (Frankfurt, Germany) PhD student in physics. Studying molecular dynamics, numerical methods.

7/2007 – 7/2009: Moscow Institute of Physics and Technology (Moscow, Russia)
M.S., in Applied Physics and Mathematics. Studied a wide range of courses related to computer science, numerical methods in math and physics. Master thesis: Application of hybrid parallelism model to calculation of computational fluid dynamics problems.

7/2003 – 7/2007: Moscow Institute of Physics and Technology (Moscow, Russia)
B.S., in Applied Physics and Mathematics

Work Experience:

8/2007 – 06/2012: TESIS, Moscow, The Group of Computational Fluid Dynamics. Software Engineer

List of Publications

1. G.B. Sushko, A.V. Korol, A.V. Solovyov "Electron and positron propagation in straight and periodically bent axial and planar Si channels" St. Petersburg State Polytechnical University Journal, in print
2. G.B. Sushko, A.V. Korol, A.V. Solovyov "Simulation of 20 GeV electron and positron -based small-amplitude short-period crystalline undulator" St. Petersburg State Polytechnical University Journal, in print
3. I.A. Solovyov, G.B. Sushko, A.V. Verkhovtsev, A.V. Korol, A.V. Solovyov, MBN Explorer: simulations of nanomaterials structure and dynamics, Polytechnic University Publishing House, St. Petersburg State Polytechnic University, St. Petersburg (2015), p.1-102; ISBN 978-5-7422-4893-4
4. I.A. Solovyov, G.B. Sushko, A.V. Verkhovtsev, A.V. Korol, A.V. Solovyov, MBN Explorer: dynamics of biomolecular systems and self-organization, Polytechnic University Publishing House, St. Petersburg State Polytechnic University, St. Petersburg (2015), p.1-112; ISBN 978-5-7422-4894-1
5. G.B. Sushko, A.V. Korol, A.V. Solovyov "Multi-GeV electron and positron channeling in bent silicon crystals" Nuclear Instruments and Methods in Physics Research Section B 355, 39-43 (2015)
6. B.P. Marinković, V. Vujčić, G.B. Sushko, D. Vudragović, D.B. Marinković, et al. "Development of collisional data base for elementary processes of electron scattering by atoms and molecules" Nuclear Instruments and Methods in Physics Research Section B 354, 90-95 (2015)
7. R.G. Polozkov, V.K. Ivanov, G.B. Sushko, A.V. Korol, A.V. Solov'yov "Radiation Emission by Electrons Channeling in Bent Silicon Crystals" European Physical Journal D 68 (9), 268 (2014)

8. G.B. Sushko, A.V. Verkhovtsev, A.V. Solov'yov "Validation of Classical Force Fields for the Description of Thermo-Mechanical Properties of Transition Metal Materials" *J. Phys. Chem. A*, 2014, 118 (37), pp 8426-8436
9. G.B. Sushko, A.V. Verkhovtsev, A.V. Yakubovich, S. Schramm, A.V. Solov'yov "Molecular Dynamics Simulation of Self-Diffusion Processes in Titanium in Bulk Material, on Grain Junctions and on Surface" *The Journal of Physical Chemistry A* 118 (33), 6685-6691 (2014)
10. A.V. Verkhovtsev, A.V. Yakubovich, G.B. Sushko, M. Hanauske, A.V. Solov'yov "Molecular dynamics simulations of the nanoindentation process of titanium crystal" *Computational Materials Science* 76, 20-26 (2013)
11. G.B. Sushko, V.G. Bezchastnov, A.V. Korol, W. Greiner, A.V. Solov'yov, R.G. Polozkov, V.K. Ivanov "Simulations of electron channeling in bent silicon crystal" *Journal of Physics: Conference Series* 438 (1), 012019 (2013)
12. G.B. Sushko, A.V. Korol, W. Greiner, A.V. Solov'yov "Sub-GeV Electron and Positron Channeling in Straight, Bent and Periodically Bent Silicon Crystals" *Journal of Physics: Conference Series* 438 (1), 012018 (2013)
13. G.B. Sushko, A.V. Verkhovtsev, A.V. Yakubovich, A.V. Solov'yov "Molecular dynamics simulation of nanoindentation of nickel-titanium crystal" *Journal of Physics: Conference Series* 438 (1), 012021 (2013)
14. G.B. Sushko, V.G. Bezchastnov, I.A. Solovyov, A.V. Korol, W. Greiner, A.V. Solov'yov "Simulation of ultra-relativistic electrons and positrons channeling in crystals with MBN Explorer" *Journal of Computational Physics* 252, 404-418 (2013)
15. A.V. Verkhovtsev, G.B. Sushko, A.V. Yakubovich, A.V. Solov'yov "Benchmarking of classical force fields by ab initio calculations of atomic clusters: Ti and Ni-Ti case" *Computational and Theoretical Chemistry*, Volume 1021, 1 October 2013, Pages 101108 (2013)
16. A.V. Yakubovich, G. Sushko, S. Schramm, A.V. Solov'yov Kinetics of liquid-solid phase transition in large nickel clusters, *Physical Review B* 88 (3), 035438, 2013

17. I.N. Konsin, G.B.Sushko, S.A.Kharchenko "Three-level MPI+TBB+CUDA parallel implementation of block iteration algorithm of SLAE solver for small-block unstructured sparse matrices" (2012), in Russian
18. D.B. Volkov-Bogorodsky, G.B. Sushko, S.A. Kharchenko "Combined MPI+threads parallel implementation of the block method for heat transfer simulation in structurally inhomogeneous media", Numerical Methods and Programming, 127-136 (2010), in Russian
19. S.V. Zhluktoy, A.A. Aksenov, S.A. Kharchenko, I.V. Moskaev, G.B. Sushko, A.S. Shishaeva "Modeling of separated flows in CFD software FlowVision-HPC", Numerical Methods and Programming, 234-245 (2010), in Russian
20. A.A. Aksenov, A.A. Dyadkin, S.V. Zhluktoy, V.A. Kutin, I.V. Moskaev, G.B. Sushko, S.A. Kharchenko, A.S. Shishaeva "Solution of computational fluid dynamics problems on 'Lomonosov' supercomputer using FlowVision", Proceedings of conference "Scientific Services & Internet: Supercomputing Centers and Applications", (2010) in Russian
21. A.E. Shelaev, A.A. Aksenov, A.A. Dyadkin, V.A. Kutin, I.V. Moskaev, G.B. Sushko, S.A. Kharchenko "FlowVision HPC: Solution of big tasks of numerical hydrodynamics" (2009), in Russian
22. V.L. Yakushev, V.N. Simbirkin, A.V. Filimonov, P.A. Novikov, I.N. Konshin, G.B. Sushko, S.A. Kharchenko "Solution of ill-conditioned symmetric SLAE for structural mechanics problems by parallel iterative methods" Vestnik of Lobachevsky state university of Nizhni Novgorod, 4, (2012), 238-246, in Russian
23. G.B. Sushko, S.A. Kharchenko "Experimental study on SKIF MSU Chebyshev of the combined MPI+Threads implementation of the algorithm for solving systems of linear equations arising in FlowVision when simulating computational fluid dynamics problems" Vestnik of Lobachevsky state university of Nizhni Novgorod, 1, (2010), 202-209. in Russian
24. G.B. Sushko, S.A. Kharchenko "Multithreaded parallel implementation of iterative algorithm of solving systems of linear equations with dynamic load-

- balancing” Proceedings of the International Conference on Parallel Computing Technologies (PaVT’2008), in Russian
25. A.A. Aksenov, A.A. Dyadkin, V.A. Kutin, I.V. Moscalev, G.B. Sushko, S.A. Kharchenko ”Solution of big problems of computational fluid dynamics on SKIF MSU using FlowVision”, Proceedings of conference ”Scientific service in the internet: solving large problems”, 69-73, (2008), in Russian